OCEAN ENGINEERING GROUP

Numerical Simulation of Steady and Unsteady Cavitating Flows inside Water-jets

Shu-Hao Chang

August 2012

REPORT No.

12-01

ENVIRONMENTAL AND WATER RESOURCES ENGINEERING
DEPARTMENT OF CIVIL, ARCHITECTURAL AND ENVIRONMENTAL ENG.
THE UNIVERSITY OF TEXAS AT AUSTIN
AUSTIN, TX 78712

The Dissertation Committee for Shu-Hao Chang
certifies that this is the approved version of the following dissertation:

Numerical Simulation of Steady and Unsteady Cavitating Flows inside Water-jets

Committee:

Spyros A. Kinnas, Supervisor

Howard Liljestrand

Ben Hodges

Robert Moser

Venkat Raman

Numerical Simulation of Steady and Unsteady Cavitating Flows inside Water-jets

by

Shu-Hao Chang, B.S.; M.S.

Dissertation

Presented to the Faculty of the Graduate School of

The University of Texas at Austin

in Partial Fulfillment

of the Requirements

for the Degree of

Doctor of Philosophy

The University of Texas at Austin

August 2012

Dedicated to my family.

Acknowledgements

To begin with, I would like to show my gratitude to my supervisor, Professor Spyros A. Kinnas, for his fully-patient direction and continuous support throughout my graduate research life in the University of Texas at Austin. I have been benefited a lot from his valuable suggestions and stimulations. His thoughtfulness, wisdom and enthusiasm inspire me enormously to always put forth the best effort in my research and future career.

I would also like to express my great appreciation to the other members of my dissertation committee: Professor Howard M. Liljestrand and Professor Ben R. Hodges from Civil Engineering, Professor Robert D. Moser from Mechanical Engineering, and Professor Venkat Raman from Aerospace Engineering and Engineering Mechanics. They unconditionally reviewed the draft of my dissertation and offered me informative suggestions.

I want to take this chance to thank the staffs in the Offshore Technology Research Center (OTRC), Mrs. Sandra Vasquez and Mrs. Dori Eubank. A lot of appreciation goes to my dear friends in the Computational Hydrodynamics Laboratory (CHL), including Dr. Hanseong Lee, Dr. Yi-Hsiang Yu, Dr. Hong Sun, Dr. Vimal Vinayan, Dr. Lei He, Mr. Ye-Tian, Mr. Xiangming Yu, and Mr. Chan-Hoo Jeon for the help, encouragement and knowledge they shared with and brought to me during these six years. Especially Ye and Xiangming, thank you very much for accompanying me during many nights at the lab doing research.

Words are not enough for me to show my sincerest and deepest appreciation to my family. With their endless love and support, I was able to hold on and reach this far to the end.

Finally, support for this research was provided by the U.S. Office of Naval Research (Contract No. N00014-07-1-0616 and N0014-10-1-0931) and Phases V and VI of the "Consortium on Cavitation Performance of High Speed Propulsors" with the following current members: American Bureau of Shipping, Daewoo Shipbuilding and Marine Engineering Co. Ltd., Kawasaki Heavy Industry Ltd., Rolls-Royce Marine AB, Rolls-Royce Marine AS, Samsung Heavy Industries Co. Ltd., SSPA AB, Sweden, VA Tech Escher Wyss GmbH, Wärtsilä Propulsion Netherlands B.V., Wärtsilä Propulsion Norway AS, Wärtsilä Lips Defense S.A.S., and Wärtsilä CME Zhenjiang Propeller Co. Ltd. Special thanks to Mr. Thad Michael at NSWCCD (Naval Surface Warfare Center at Carderock Division) for sending his ONR AxWJ2 water-jet geometry and valuable feedback and suggestions on my research. Also special thanks to Mr. Seth D. Schroeder at NSWCCD for providing his numerical RANS case and data files, experimental data and report for the validations of my numerical scheme.

Numerical Simulation of Steady and Unsteady Cavitating Flows inside Water-jets

Publication No. _____

Shu-Hao Chang, Ph.D.

The University of Texas at Austin, 2012

Supervisor: Spyros A. Kinnas

A numerical panel method based on the potential flow theory has been refined and applied to the simulations of steady and unsteady cavitating flows inside water-jet pumps.

The potential flow inside the water-jet is solved simultaneously in order to take the interaction of all geometries (blades, hub and casing) into account. The integral equation and boundary conditions for the water-jet problem are formulated and solved by distributing constant dipoles and sources on blades, hub and shroud surfaces, and constant dipoles in the trailing wake sheets behind the rotor (or stator) blades. The interaction between the rotor and stator is carried out based on an iterative procedure by considering the circumferentially averaged velocities induced on each one by the other. The present numerical scheme is coupled with a 2-D axisymmetric version of the Reynolds Averaged Navier-Stokes (RANS) solver to evaluate the pressure rise on the shroud and simulate viscous flow fields inside the pump.

A tip gap model based on a 2-D orifice equation derived from Bernoulli's obstruction theory is implemented in the present method to analyze the clearance effect between the blade tip and the shroud inner wall in a global sense. The reduction of the flow from

losses in the orifice can be defined in terms of an empirically determined discharge coefficient (C_Q) representing the relationship between the flow rate and the pressure difference across the gap because of the viscous effect in the tip gap region.

The simulations of the rotor/stator interaction, the prediction of partial and super cavitation on the rotor blade and their effects on the hydrodynamic performance including the thrust/torque breakdown of a water-jet pump are presented. The predicted results, including the power coefficient (P^*), head coefficient (H^*), pump efficiency (η), thrust and torque coefficients (K_T and K_Q), as well as the cavity patterns are compared and validated against the experimental data from a series of measurements on the ONR AxWJ-2 pump at NSWCCD.

Table of Contents

List of Tables

List of Figures

Chapter 1: Introduction

1.1 BACKGROUND

The increasing demand for high-speed marine vessels has primarily driven the design of propulsion systems recently. Complex propulsor configurations are becoming rather common to achieve the performance of high efficiency, safety, comfort and cost effective maintenance. Water-jet propulsion systems have become fairly popular on commercial and naval applications nowadays. The absence of appendages such as shafts, rudders and ducts under the waterline not only lowers the resistance but also makes water-jets a preferred solution of shallow water maneuvering. Figure 1.1 shows a water-jet pump system used for the propulsion of high speed water vessels. Furthermore, the possibility of cavitation occurrence and the debris damages to the propeller can also be reduced inside water-jet pumps. Nevertheless, cavitation is always an inevitable issue. The thrust breakdown caused by super cavitation is an important subject related to the performance of a water-jet operating in extreme conditions. In addition, water-jet pumps typically have a small clearance between the rotor blade tip and the shroud inner surface. This allows the loading to be carried up to the tip of the blade but also causes the cavitation occurrence in this gap region. The flow around the tip zone and the effects of the gap must also be adequately modeled to obtain more accurate evaluation of the rotor performance. Figure 1.2 shows a yacht using a water-jet pump as its propulsion system.

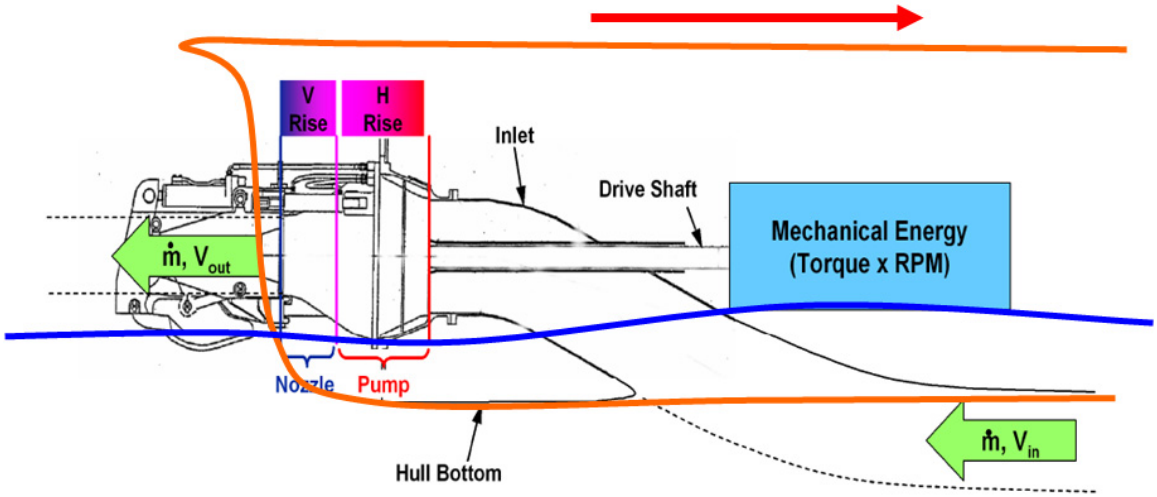

Figure 1.1: A water-jet pump propulsion system used for high speed vessels (source: http://www.ce.utexas.edu/prof/kinnas/319LAB/PICTS/waterjethull.png).

Figure 1.2: A yacht using water-jet as its propulsion system (source: http://megayachts.ru/res/news/20051028/37/609.jpg).

1.2 MOTIVATION

The motivation of this research is to apply a low order potential based panel method to have adequate evaluation of pressure rise on the shroud across rotor and stator blades and a better prediction of cavitating performance as well as thrust breakdown phenomenon inside a water-jet pump. The main benefit from this study is a better understanding of the hydrodynamic characteristics of the blade cavitation. Furthermore, the outcome of this work will lead to a better prediction of hydrodynamic performance inside a water-jet pump for use at the early design stage.

1.3 OBJECTIVES

The objective of this research is to develop a numerical approach based on potential flow method to simulate the rotor and stator interaction inside water-jet pumps, as well as to predict partial and super cavitation on the rotor blade and their effects on the hydrodynamic performance of water-jet propulsion systems. The following assumptions or approaches are applied in order to achieve the main objectives.

- The fluid domain is numerically modeled via a low order panel method based on the perturbation velocity potential.
- The integral equation and boundary conditions for water-jets are formulated and solved by distributing constant dipoles and sources on blades, hub and shroud surfaces, and constant dipoles on the trailing wake sheets behind the rotor (or stator) blades.
- The interaction between the rotor and the stator of the water-jet is accounted for through an iterative process that considers the *circumferentially averaged induced velocities* on the control points from one to the other.

- The current method is coupled with a Renolds Averaged Navier Stokes (RANS) based Computational Fluid Dynamics (CFD) tool to evaluate pressure rise on the shroud surface in the water-jet.
- The range of applicability of the present method is tested by comparisons with experiments and other numerical methods.

1.4 OVERVIEW

This dissertation is organized into six main chapters.

Chapter 1 contains background, motivation and objectives of this research.

Chapter 2 presents literature reviews of the related studies on the numerical simulation and experiments on water-jet propulsion systems and the tip gap model.

Chapter 3 describes the methodology used in this research including assumptions, governing equations, boundary conditions, rotor/stator interaction, inviscid/viscous coupling scheme, the tip gap model and steady wake alignment on the rotor problem.

Chapter 4 shows the numerical validation and convergence studies of the present method on the steady rotor and stator problem and induced swirl velocities on the stator blade by the rotor.

Chapter 5 presents the predicted numerical results of the water-jet in steady and unsteady wetted and cavitating simulations and the correlations with the experimental data and the results from RANS solvers.

Chapter 6 summarizes the conclusions and the contributions of this dissertation, and provides recommendations for future research.

Chapter 2: Literature Review

This chapter reviews the existing literature related to the studies of water-jet propulsion systems. The first part discusses numerical methods related to the simulations of the water-jet problem. The second part focuses on the experimental studies of water-jets. Finally, a review of the research on the tip gap model is given.

2.1 THE WATER-JET PROBLEM

Axial flow water-jets are marine propulsors promising to provide a balance between the robustness and performance and are particularly suited for high-speed vessels. However, complex geometry configurations, inherent unsteadiness of the interaction between the rotor and stator, and inevitable cavitation due to local pressure depression makes the simulations and analyses of flow fields inside water-jets considerably challenging. Several numerical and experimental approaches have been developed and applied to analyze the water-jet problem over past years. The first subsection will review the existing numerical methods and the second subsection will review the existing experimental studies.

2.1.1 Numerical Studies on Water-jets

Using numerical methods to solve water-jet propulsion systems has become much more challenging because of the complex geometric configurations and the interactions among the components inside of a water-jet pump. Kerwin (2006) presented a comprehensive review regarding the issues in predicting the performance and in designing of water-jets.

Presently, numerical methods for predicting the cavitating performance and assisting the design of water-jet propulsors are still limited. A more detailed description of and literature review on water-jets can be found in the International Towing Tank Conference (ITTC, 2008). CFD tools, especially RANS solvers, have gained increasing popularity for simulating flows inside water-jets. Chun et al. (2002) used a RANS solver with a moving, non-orthogonal body-fitted multi-blocked grid system for the interaction of the rotor and stator. The former component was considered in an unsteady sense and the latter component was accounted for in a circumferentially averaged sense. Brewton et al. (2006) incorporated periodic boundaries and a mixing plane model into a RANS method, and considered the interaction between the rotor and the stator in the time-averaged sense. Schroeder et al. (2009) used a Multiphase Computational Fluid Dynamics (MCFD) solver based on the Open Field Operation and Manipulation (OpenFOAM) CFD library to predict the power performance of the ONR AxWJ1 water-jet. Lindau et al. (2009; 2011) also applied a RANS solver with homogeneous-multiphase modeling and turbulent simulation capabilities, and by using 3-D powering iteration methodology, they simulated water-jet flows over a wide range of flow coefficients and were able to model the cavitation driven breakdown. An intermediate approach which combines potential flow method and RANS was applied to the prediction and design of water-jet components. Taylor et al. (1998) and Kerwin et al. (1997) applied a vortex lattice method (VLM) coupled with either a RANS solver or an Euler equation solver to include the effects of the hull and other appendages, and to analyze the global flow through the water-jet pump.

Kinnas et al. (2007a; 2010) applied a panel method to predict performances of a water-jet, and the interaction between the rotor and the stator was considered in an iterative manner via taking into account the circumferentially averaged *induced potentials*

from one to the other. Sun (2008), Sun and Kinnas et al. (2006; 2008) and Kinnas et al. (2007b) have used the viscous/inviscid interactive approach successfully by coupling with a boundary layer solver (XFOIL, Drela 1989) to simulate the viscous flow around single, ducted and ONR AxWJ1 water-jet propulsion systems, including boundary layer effects on the cavities over the blades.

The potential-based boundary element method (BEM) by Fine and Kinnas (1993) and Kinnas & Fine (1993) was improved and refined considerably to simulate cavitating propulsor flows (Young 2002; Lee 2002). The method is able to predict mixed cavity patterns including the partial cavity and super cavity on the face and back sides of surface-piercing propellers (Young 2002; Young and Kinnas 2001; 2003; 2004) and ducted propellers (Lee and Kinnas 2006). The method is also able to simulate tunnel effects on marine propellers (Lee and Kinnas 2005), as well as to predict tip vortex cavitation and unsteady wake alignment (Lee and Kinnas 2004). A similar solver based on the boundary element method was also developed by Gaggero and Brizzolara (2008; 2009) to predict the cavitation of open propellers or a propeller inside an axial cylinder.

2.1.2 Experimental Studies

The design of a water-jet propulsion system requires CFD tools for simulating and predicting the flow inside the pump. Validation of CFD numerical results demands detailed experimental data on flow patterns and turbulence over the entire pump system.

The ONR AxWJ1 pump has undergone a series of tests in a closed-loop cavitation tunnel at John Hopkins University by Wu and Katz et al. (2008; 2011). The rotor, stator and casing are made of acrylic and especially designed to use index matching fluid. Such matching makes the blades invisible and enables flow structure visualization without any

obstructions. A stereo Particle Image Velocimetry (PIV) system was used to measure the cavitation in the vicinity of the tip region and the roll-up of tip leakage vortex (TLV). Steady state powering performance and pressure rise of the ONR AxWJ1 pump were measured by Wu et al. (2009).

A series of performance evaluations of the ONR AxWJ2 water-jet pump in a 36-inch Variable Pressure Water Tunnel (36VPWT) has been measured by Chesnakas et al. (2009) at NSWCCD. The measurements included pressure rise on the casing, impeller thrust and torque in fully-wetted and cavitating conditions, and the observations included the impeller cavitation coverage and TLV.

2.2 THE TIP GAP MODEL

In the potential flow simulation of a water-jet, the treatment of a gap flow remains a critical issue that may drastically affect the loading distributions around the blade tip. In order to incorporate a clearance flow model inside the gap, an appropriate expression for a leakage volume flow through the gap can be implemented.

Different models for the potential flow in the gap region include: nonzero and zero gap width and a tip leakage model with a vortex sheet shedding along the chord at the tip of the propeller blade developed by Gu (2006). Other models controlling the volume flow rate through the gap and based on orifice theory have been proposed by Kerwin et al. (1987) and applied in panel methods by Hughes (1993; 1997), Moon et al. (2002), and Gaggero et al. (2009). A 2-D orifice equation model in which the velocity can be related to the pressure difference across the tip region of the blade by applying Bernoulli's obstruction theory is implemented in the present numerical method. Following the work by Hughes (1997), the reduction in the flow from losses in the orifice

can be defined in terms of an empirically determined discharge coefficient (C_Q) representing the relationship between the flow rate and the pressure difference across the clearance region.

Chapter 3: Methodology

A low order panel method solver based on the potential flow theory is improved, refined and applied to analyze unsteady propulsion systems, and is coupled with a Reynolds Averaged Navier-Stokes (RANS) solver, ANSYS FLUENT, to simulate the viscous flow inside a water-jet pump. The details of governing equations, numerical method and boundary conditions for solving inviscid wetted and cavitating flows inside a water-jet are addressed in this chapter.

3.1 ASSUMPTIONS

In Figure 3.1, a typical configuration of water-jet geometry along with its coordinate systems is shown. (X_s, Y_s, Z_s) denotes a ship fixed coordinate system and (X, Y, Z) is a propeller fixed coordinate system. The following assumptions are made for solving the water-jet problem:

1. The effective inflow $\vec{q}_w$ given at the inlet of the pump is defined in a ship fixed coordinate system and is assumed to be uniform for steady problems. However, the effective inflow (as shown in Figure 5.41) can be non-uniform for unsteady problems.
2. The rotor blades rotate with a constant angular velocity vector ω.
3. The stator blades do not rotate and are fixed in the propeller fixed coordinate system.
4. The total inflow velocity $\vec{V}_{in}$ in the propeller fixed coordinate system can be expressed as:

$$\vec{V}_{in}(x,y,z,t) = \vec{q}_w(x,r,\theta-\omega t) + \omega \times X \qquad \text{for rotor,}$$

$$\vec{V}_{in}(x,y,z,t) = \vec{q}_w(x,r,\theta) \qquad \text{for stator,}$$

where $r = \sqrt{y^2+z^2}$, $\theta = \tan^{-1}(z/y)$ and $X = (X,Y,Z)$.

5. The flow is assumed to be inviscid, incompressible and irrotational. Therefore, the velocity field in the rotating coordinate system can be described as:

$$\vec{q}_t(x,y,z,t) = \vec{V}_{in}(x,y,z,t) + \nabla\phi(x,y,z,t) \tag{3.1}$$

where $\vec{q}_t(x,y,z,t)$ is the total velocity at any point (x,y,z) inside the fluid domain. $\nabla\phi(x,y,z,t)$ is the perturbation velocity and $\phi(x,y,z,t)$ is the perturbation potential which satisfies the Laplace's equation $\nabla^2\phi = 0$.

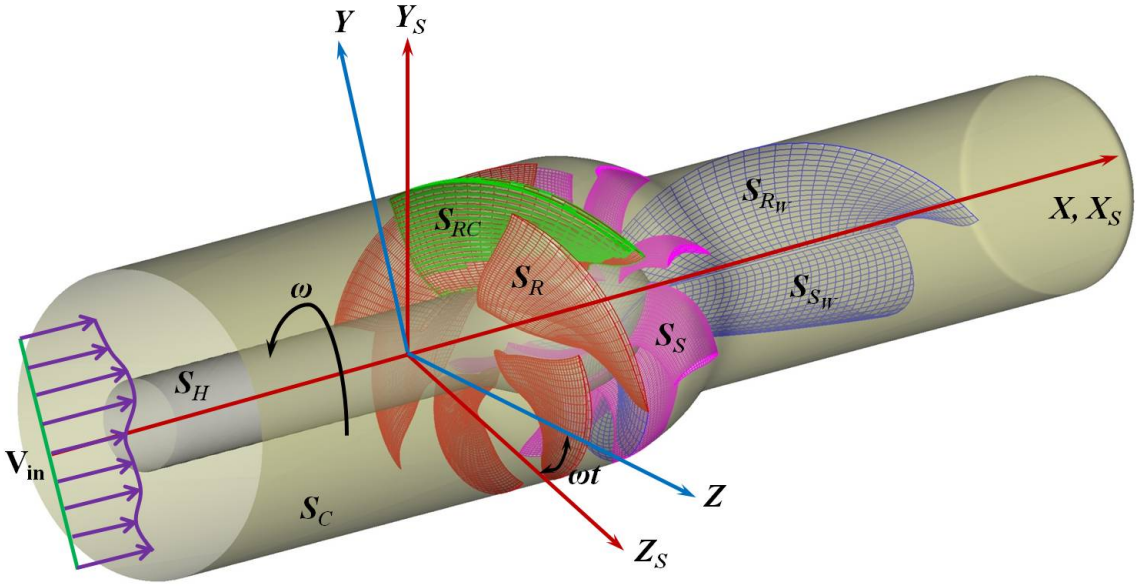

Figure 3.1: A water-jet problem subject to a general inflow and coordinate system.

3.2 GOVERNING EQUATIONS

The perturbation potential $\phi(x,y,z)$ at any point $p(x,y,z)$ located either on the fully-wetted rotor and stator, hub and casing surfaces, $S_R \cup S_S \cup S_H \cup S_C$, or on the cavitating rotor and stator surfaces, $S_{RC} \cup S_{SC}$, has to satisfy the Green's third identity in Equation (3.2). It should be noted that ϕ is a function of time since the interaction between the rotor and stator is essentially unsteady. Analysis of the interaction between

the two components numerically in a fully unsteady sense is rather difficult and prohibitively expensive for the computation. Therefore, an alternative method to simulate the flow inside a water-jet pump is via an iterative procedure which solves the rotor problem and the stator problem separately and the interaction between the two is taken into account by considering the circumferentially averaged effects of each component to the other.

$$
\begin{aligned}
2\pi\phi = & \int_{S_R + S_{R_C}} \left[\phi_q \frac{\partial G(p;q)}{\partial n_q} - G(p;q) \frac{\partial \phi}{\partial n_q} \right] ds + \\
& \int_{S_{R_W}} \Delta\phi_{R_W} \frac{\partial G(p;q)}{\partial n_q} ds + \\
& \int_{S_S + S_{S_C}} \left[\phi_q \frac{\partial G(p;q)}{\partial n_q} - G(p;q) \frac{\partial \phi}{\partial n_q} \right] ds + \\
& \int_{S_{S_W}} \Delta\phi_{S_W} \frac{\partial G(p;q)}{\partial n_q} ds + \\
& \int_{S_{HC}} \left[\phi_q \frac{\partial G(p;q)}{\partial n_q} - G(p;q) \frac{\partial \phi}{\partial n_q} \right] ds
\end{aligned}
\tag{3.2}
$$

where the p and q correspond to the variable points and the field points, respectively. $G(p;q) = 1/R(p;q)$ is the Green function and $R(p;q)$ is the distance between the field point p and the variable point q. n indicates the normal direction pointing into the flow field. $\Delta\phi_{RW}$ and $\Delta\phi_{SW}$ are the potential jumps across the trailing wake sheets shedding from either the rotor or the stator blade trailing edge respectively.

Figure 3.2 is the schematic sketch of the rotor and stator problem, the rotor only problem, and the stator only problem respectively. The interaction is carried out via induced velocities in the present method. In addition, the rotor is solved with respect to the rotating coordinate system and the stator is solved with respect to the ship fixed coordinates system.

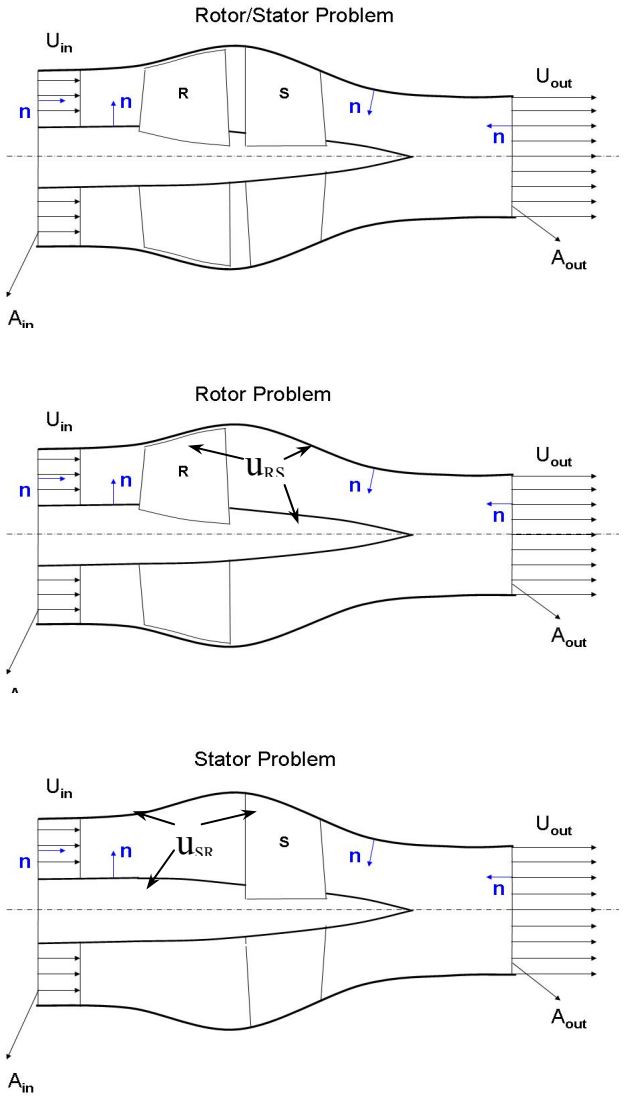

Figure 3.2: Schematic sketch: (a) the rotor and stator problem, (b) the rotor only problem, and (c) the stator only problem. Problems (b) and (c) are solved in sequence with circumferentially-averaged effects (induced velocities) of the one to the other in an iterative manner for solving problem (a) (modified from Kinnas et al. 2007a).

3.3 THE INDUCED VELOCITY METHOD

In the induced velocity method, the interaction between the rotor and stator is taken into account by applying the circumferentially averaged induced velocities from one to the other. This section summarizes the integral equations for the rotor and stator problems, and the evaluation of the circumferentially averaged induced velocities.

3.3.1 The Rotor Problem

Equation (3.3) is the integral equation for the rotor problem by using the induced velocity method.

$$\begin{aligned} 2\pi\phi = & \int_{S_R+S_{RC}} \left[\phi_q \frac{\partial G(p;q)}{\partial n_q} - G(p;q) \frac{\partial \phi_q}{\partial n_q} \right] ds + \\ & \int_{S_{R_W}} \Delta\phi_{R_W} \frac{\partial G(p;q)}{\partial n_q} ds + \\ & \int_{S_{HC}} \left[\phi_q \frac{\partial G(p;q)}{\partial n_q} - G(p;q) \frac{\partial \phi_q}{\partial n_q} \right] ds \end{aligned} \tag{3.3}$$

where the source strength $\partial\phi/\partial n$ is modified as,

$$\frac{\partial \phi}{\partial n} = -(\vec{q}_{in}(x,y,z,t) + \vec{u}_{RS}) \cdot \vec{n} \tag{3.4}$$

and $\vec{u}_{RS}$ is the circumferentially averaged induced velocities on the rotor, hub and casing surfaces by the stator and are evaluated by the following integral equation:

$$\begin{aligned} 4\pi\vec{u}_{RS} = & \int_{S_S+S_{SC}} \left[\phi_q \nabla \frac{\partial G(p;q)}{\partial n_q} - \nabla G(p;q) \frac{\partial \phi_q}{\partial n_q} \right] ds + \\ & \int_{S_{S_W}} \Delta\phi_{S_W} \nabla \frac{\partial G(p;q)}{\partial n_q} ds \end{aligned} \tag{3.5}$$

$\nabla(\partial G/\partial n)$ and ∇G are evaluated via a numerical subroutine *RPAN*, which calculates the induced potentials and induced velocities due to unit strength sources and

normal dipoles over a quadrilateral panel. Details of evaluating induced potentials and velocities can be found in Newman (1986).

3.3.2 The Stator Problem

Equation (3.6) is the integral equation for the stator problem by using the induced velocity method.

$$
\begin{aligned}
2\pi\phi = & \int_{S_S + S_{SC}} \left[\phi_q \frac{\partial G(p;q)}{\partial n_q} - G(p;q) \frac{\partial \phi_q}{\partial n_q} \right] ds + \\
& \int_{S_{S_W}} \Delta\phi_{S_W} \frac{\partial G(p;q)}{\partial n_q} ds + \\
& \int_{S_{HC}} \left[\phi_q \frac{\partial G(p;q)}{\partial n_q} - G(p;q) \frac{\partial \phi_q}{\partial n_q} \right] ds
\end{aligned}
\tag{3.6}
$$

where the source strength $\partial\phi/\partial n$ is modified as,

$$
\frac{\partial \phi}{\partial n} = -(\vec{q}_{in}(x, y, z, t) + \vec{u}_{SR}) \cdot \vec{n} \tag{3.7}
$$

and $\vec{u}_{SR}$ is the circumferentially averaged induced velocities on the stator, hub and casing by the rotor and are calculated by the following integral equation:

$$
\begin{aligned}
4\pi\vec{u}_{SR} = & \int_{S_R + S_{RC}} \left[\phi_q \nabla \frac{\partial G(p;q)}{\partial n_q} - \nabla G(p;q) \frac{\partial \phi_q}{\partial n_q} \right] ds + \\
& \int_{S_{R_W}} \Delta\phi_{R_W} \nabla \frac{\partial G(p;q)}{\partial n_q} ds
\end{aligned}
\tag{3.8}
$$

3.4 BOUNDARY CONDITIONS

In order to solve the rotor or stator problem, the following boundary conditions must be satisfied: (1) the kinematic boundary condition on the wetted rotor or stator blades, hub and casing surfaces; (2) the dynamic boundary conditions on the rotor or stator blade cavity surfaces; (3) the kinematic boundary conditions on the rotor or stator blade cavity surfaces; (4) the Kutta condition; (5) the cavity detachment and (6) the cavity closure conditions. It should be noted that the dynamic and kinematic boundary conditions for determining the cavity shape are applied on the approximated boundary, which is the blade surface beneath the cavity. The cavity shape is unknown and has to be calculated as part of the solutions when applying a fully non-linear analysis for 3-D cavitating flow simulations. The reason for applying approximated boundary is to avoid the computationally expensive re-paneling on the cavity surface and the re-calculation of influence coefficients. More detailed descriptions can be found in Fine (1992).

The boundary conditions applied on the rotor/stator, hub, casing, cavity and the wake surfaces are as following:

1. The kinematic boundary condition on the fully-wetted rotor/stator, hub and casing surfaces requires the flow is tangent to the body surfaces.

$$\frac{\partial \phi}{\partial n} = -\vec{V}_{in}\left(x, y, z, t\right) \cdot \vec{n} \tag{3.9}$$

2. The dynamic boundary condition on the cavitating blade and wake surfaces requires that the pressure inside and on the cavity is constant and equal to the vapor pressure, P_v. There are slight differences between the rotor and stator problems when implementing the dynamic boundary condition on the cavity surface. By applying Bernoulli's equation with respect to the propeller fixed coordinate system, the total velocity on the cavity surface can be expressed as:

$$\left|\vec{q}_t\right|^2 = n^2 D^2 \sigma_{n,rotor} + \left|\vec{V}_{in}\right|^2 + \omega^2 r^2 - 2gy_s - 2\frac{\partial \phi}{\partial t} \quad \text{for rotor}$$
$$\left|\vec{q}_t\right|^2 = (1+\sigma_{n,stator})\left|\vec{V}_{in}\right|^2 - 2gy_s - 2\frac{\partial \phi}{\partial t} \quad \text{for stator} \tag{3.10}$$

where n and D are the blade rotational frequency (*rps*) and the propeller diameter, respectively. ω is the angular velocity and r is the distance from the axis of rotation. g is the acceleration of gravity and y_s is the vertical distance from the horizontal plane through the axis of rotation. The cavitation number σ_n for rotor and stator is defines as follows:

$$\sigma_n = \frac{P_o - P_v}{0.5\rho n^2 D^2} \text{ for rotor}$$
$$\sigma_n = \frac{P_o - P_v}{0.5\rho V_{in}^2} \quad \text{for stator} \tag{3.11}$$

where ρ denotes water density and P_0 is the far upstream pressure on the shaft axis. The total velocity on the cavity $\overrightarrow{q_t}$ may also be expressed in terms of the directional derivatives of the perturbation potential and the components of the inflow along the non-orthogonal coordinate system:

$$\overrightarrow{q_t} = \left(\frac{\partial \phi}{\partial n} + U_n\right)\vec{n} + \frac{\left(\frac{\partial \phi}{\partial s} + U_s\right)\left[\vec{s} - \left(\vec{s}\cdot\vec{v}\right)\vec{v}\right] + \left(\frac{\partial \phi}{\partial v} + U_v\right)\left[\vec{v} - \left(\vec{s}\cdot\vec{v}\right)\vec{s}\right]}{\left\|\vec{s}\times\vec{v}\right\|^2} \tag{3.12}$$

where $\vec{s}$ and $\vec{v}$ are the unit vectors corresponding to the coordinates $\vec{s}$ (chordwise) and $\vec{v}$ (span-wise) as shown in Figure 3.3. $\vec{n}$ is the unit normal vector to the cavity. U_s, U_v and U_n are the inflow velocities along (s, v, n) directions. Combining the equations for $\overrightarrow{q_t}$, $\frac{\partial \phi}{\partial s}$ can be expressed as follows:

$$\frac{\partial \phi}{\partial s} = -U_s + \left(\frac{\partial \phi}{\partial v} + U_v\right)\cos\theta + \sin\theta\sqrt{\left|\overrightarrow{q_t}\right|^2 - \left(\frac{\partial \phi}{\partial v} + U_v\right)^2} \tag{3.13}$$

where θ is the angle between $\vec{s}$ and $\vec{v}$, and $\cos\theta = \vec{s} \cdot \vec{v}$. Finally, the equation for the perturbation potential on the cavity over blade surface can be derived by integrating the equation as follows:

$$\phi(s,v,t) = \phi(0,v,t) + \int_0^s \left[-U_s + \left(\frac{\partial \phi}{\partial v} + U_v \right) \cos\theta + \sin\theta \sqrt{|\vec{q}_t|^2 - \left(\frac{\partial \phi}{\partial v} + U_v \right)^2} \right] ds \qquad (3.14)$$

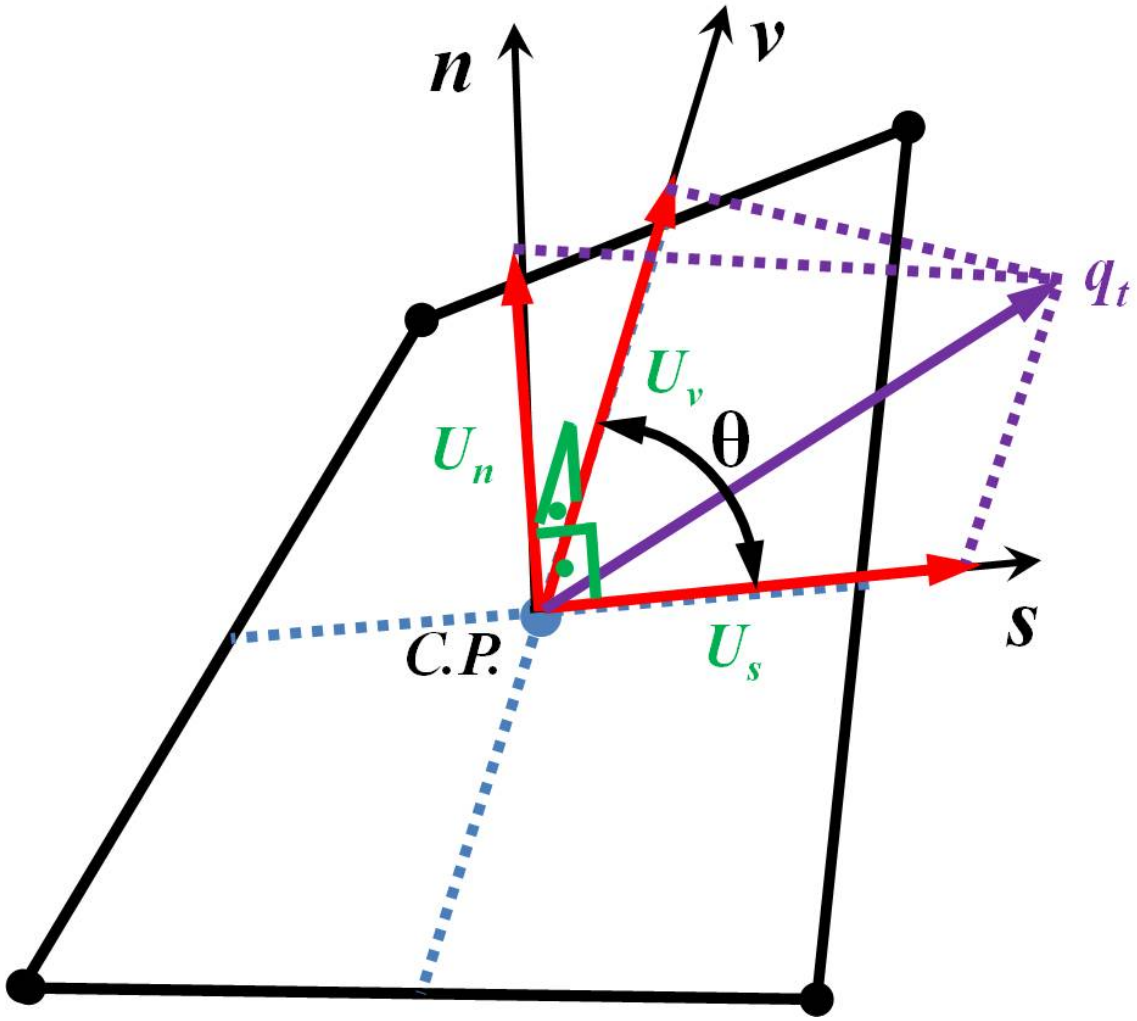

Figure 3.3: Local non-orthogonal coordinate system on the blade, hub and casing panels. Vectors *s* and *v* are formed by the lines connecting the midpoints of panel edges. Vector *n* is normal to *s* and *v*.

And, on the super cavity over the wake surface is:

$$\phi^{+}(s,u,t)=\phi(s_{TE},u,t)+\int_{S_{TE}}^{s}\left[-U_{s}+\sqrt{\left|\vec{q_t}\right|^{2}-\left(V_{u}^{+}\right)^{2}}\right]ds \tag{3.15}$$

The potential $\phi\,(0,\mathrm{v},\mathrm{t})$ corresponds to the potential value at the cavity leading edge, and can be extrapolated in terms of the unknown potentials of wetted parts in front of the cavity detachment location. $\mathrm{s}=\mathrm{s_{TE}}$ denotes the blade trailing edge. The variable u in the equation for $\phi^{+}(\mathrm{s},\mathrm{u},\mathrm{t})$ corresponds to the directional derivative normal to (s,n) plane on wake surface, and the superscript, $+$, represents the upper side of the wake sheet. The equations for the potential on cavity includes the unknown functions, $\frac{\partial\phi}{\partial t}$ and $\frac{\partial\phi}{\partial v}$, and those terms are determined in an iterative manner.

3. The kinematic boundary condition, which is used to determine the actual cavity shape, requires the substantial derivative of the cavity surface vanishes.

$$\left(\frac{\partial}{\partial t}+\vec{q_t}\cdot\nabla\right)\left[n-h(s,v,t)\right]=0 \tag{3.16}$$

where h is the cavity thickness normal to the blade surface.

Once the boundary value problem is solved, the kinematic condition is used to determine the position of the cavity surface. The partial differential equation for the cavity thickness is as follows:

$$\frac{\partial h}{\partial s}(V_{s}-V_{v}\cos\theta)+\frac{\partial h}{\partial v}(V_{v}-V_{s}\cos\theta)=\left(V_{n}-\frac{\partial h}{\partial t}\right)\sin^{2}\theta \tag{3.17}$$

where

$$V_{s}=\frac{\partial\phi}{\partial s}+U_{s}\ ,\ V_{v}=\frac{\partial\phi}{\partial v}+U_{v}\ ,\ V_{n}=\frac{\partial\phi}{\partial n}+U_{n} \tag{3.18}$$

The cavity height normal to the blade surface can be determined by solving the above partial differential equation. Similarly, the cavity height h_w on wake surface when the super cavity occurs can be determined:

$$\frac{\partial h_w}{\partial s}\left|\vec{q_t}\right| = q_w(t) - \frac{\partial h_w}{\partial t} \tag{3.19}$$

where the strength of the cavity source on wake surface, $q_w(t)$ is:

$$q_w(t) = \frac{\partial \phi^+}{\partial n} - \frac{\partial \phi^-}{\partial n} \tag{3.20}$$

4. The Kutta condition, which implies that the fluid velocities at the blade trailing edge are finite.

$$|\nabla \phi| < \infty \text{ at blade and duct trailing edge} \tag{3.21}$$

At the blade trailing edge, an iterative pressure Kutta (*IPK*) condition is applied to ensure that the pressures on the pressure side and suction side are equal in Kinnas and Hsin (1992).

5. The cavity detachment locations are determined iteratively by satisfying the Villat-Brillouin smooth detachment conditions, as described in Young (2002).
6. The cavity closure condition implies that the cavity has to be close at the cavity trailing edge. Since the extent of the unsteady cavity is unknown and has to be determined as a part of the solutions, a split-panel technique and a Newton-Raphson iterative method are applied to find the correct cavity extent which satisfies the cavity closure condition at the given cavitation number presented in Fine (1992); Kinnas and Fine (1993).

Boundary Condition at Water-jet Inlet and Outlet

The simulation of a water-jet pump is an internal boundary value problem. Unlike the external flow problem in an unbounded fluid domain, boundary conditions at the water-jet inlet and outlet are required to make the solution unique.

1. At the pump inlet, the flow is assumed to be equal to the inflow.

$$\left.\frac{\partial \phi}{\partial n}\right|_{in} = \nabla \phi \cdot \vec{n} = 0 \tag{3.22}$$

   It should also be noted that the water-jet inlet panels are removed and the perturbation potentials are assumed to be zero at the inlet to obtain a unique solution of an internal boundary value problem.

2. The flow at the pump outlet has to satisfy the conservation of mass.

$$\left.\frac{\partial \phi}{\partial n}\right|_{out} = V_{in} - V_{out} \tag{3.23}$$

   As a result, the velocity at the outlet is:

$$V_{in} \cdot A_{in} = V_{out} \cdot A_{out} \Rightarrow V_{out} = V_{in} \frac{A_{in}}{A_{out}} \tag{3.24}$$

   where V_{in} is the inflow velocity. A_{in} and A_{out} are the areas of the pump inlet and outlet, respectively.

It should be noted that when solving the boundary value problem of the internal flow, the perturbation potentials at the inlet are set to zero automatically to make the solutions of the whole system unique.

3.5 THE EMPIRICAL VISCOUS PITCH CORRECTION

The governing equation for the water-jet problem is based on the potential flow theory and thus the boundary layer effects are not taken into consideration. The influence of the boundary layer on the rotor performance can either be included by coupling with a boundary layer solver (XFOIL) in Sun (2008) or can be approximated by applying an empirical viscous pitch correction and a frictional coefficient to the potential flow solutions. Kerwin and Lee (1987) proposed a viscous pitch correction on the basis of Brockett's (1966) work on 2-D sections, where the influence of the boundary layer on the lift of the blade sections was approximated by reducing the pitch angle of the each section by the amount of:

$$\Delta\alpha = 1.9454 \frac{t_{\max}}{C} \left| \frac{f_{\max}}{C} \right| \tag{3.25}$$

where $\Delta\alpha$ is in radians. C is the chord length of each blade section. t_{max}/C is the maximum thickness-chord ratio, and f_{max}/C is the maximum camber-chord ratio.

The frictional force on the rotor blade is considered as:

$$K_{T,fr} = C_f J_S^2 A_R / 8 \tag{3.26}$$

where C_f is a frictional coefficient taken as a function of the Renolds number (Re) of the rotor. J_S is the advance ratio and A_R is the non-dimensionalized surface area of the rotor. The value of C_f is determined by using the formula as:

$$C_f = \frac{0.075}{\left(\log \mathrm{Re} - 2\right)^2} \tag{3.27}$$

Therefore, the total thrust of the rotor including the viscosity effect is as following:

$$K_{T,vis} = K_{T,inv} - K_{T,fr} \tag{3.28}$$

3.6 THE INTERACTION BETWEEN THE ROTOR AND STATOR

The iterative procedures between the rotor and stator and the algorithm of evaluating circumferentially averaged effects (induced velocities) from each component to the other are summarized here. The induced velocities on the other component are first calculated from Equation (3.5) for $\boldsymbol{4\pi\vec{u}_{RS}}$ and Equation (3.8) for $\boldsymbol{4\pi\vec{u}_{SR}}$ and then are taken circumferentially average to apply on the control points of blade panels. The problems for both components by solving Equation (3.3) and Equation (3.6) are iterated until the forces are converged within a certain criterion. As an instance, the calculation of the circumferentially averaged induced velocities in the case of a stator problem is explained. Figure 3.4 shows how the induced velocities at the control points of the stator blade due to the rotor influence are calculated and averaged. The induced velocities on the stator by each panel on the rotor key blade can be derived as follows (N is the number of equally spaced points over an angle equal to that between two rotor blades):

$$u_{SR}^{j} = \frac{\sum_{i=1}^{i=N} u_{SR,i}^{\ j}}{N} \tag{3.29}$$

The circumferentially averaged induced velocities due to the rotor wake are evaluated at those equally spaced points (without including points on the wakes) between two wakes in a similar approach as shown in Figure 3.4, and then interpolated to the control points on the stator.

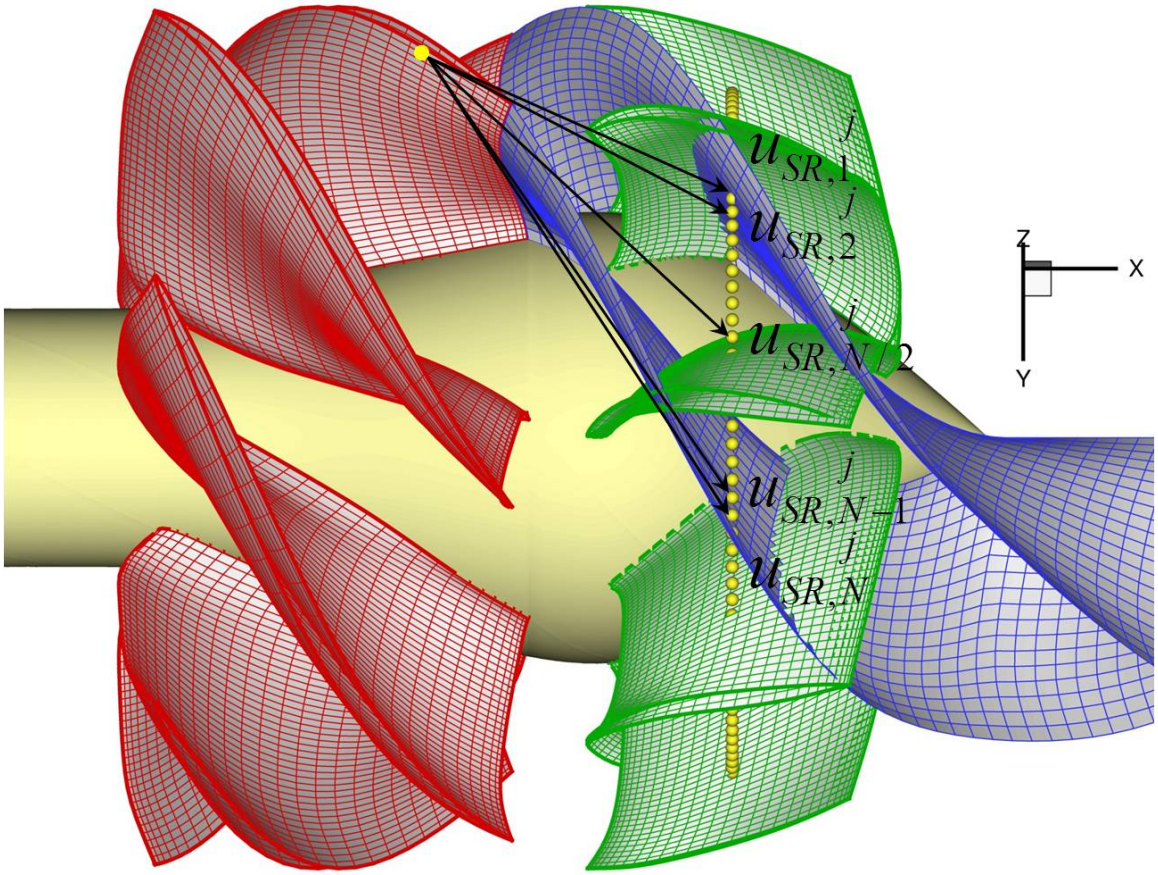

Figure 3.4: Schematic sketch of the inclusion of the circumferentially averaged rotor effects (induced velocities) to control points on the stator.

3.7 THE POTENTIAL/VISCOUS FLOW SOLVER COUPLING

A hybrid algorithm of coupling the present method with a viscous solver is utilized to analyze the flow field and evaluate the pressure rises on the casing inside a water-jet pump.

The overview of the hybrid scheme is shown in Figure 3.5. The potential flow solver is used for simulating the propeller blades, and the viscous flow solver is applied to solve the flow field around the hub, casing and propeller in order to include effects of vorticity and boundary layers. The resulting pressure distributions on the blade are converted into body forces, which are considered as source terms in the momentum equations to represent the propeller blades in the RANS solver.

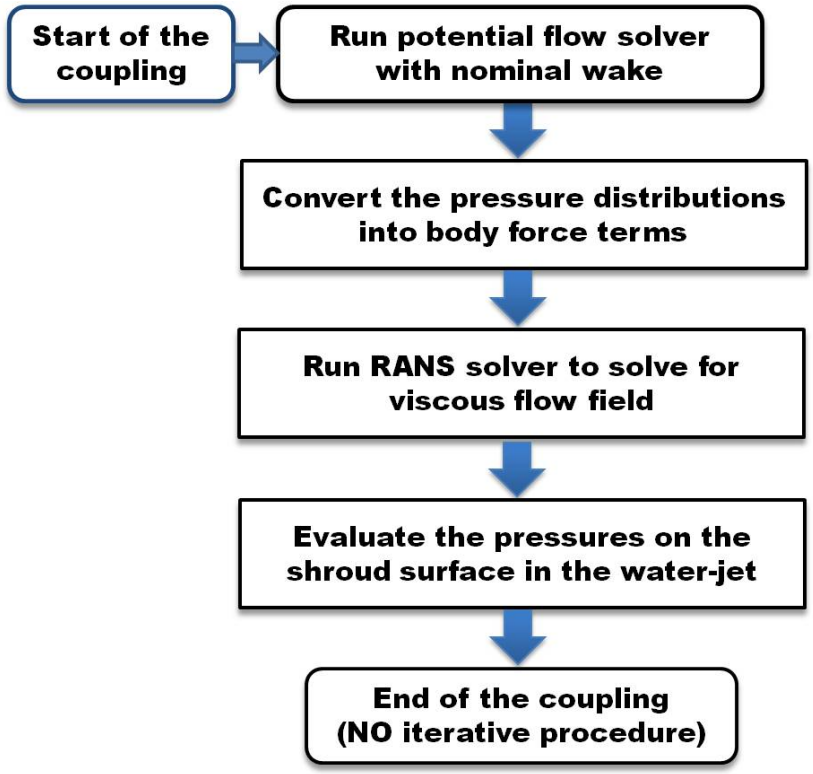

Figure 3.5: Overview of the coupling procedure for the hybrid scheme.

The RANS model in this research uses a commercial software package, ANSYS FLUENT (version 12.0.16), and the grids are generated by applying ANSYS GAMBIT. The solutions are computed by using the steady-state pressure based solver. The SIMPLEC pressure-correction algorithm and the second-order upwind scheme are applied in FLUENT. The *k-ω* turbulent model is utilized with standard wall function, and h-refinement (hanging nodes) is implemented near casing and hub surfaces so that the range of y^+ satisfies the requirement of the turbulent model.

The body force terms in the RANS method are calculated by integrating the pressure difference Δp, between the pressure side and suction side of the blade, on the blade surface. The pressure force vector F_P for each panel on the mean camber surface is given as:

$$\mathbf{F_p} = \Delta p A_c \, \mathbf{n} \tag{3.30}$$

where A_c is the area of the panel, $\boldsymbol{n}$ indicates the normal vector to the mean camber surface. In the 2-D axisymmetric domain, the propeller blade is projected to the *X-R* plane as shown in Figure 3.6. The body forces are, therefore, averaged in the circumferential direction. The body force per unit volume vector F_b becomes:

$$\mathbf{F}_b = \frac{\mathbf{F_p} N_b}{2\pi A_p} \tag{3.31}$$

where N_b indicates the number of blades, and A_p is the cell area in the projected blade zone.

The coupling algorithm and the explanation of body forces for 3-D models can be found in (Kinnas et al. 2010, 28th SNH). More applications of this hybrid scheme by using a vortex lattice method coupling with either a Euler solver or a RANS solver to the ducted and podded propellers and the interaction between the front and after propellers in the twin-type propeller cases can be found (Gu 2006; Gupta 2004; Kinnas et al. 2004; Kinnas et al. 2006; Kinnas et al. 2007b; Kinnas et al. 2009; Kinnas et al. 2012a).

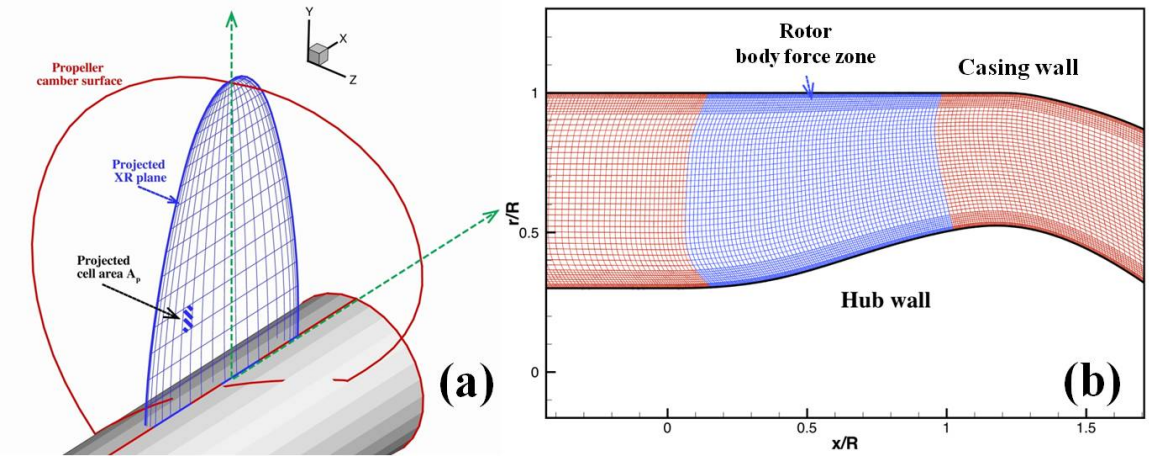

Figure 3.6: (a) Projected propeller zone (body force zone) and (b) an example of axisymmetric mesh near the projected propeller zone area.

3.8 THE TIP GAP MODEL

In order to incorporate the clearance flow model inside a tip gap region of a water-jet, an appropriate expression for the correct leakage volume flow through the gap should be achieved. A 2-D orifice equation model is used in which the velocity can be related to the pressure difference across the tip region of the blade by applying Bernoulli's obstruction theory in the present method. Following the work by Hughes (1997), the reduction in the flow from losses in the orifice can be defined in terms of an empirical determined discharge coefficient (C_Q) representing the relationship between the flow rate Q and the pressure difference Δp across the gap size h:

$$C_Q = \frac{Q}{h}\sqrt{\frac{\rho}{2\Delta p}} \tag{3.32}$$

The mean velocity V_{gap} through the gap region at a given chordwise location can be expressed as:

$$V_{gap} = C_Q\sqrt{\frac{2\Delta p}{\rho}} = C_Q\left|\vec{V}_{in}\right|\sqrt{\Delta C_P} \tag{3.33}$$

where $\vec{\mathrm{V}}_{\mathrm{in}}$ is the local inflow velocity relative to the blade, and ΔC_P is the pressure coefficient on the blade tip, which is defined as:

$$\Delta C_P = \frac{\Delta p}{0.5\rho\left|\vec{V}_{in}\right|^2} \tag{3.34}$$

To incorporate the gap model into the panel method, an additional row of fictitious panels will be needed to close the tip gap region as shown in Figure 3.7. To combine Equation (3.33) with the kinematic boundary condition, the sources strength in the gap zone becomes:

$$\frac{\partial \phi_q}{\partial n_q} = -\vec{V}_{in}\cdot\vec{n}_q + C_Q\left|\vec{V}_{in}\right|\sqrt{\Delta C_P}\,(\vec{n}_q\cdot\vec{n}_{camber}) \tag{3.35}$$

where $\vec{n}_q$ is the unit normal vector to the panel surface, and $\vec{n}_{camber}$ is the unit normal vector to the mean camber surface at the blade tip at the same chordwise location as the panels. The value for pressure jump ΔC_P between pressure and suction sides is obtained by an "iterative procedure." The problem for the potential distributions on the rotor blade is first solved as if the gap were completely sealed by using Equation (3.9) to specify the source strengths for the gap panels. The pressure distribution is then computed by differentiating the perturbation potentials using finite difference scheme. The value of ΔC_P is taken to be the difference between C_P on the pressure side and suction side of the blade tip panels (they are panels closest to the rotor tip) at the chordwise location. The problem for the perturbation potentials on the rotor blade is then solved again with the boundary condition on the gap panels now specified by Equation (3.35). The pressures on the rotor are then recalculated and used to update the boundary condition on the gap panels. The solution converges within 30 iterations.

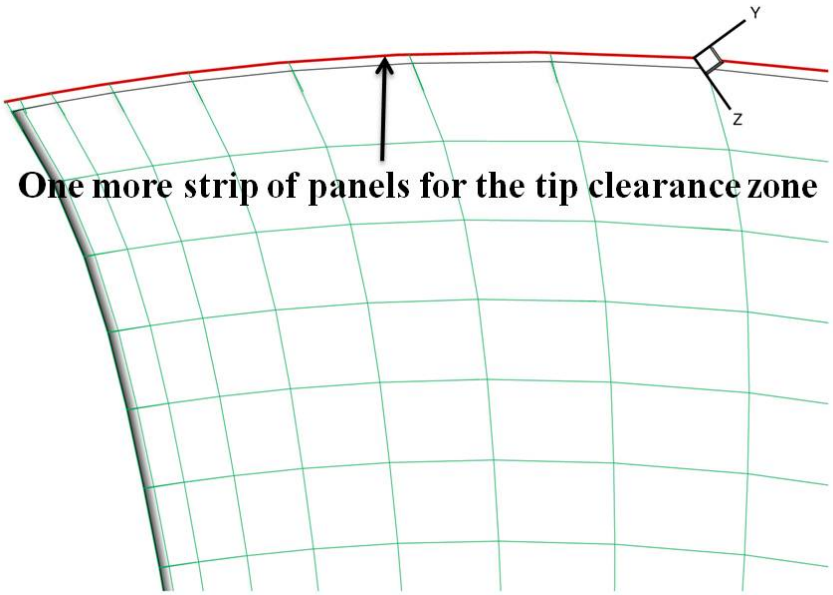

Figure 3.7: Additional row of panels for ONR-AxWJ2 water-jet rotor blade with the gap size of 0.33% of the blade radius (red curve: inner surface of the casing).

3.9 THE STEADY WAKE ALIGNMENT ON THE ROTOR PROBLEM

A pitch alignment model is used on the trailing wake of the rotor originally. In order to improve the prediction of the rotor performance, the influences of the rotor, hub and casing on the wake have to be included in the simulation. To align the wake, the induced velocities on the wake surface by those components are evaluated by Equation (3.36) as follows:

$$\begin{aligned}\vec{q}_{induced} = & \frac{1}{4\pi}\iint_{S_R}\left[\phi_q\nabla\left(\frac{\partial G(p;q)}{\partial n_q}\right)-\nabla G(p;q)\frac{\partial\phi_q(t)}{\partial n_q}\right]dS + \\ & \frac{1}{4\pi}\iint_{S_{Hub}}\left[\phi_q\nabla\left(\frac{\partial G(p;q)}{\partial n_q}\right)-\nabla G(p;q)\frac{\partial\phi_q(t)}{\partial n_q}\right]dS + \\ & \frac{1}{4\pi}\iint_{S_{Casing}}\left[\phi_q\nabla\left(\frac{\partial G(p;q)}{\partial n_q}\right)-\nabla G(p;q)\frac{\partial\phi_q(t)}{\partial n_q}\right]dS + \\ & \frac{1}{4\pi}\iint_{S_{RW}}\Delta\phi_{RW}\nabla\left(\frac{\partial G(p;q)}{\partial n_q}\right)dS\end{aligned} \tag{3.36}$$

The procedure of the wake alignment is carried out in an iterative manner, and the hub and casing surfaces are re-paneled. The overview of the iterative procedure of steady wake alignment is shown in Figure 3.8.

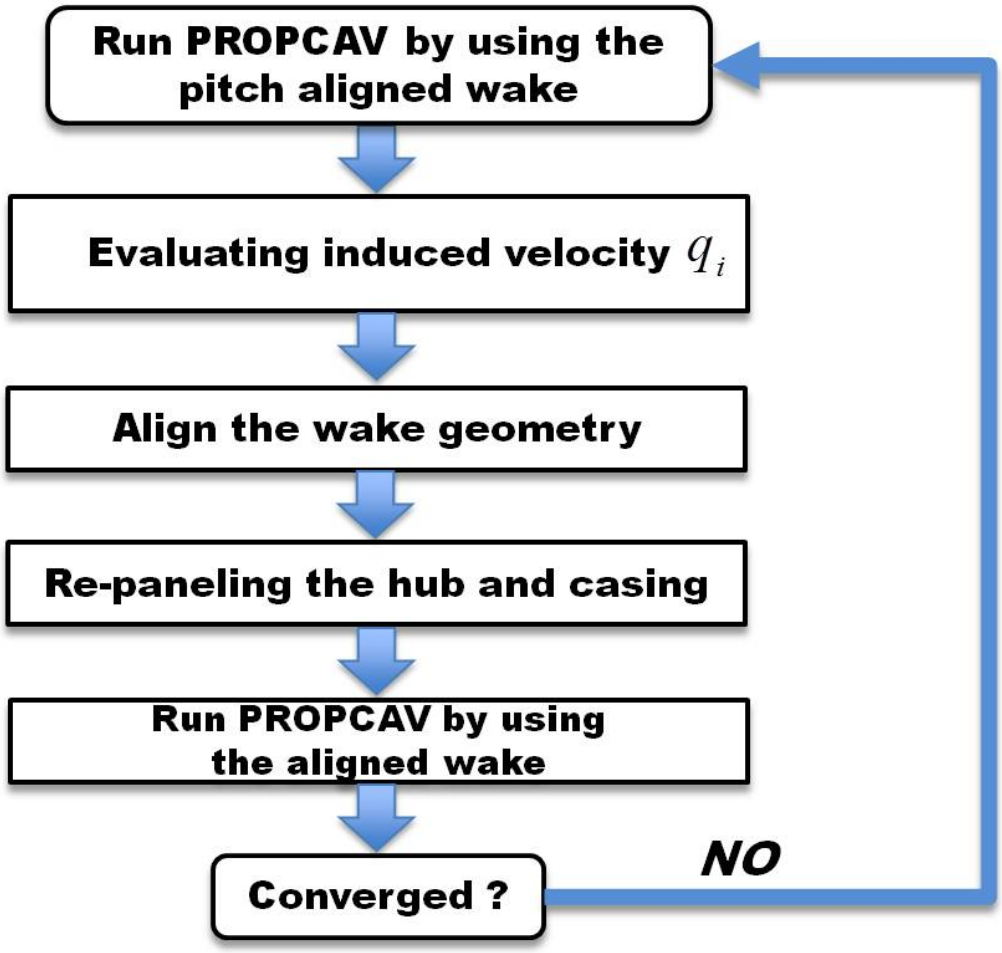

Figure 3.8: Iterative procedure for ONR AxWJ2 rotor steady wake alignment.

Chapter 4: Numerical Validation of the Present Method

The purpose of this chapter is to show the present numerical method to be convergent and consistent. The steady rotor problem and steady stator problem as well as the rotor induced swirl velocity on the stator are validated. The numerical results from the present method are compared against either those calculated from a commercial CFD software ANSYS FLUENT or those obtained from the experimental observations.

4.1 THE ROTOR ONLY PROBLEM

In this section, only rotors inside ONR AxWJ2 water-jet pump are simulated. Convergence studies for the rotor only problem with the number of elements on the blade, number of elements along the casing, number of circumferential panels on the hub and casing between two blades and the length and the angle increment of the rotor trailing wake are investigated. The non-dimensional circulation (Γ) on the blade is defined as following:

$$\Gamma = \Delta\phi / 2\pi R\sqrt{V_S^2 + (0.7\pi nD)^2} \tag{4. 1}$$

where $\Delta\phi$ indicates the potential jump across the trailing wake at each blade section. V_S is the ship speed and n is the rotor rotational frequency (rev/s).

Convergence Study on Steady Fully-wetted Calculation

The dependences of fully-wetted circulation distributions on the rotor blade at J_S=1.19 with different number of panels in the chord-wise direction and span-wise direction of the blade are shown in Figure 4.1 and 4.2, respectively. As shown in Figure 4.1, the circulation distributions are consistent except the slight differences from the result of 50 elements in the chord-wise direction. In Figure 4.2, the circulation

distributions are also consistent in addition to minor discrepancies from those of 15 elements in the span-wise direction. The number of circumferential elements is 20 between two blades on the hub and casing while doing these two convergence tests. Changing the number of panels on the blade affects slightly the circulation distributions of the rotor.

Figure 4.3 shows the convergence of the rotor circulation distributions with number of panels in the circumferential direction between two blades. This convergence test is more demanding than the previous two since the number of circumferential elements affects the blade loading more significantly. The figure shows that using at least 20 elements in the circumferential direction is sufficient for achieving convergent results.

Figure 4.4 presents the convergence of the rotor circulation distributions with the panel size of the rotor trailing wake. Five different angel increments, $\Delta\theta = 2^{\circ}, 3^{\circ}, 4^{\circ}, 6^{\circ}$ and 8° for the wake geometry are used. The convergence of the results is satisfactory and not affected by the wake angel increments evidently.

Figure 4.5 shows the effects of wake length on the convergence of the rotor loading. From the convergent results, the extension of the rotor trailing wake has no major influence on the rotor circulation distributions.

In addition, the effects of the number of panels on the casing to the convergence of the present method are investigated. The legend, *Casing 154×20*, indicates that 154 panels is used along the axial direction while the number of circumferential elements is kept as 20. As shown in Figure 4.6, the number of panels along the axial direction on the casing affects slightly on the convergence of the results.

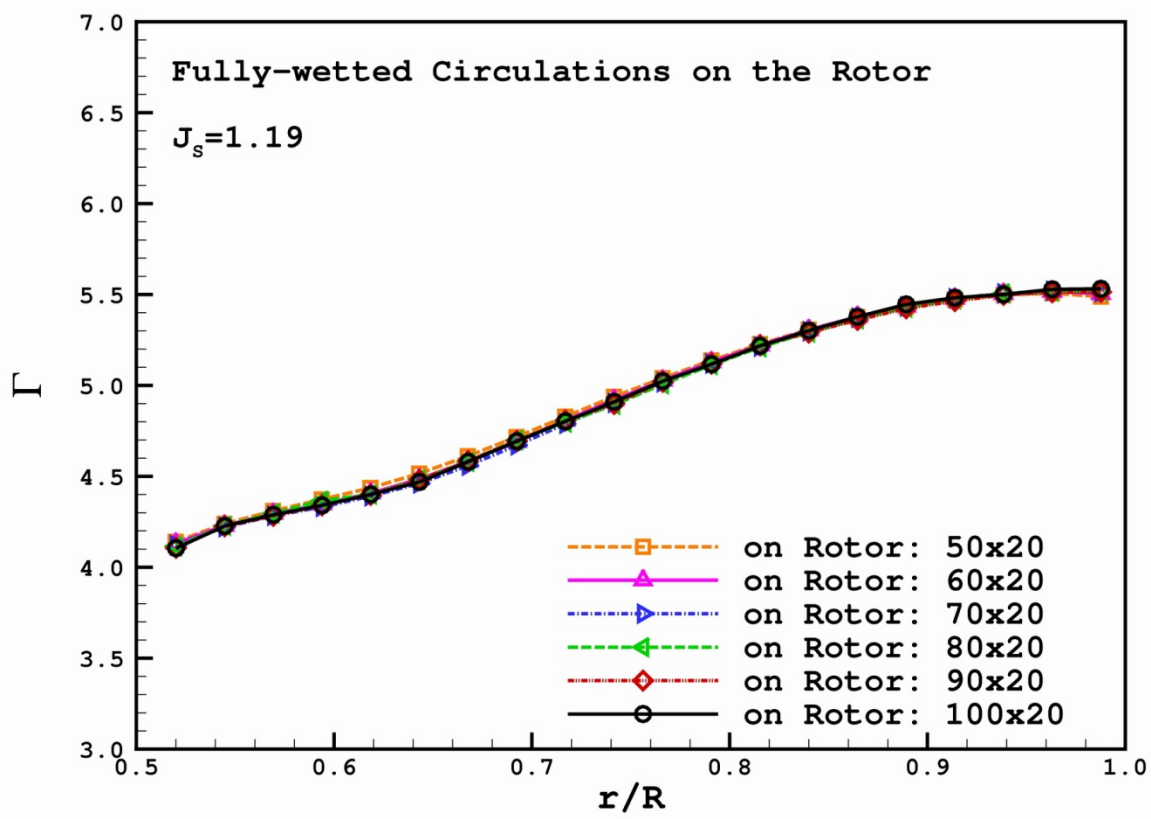

Figure 4.1: Convergence of fully-wetted circulation distributions on the rotor of the ONR AxWJ2 water-jet with different number of panels in the chord-wise direction of the blade. J_S=1.19. Number of panels in the circumferential direction is 20.

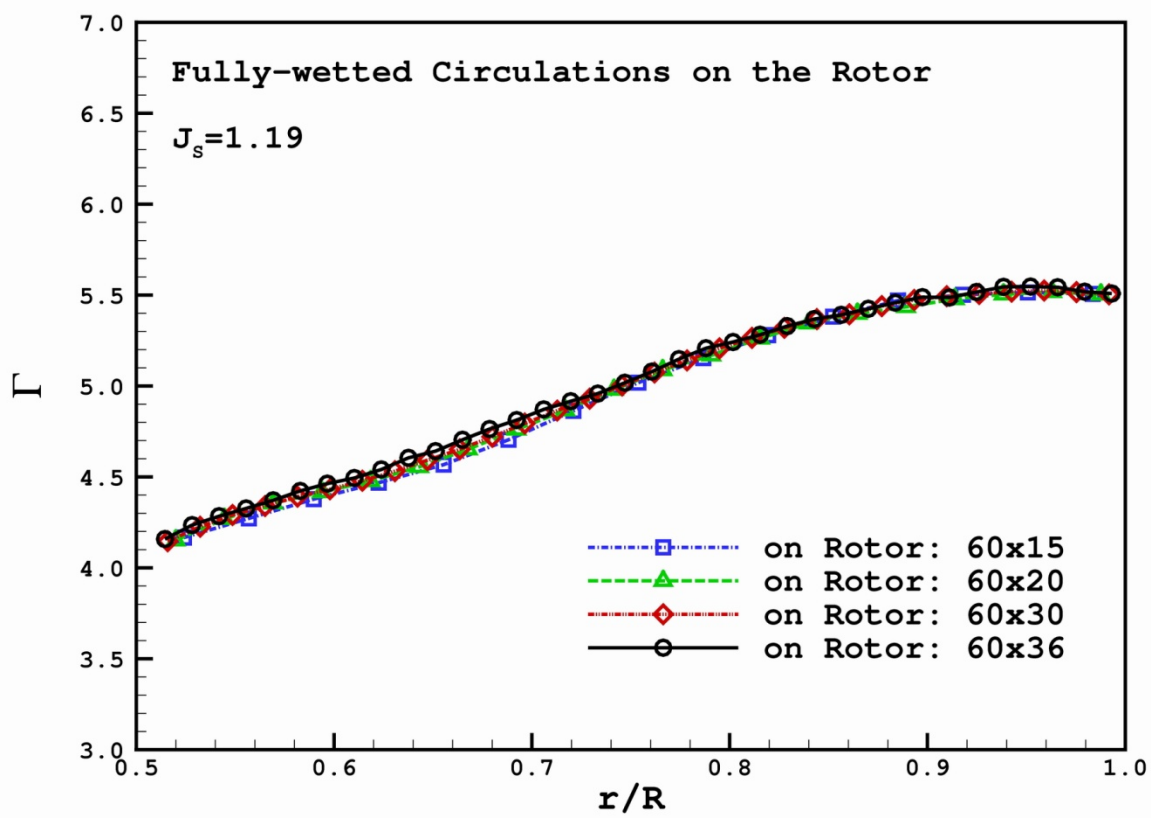

Figure 4.2: Convergence of fully-wetted circulation distributions on the rotor of the ONR AxWJ2 water-jet with different number of panels in the span-wise direction of the blade. J_S=1.19. Number of panels in the circumferential direction is 20.

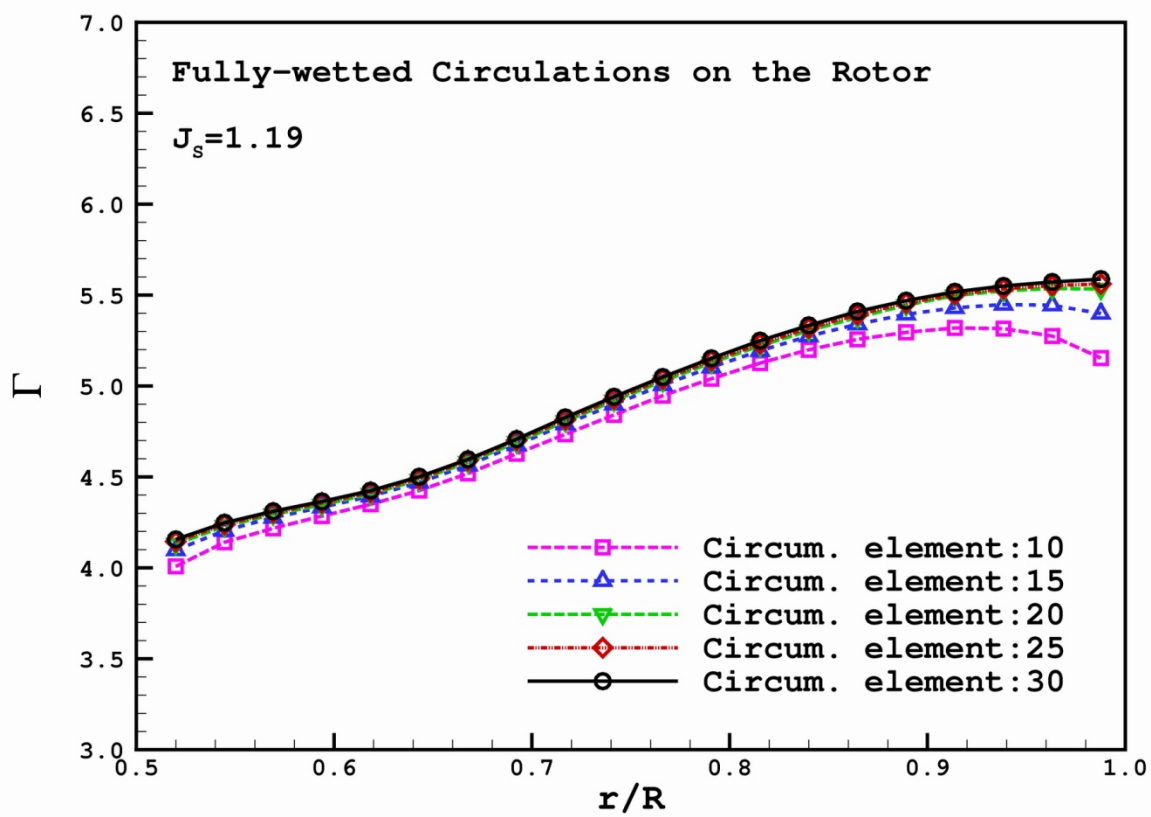

Figure 4.3: Convergence of fully-wetted circulation distributions on the rotor of the ONR AxWJ2 water-jet with different number of panels in the circumferential direction between two blades. J_S=1.19. *NN*×*MM* on the blade is 60×20.

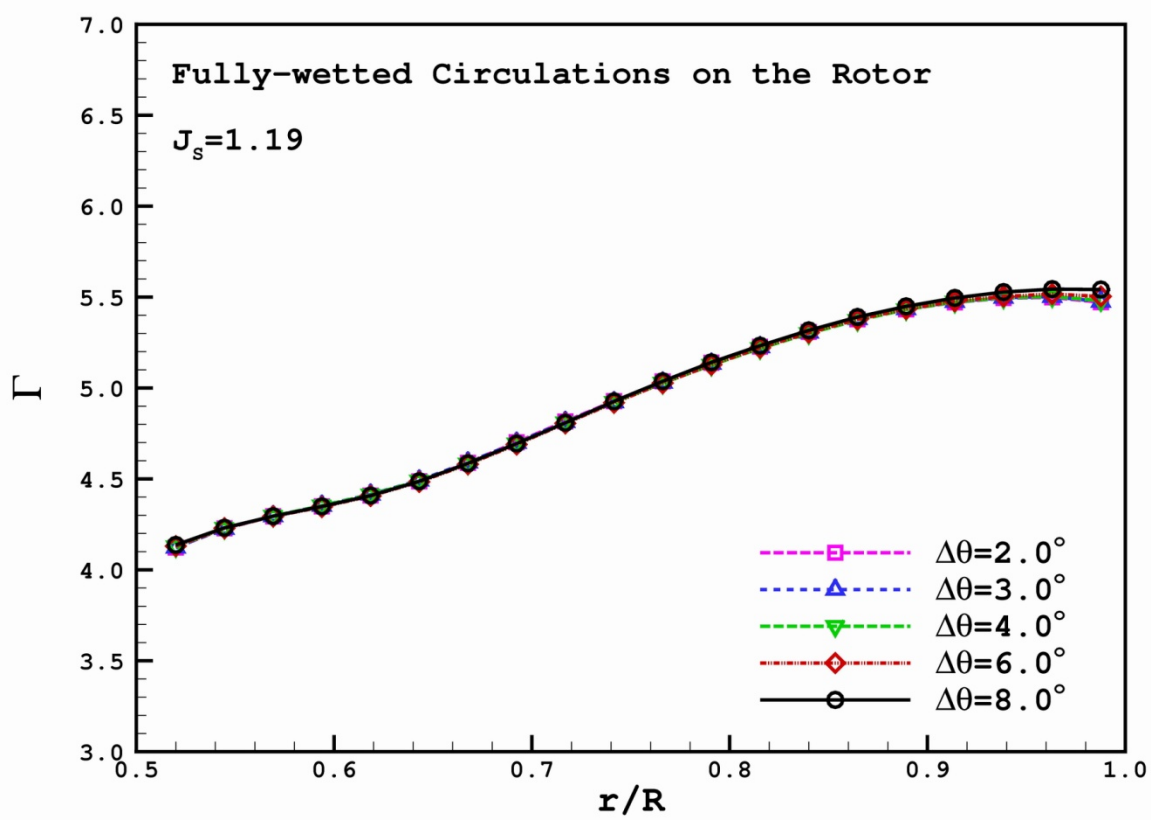

Figure 4.4: Convergence of fully-wetted circulation distributions on the rotor of the ONR AxWJ2 water-jet with different panel size of the rotor trailing wake. J_S=1.19. Number of panels in the circumferential direction is 20. *NN*×*MM* on the blade is 60×20.

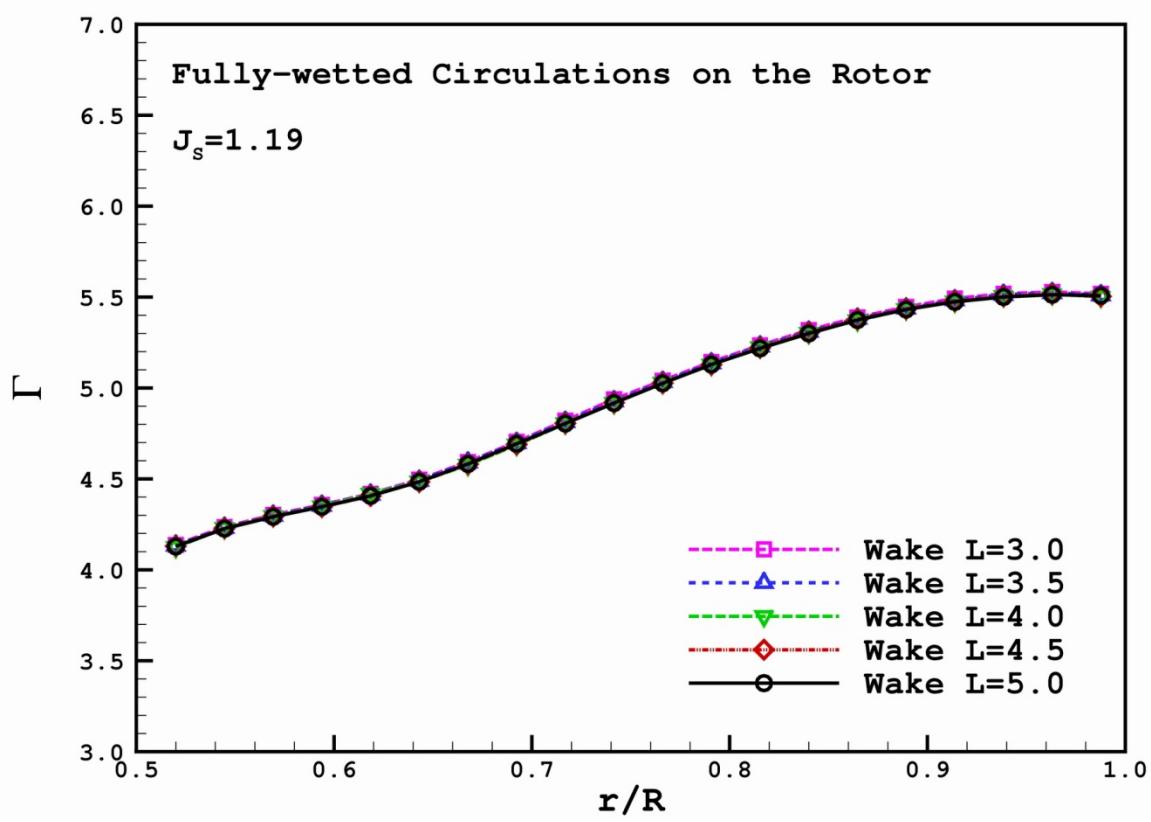

Figure 4.5: Convergence of fully-wetted circulation distributions on the rotor of the ONR AxWJ2 water-jet with different length of the rotor trailing wake. J_S=1.19. Number of panels in the circumferential direction is 20. *NN*×*MM* on the blade is 60×20 and Δθ=6°.

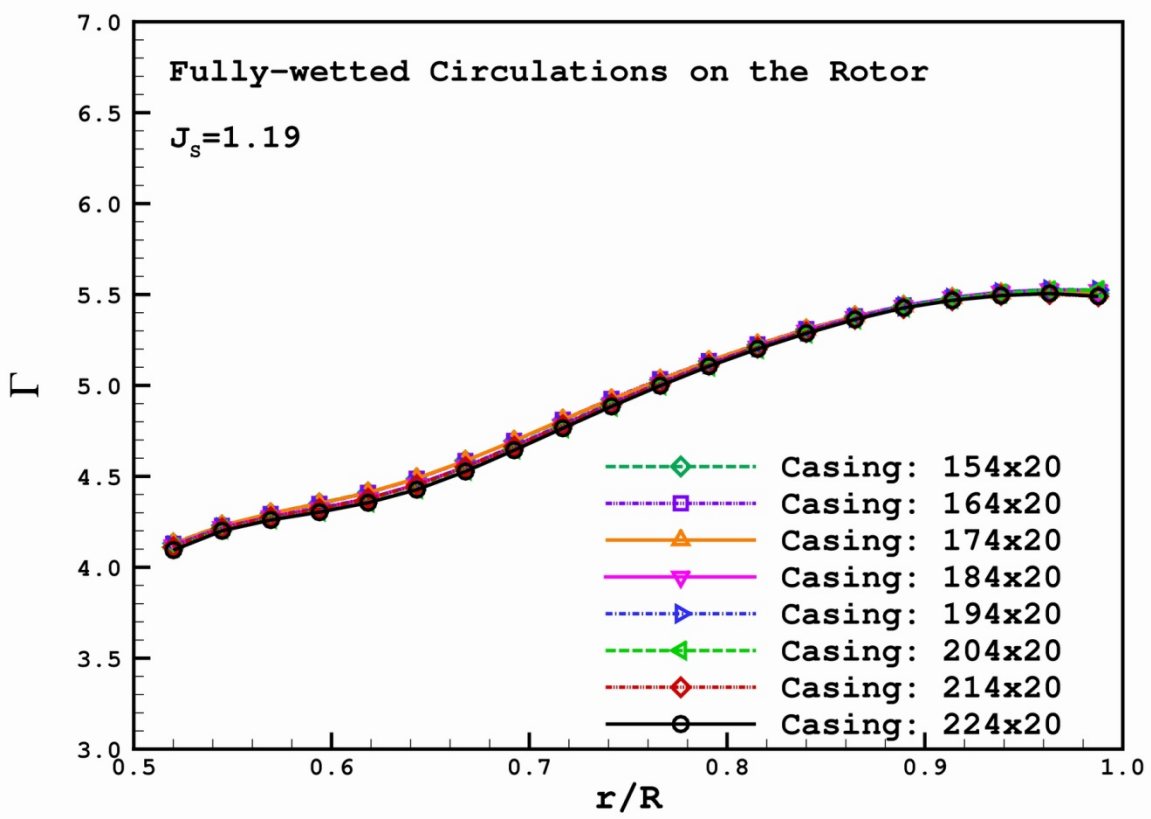

Figure 4.6: Convergence of fully-wetted circulation distributions on the rotor of the ONR AxWJ2 water-jet with number of panels on the casing. J_S=1.19. Number of panels in the circumferential direction is 20. *NN*×*MM* on the blade is 60×20 and Δθ=6°. Wake length is 4.50.

Convergence Study on Steady Partial Cavitating Calculation

The convergence of cavitating circulation distributions of the rotor is shown in Figure 4.7. The number of circumferential panels between two blades on the hub and casing is kept the same as 20 elements, and changing the number of panels on the blade does not affect the blade circulations significantly. The sensitivity of the cavity patterns with number of panels on the rotor is investigated at J_S=0.988 (Q^*=0.706) and σ_n = 1.13 (N^*=1.046) and compared with that from the experimental observation as shown in Figure 4.8. Except for very slight differences in the cases of 60x20 and 80x20 on the rotor blade, the present method predicts very similar results regardless of the number of panels on the rotor.

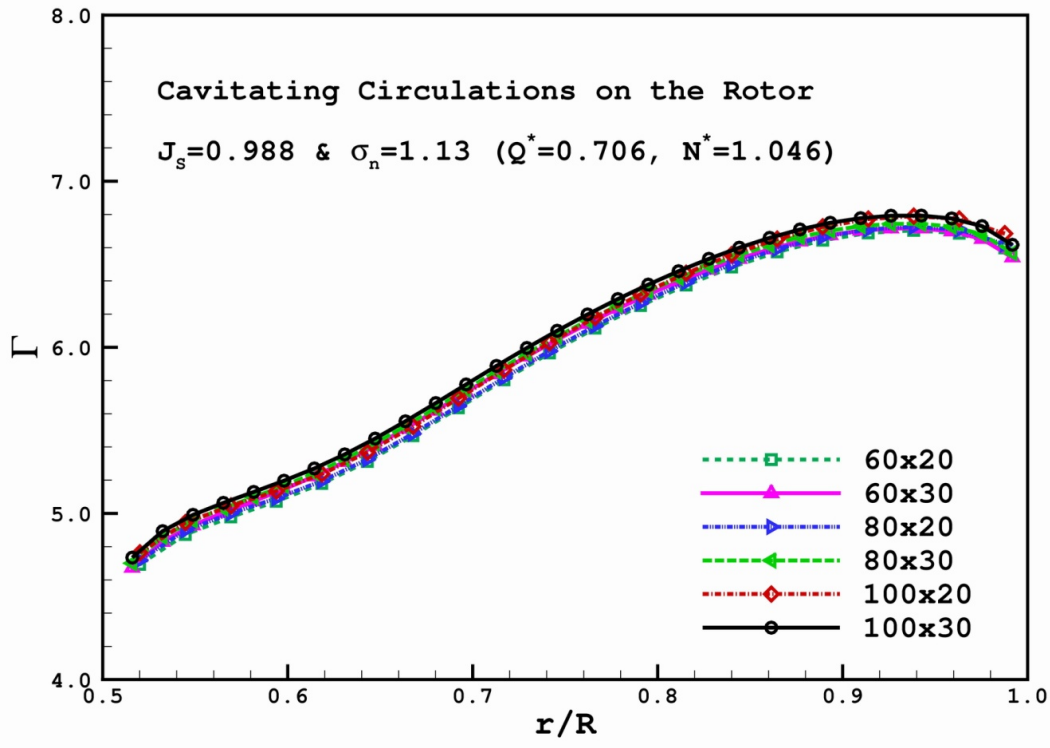

Figure 4.7: Convergence of cavitating circulation distributions with number of panels on the rotor blade of the ONR AxWJ2 water-jet. J_S=0.988 (Q^*=0.706) and σ_n = 1.13 (N^*=1.046). Number of panels in the circumferential direction is 20. $\Delta\theta$=6°. Wake length is 4.50.

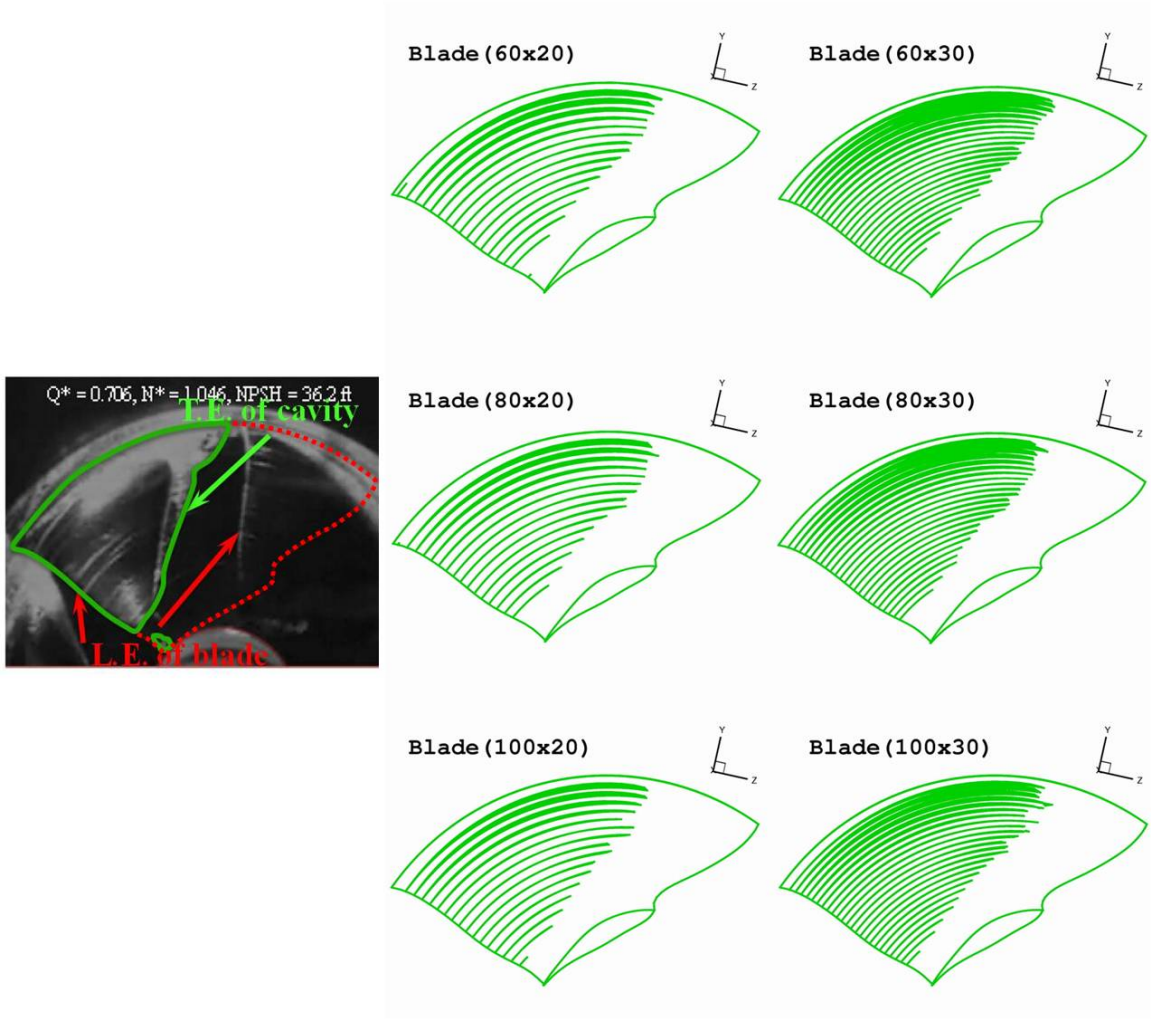

Figure 4.8: Convergence of the cavity patterns on the rotor of the ONR AxWJ2 water-jet with different number of panels on the blade and the comparison with the observation of the experiment. J_S=0.988 (Q^*=0.706) and σ_n = 1.13 (N^*=1.046). Number of panels in the circumferential direction is 20. $\Delta\theta$=6°. Wake length is 4.50.

Convergence Study on Steady Super Cavitating Calculation

The convergences of fully-wetted and super-cavitating circulation distributions of the rotor are shown in Figure 4.9 and 4.10, respectively. The number of circumferential panels between two blades on the hub and casing is still kept the same as 20 elements. Changing the number of panels on the blade affects slightly the circulation distributions of the rotor. The sensitivity of the cavity patterns with different number of panels on the rotor is investigated at J_S=0.96 and σ_n = 0.80 as shown in Figure 4.11. Except for the slight differences around the tail of cavity at each section, the present method predicts very similar results regardless of the number of panels on the rotor.

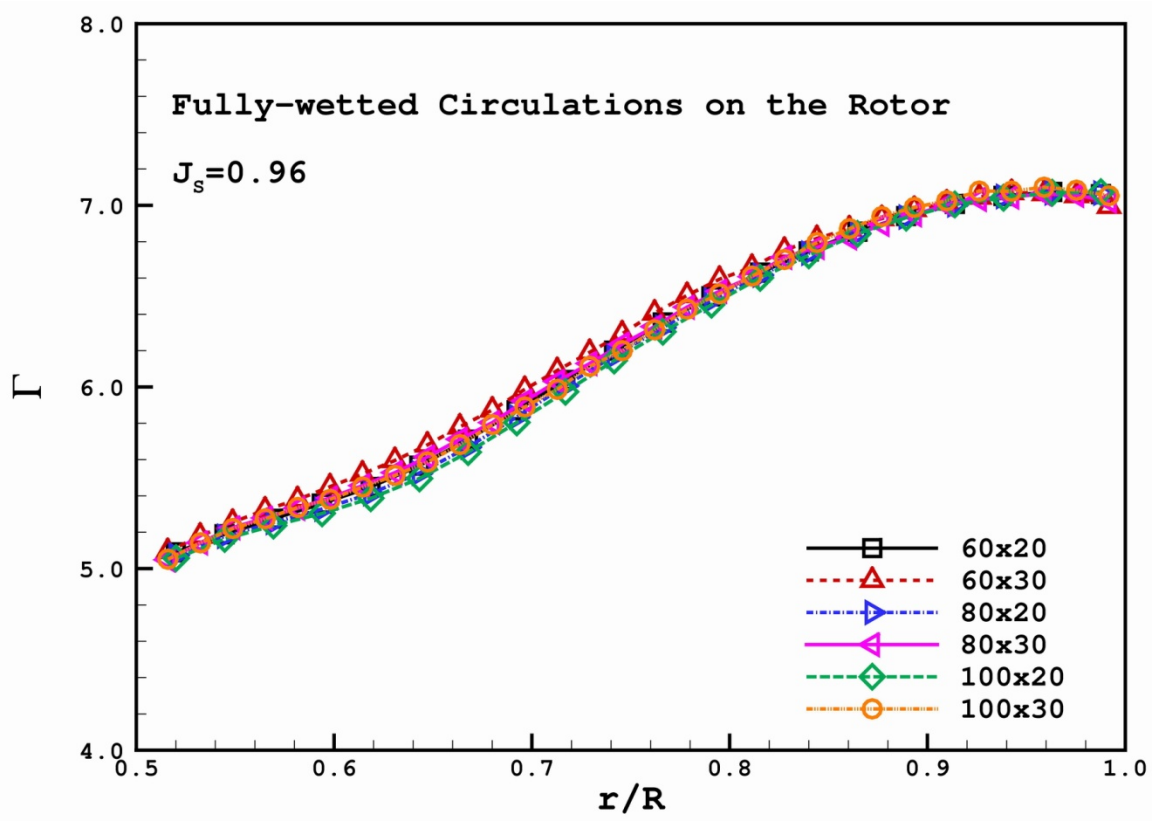

Figure 4.9: Convergence of fully-wetted circulation distributions with number of panels on the rotor blade of the ONR AxWJ2 water-jet. J_S=0.96. Number of panels in the circumferential direction is 20. Δθ=6°. Wake length is 4.50.

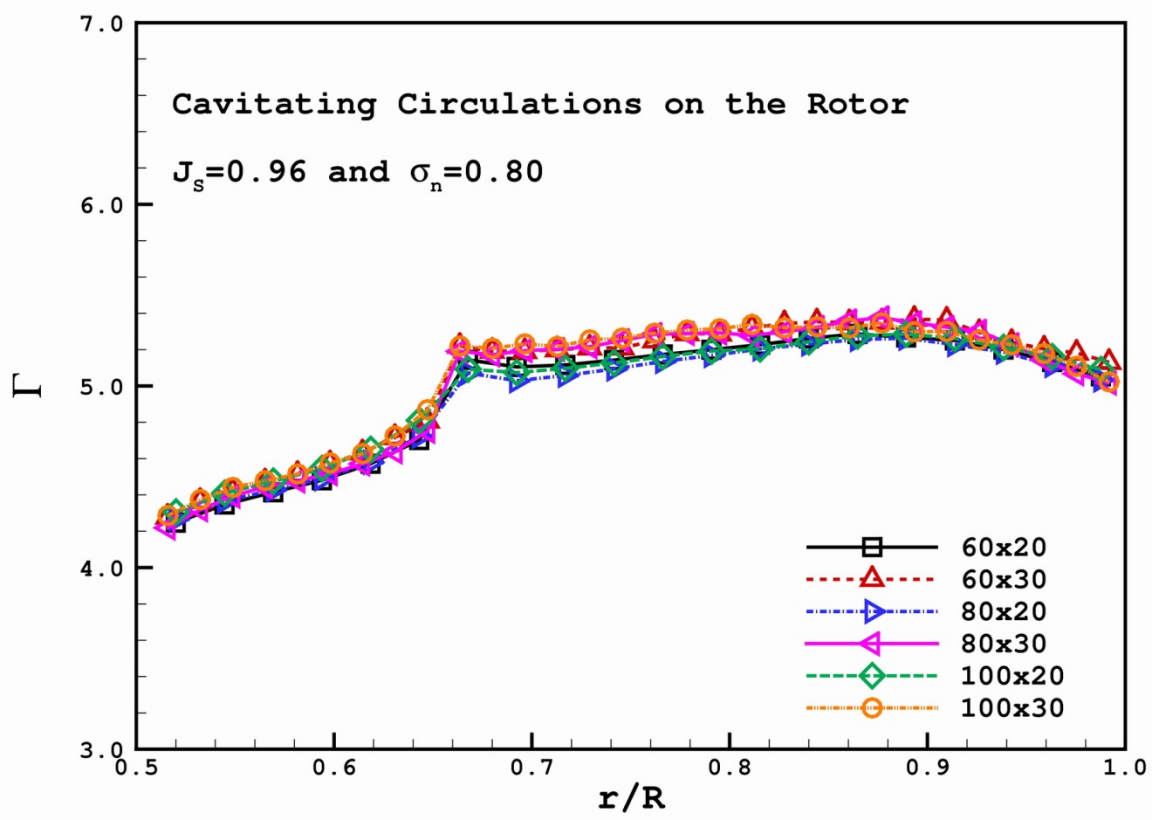

Figure 4.10: Convergence of super-cavitating circulation distributions with number of panels on the rotor blade of the ONR AxWJ2 water-jet. J_S=0.96 and σ_n = 0.80. Number of panels in the circumferential direction is 20. Δθ=6°. Wake length is 4.50.

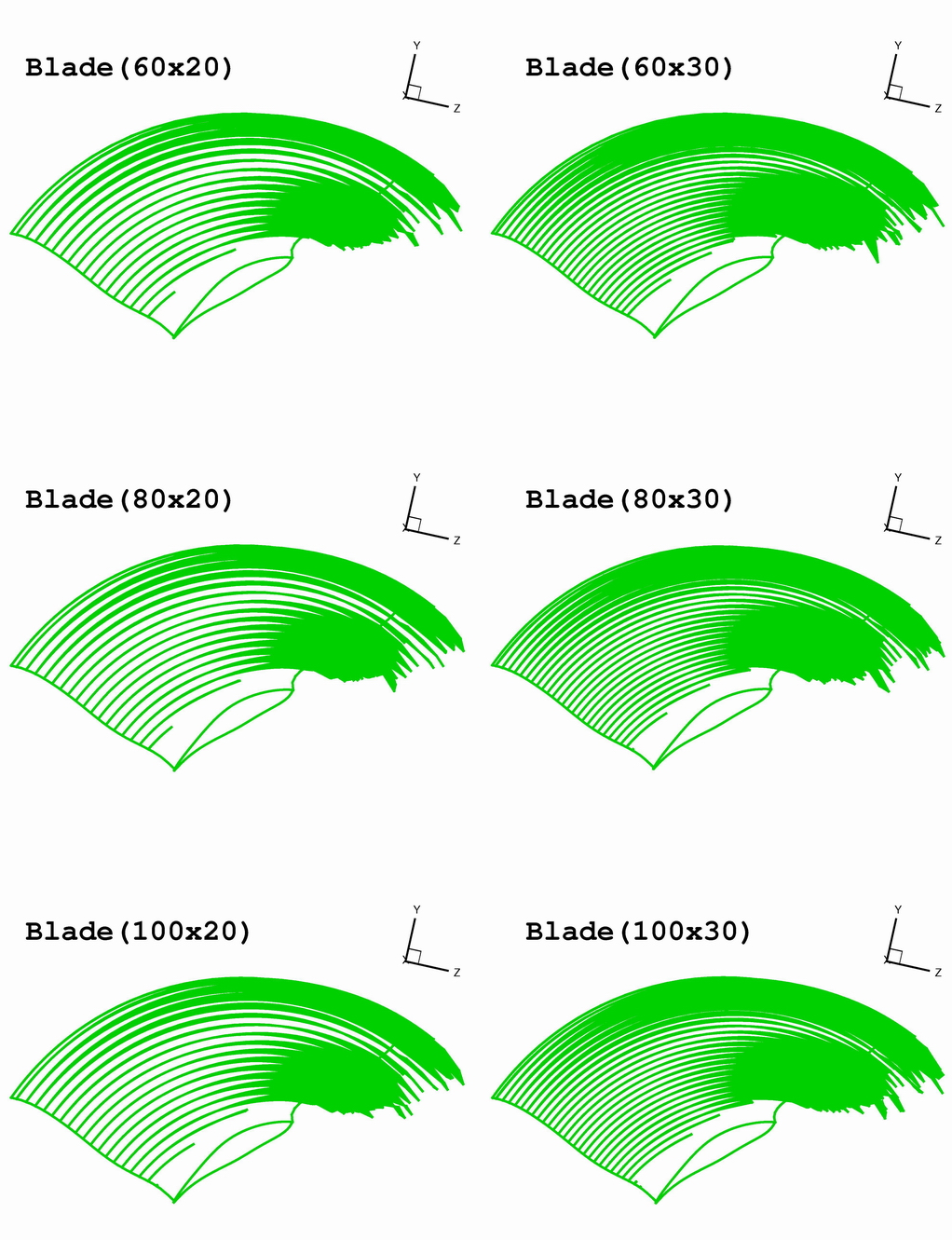

Figure 4.11: Convergence of the cavity patterns on the rotor blade of the ONR AxWJ2 water-jet with number of panels in the chord-wise and span-wise directions. J_S=0.96 and σ_n = 0.80. Number of panels in the circumferential direction is 20. $\Delta\theta$=6°. Wake length is 4.50.

4.2 THE STATOR ONLY PROBLEM

This section presents the grid dependence studies in the case of having only stators inside ONR AxWJ2 water-jet pump. Convergence studies for the stator only problem with the number of elements on the blade, number of elements along the casing, number of circumferential panels on the hub and casing between two blades and the length and the angle increment of the rotor trailing wake are investigated. The non-dimensional circulation (Γ_S) on the blade is defined as following:

$$\Gamma = \Delta\phi / 2\pi R V_S \tag{4. 2}$$

where $\Delta\phi$ indicates the potential jump across the trailing wake at each blade section. V_S is the ship speed.

Convergence Study on Steady Fully-wetted Calculation

The dependences of fully-wetted circulation distributions on the stator at J_S=1.19 with different number of panels in the chord-wise direction and span-wise direction of the blade are shown in Figure 4.12 and 4.13, respectively. As shown in Figure 4.12, except the slight differences from the result of 50 and 60 elements in the chord-wise direction, the circulation distributions are consistent. In Figure 4.13, the circulation distributions are also consistent except somewhat discrepancies from those of 15 elements in the span-wise direction. The 20 circumferential elements are used between two blades on the hub and casing while doing these two convergence tests. Changing the number of panels on the stator blade does not affect the circulation distributions significantly.

Figure 4.14 shows the convergence of the stator circulation distributions with number of panels in the circumferential direction between two blades. The figure shows slight discrepancies of the results close to the stator tip, and using at least 20 elements in the circumferential direction is sufficient for achieving convergent results.

Figure 4.15 presents the convergence of the stator circulation distributions with the panel size of the stator trailing wake. Five different angel increments, $\Delta\theta = 2^{\circ}, 3^{\circ}, 4^{\circ}, 6^{\circ}$ and 8° for the wake geometry are used. The convergence of the results is satisfactory and not affected by the wake angel increments evidently.

Figure 4.16 shows the effects of wake length on the convergence of the stator circulations. The extension of the stator trailing wake has no major influence on the stator loading.

The effects of the number of panels on the casing to the convergence of the present method are also investigated. The legend, *Casing: 224×20*, indicates that 224 panels is used along the axial direction while the number of circumferential elements is kept as 20. As shown in Figure 4.17, the number of panels along the axial direction on the casing affects slightly on the convergence of the results.

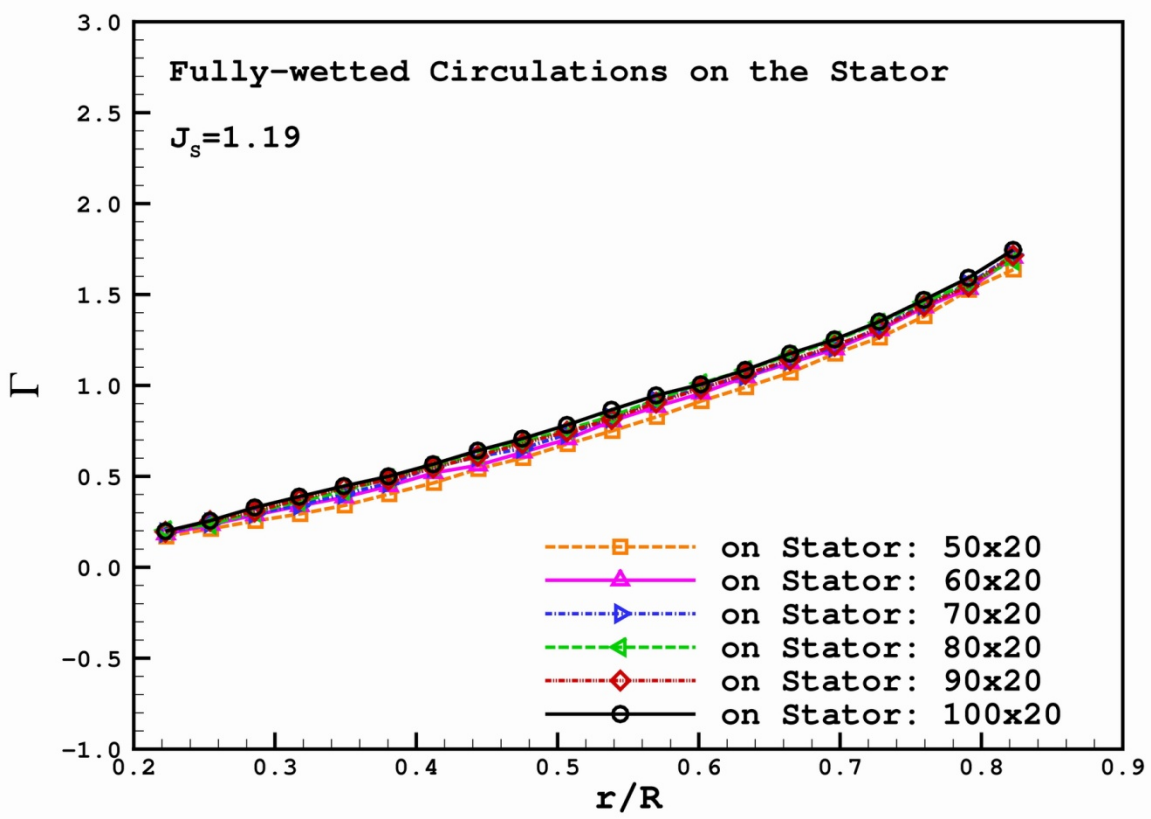

Figure 4.12: Convergence of fully-wetted circulation distributions on the stator of the ONR AxWJ2 water-jet with different number of panels in the chord-wise direction of the blade. J_S=1.19. Number of panels in the circumferential direction is 20. $\Delta\theta$=6°. Wake length is 4.50.

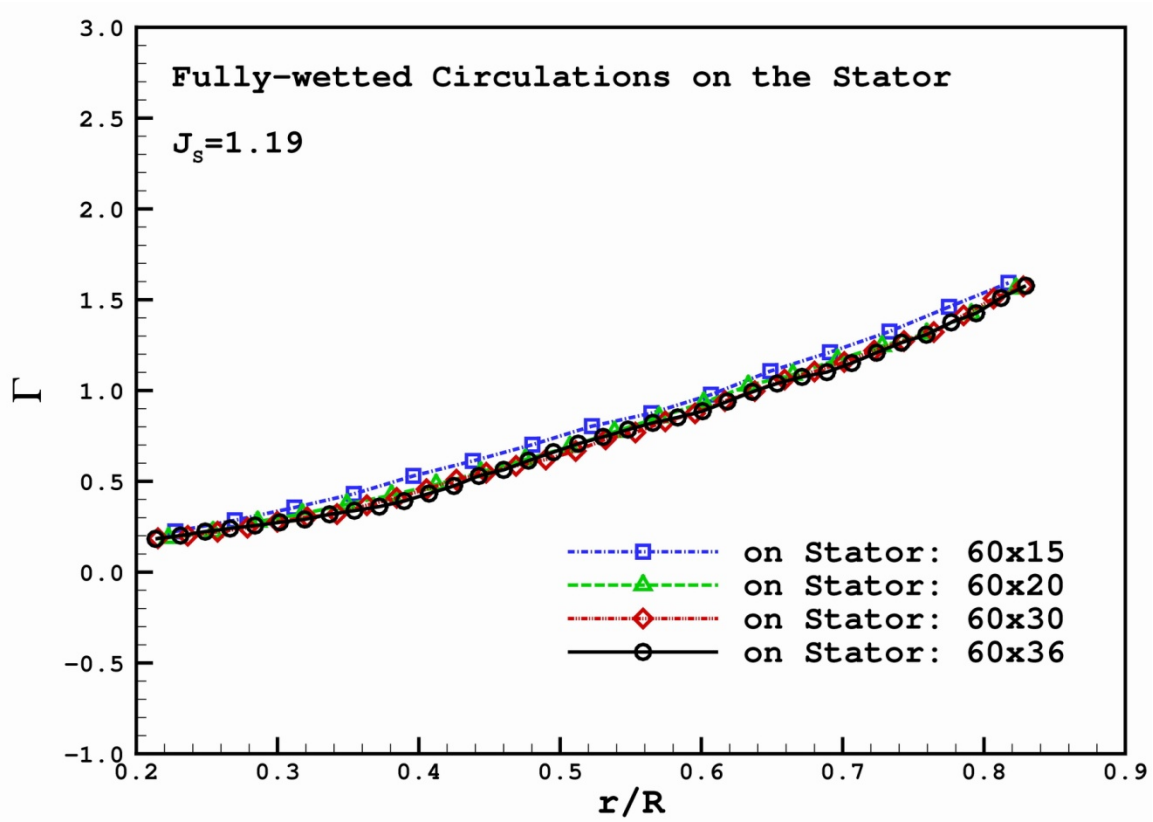

Figure 4.13: Convergence of fully-wetted circulation distributions on the stator of the ONR AxWJ2 water-jet with different number of panels in the span-wise direction of the blade. J_S=1.19. Number of panels in the circumferential direction is 20. $\Delta\theta$=6°. Wake length is 4.50.

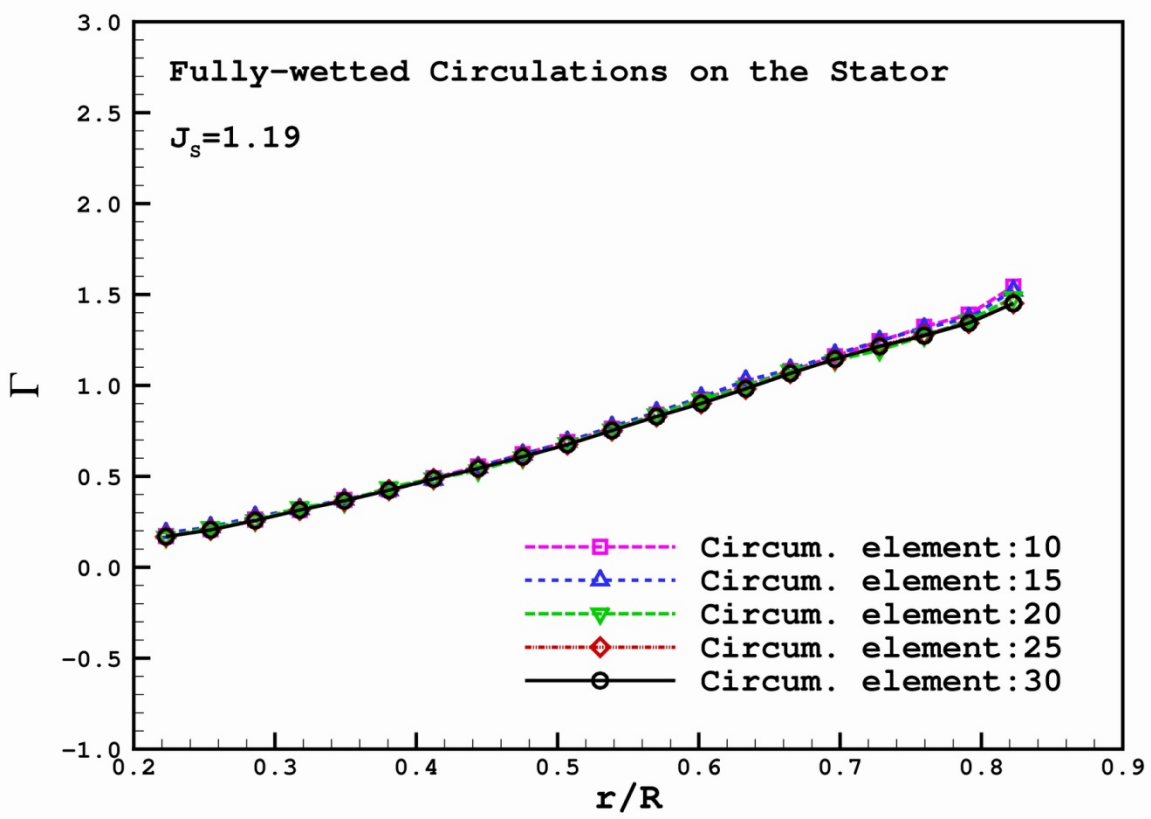

Figure 4.14: Convergence of fully-wetted circulation distributions on the stator of the ONR AxWJ2 water-jet with different number of panels in the circumferential direction between two blades. J_S=1.19. $NN \times MM$ on the blade is 60×20 and $\Delta\theta$=6°. Wake length is 4.50.

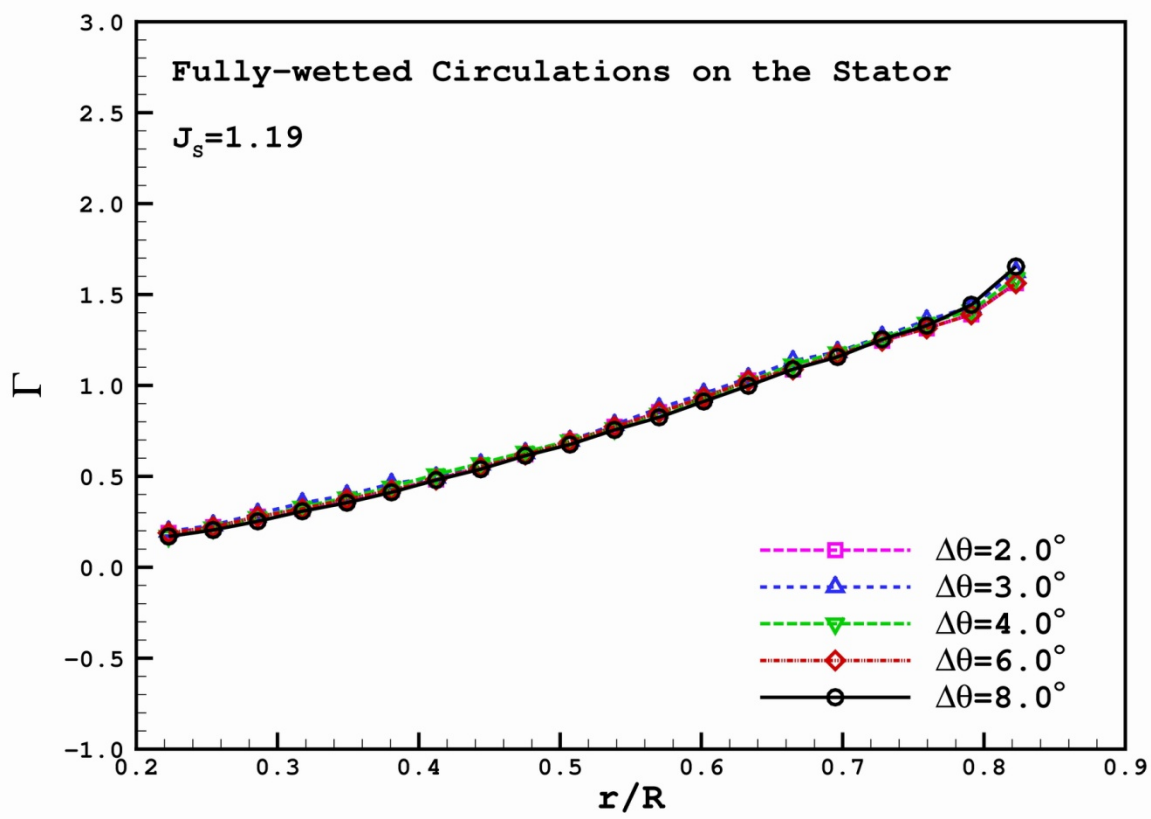

Figure 4.15: Convergence of fully-wetted circulation distributions on the stator of the ONR AxWJ2 water-jet with different panel size of the stator trailing wake. J_S=1.19. Number of panels in the circumferential direction is 20. *NN*×*MM* on the blade is 60×20 and wake length is 4.50.

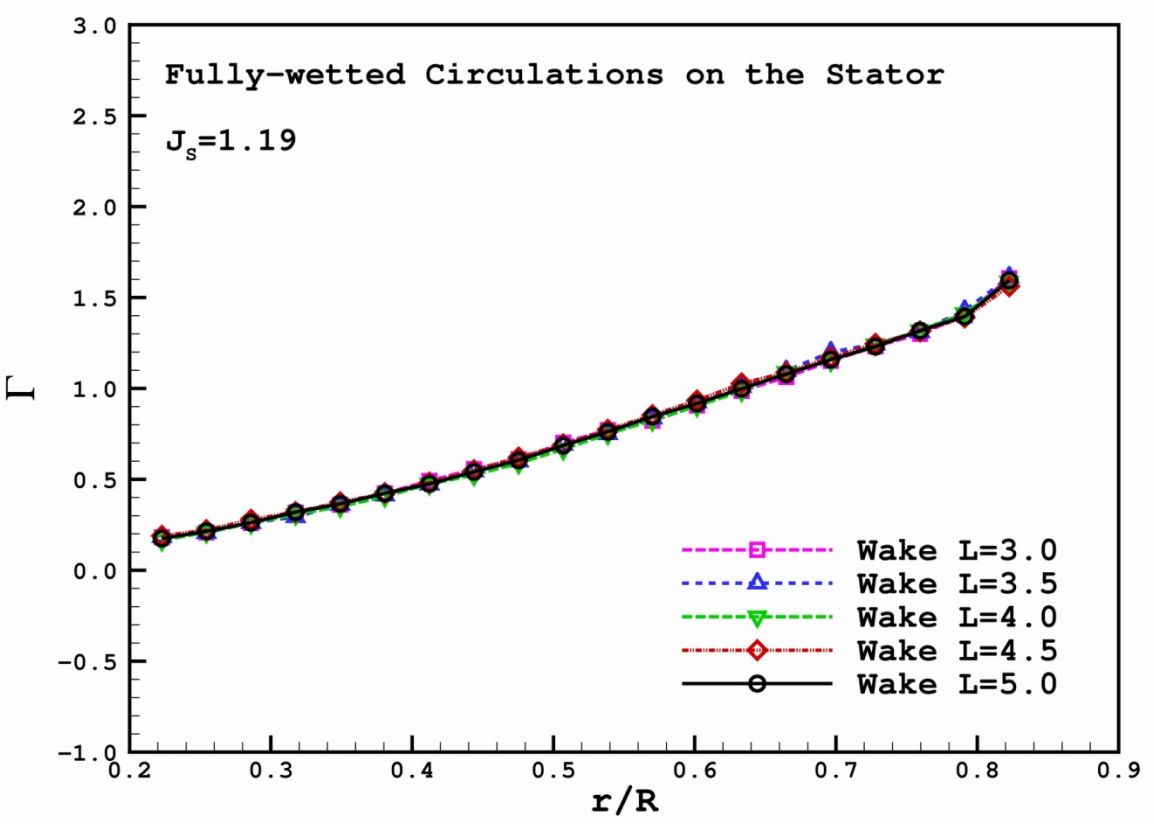

Figure 4.16: Convergence of fully-wetted circulation distributions on the stator of the ONR AxWJ2 water-jet with different length of the stator trailing wake. J_S=1.19. Number of panels in the circumferential direction is 20. $NN \times MM$ on the blade is 60×20 and $\Delta\theta$=6°.

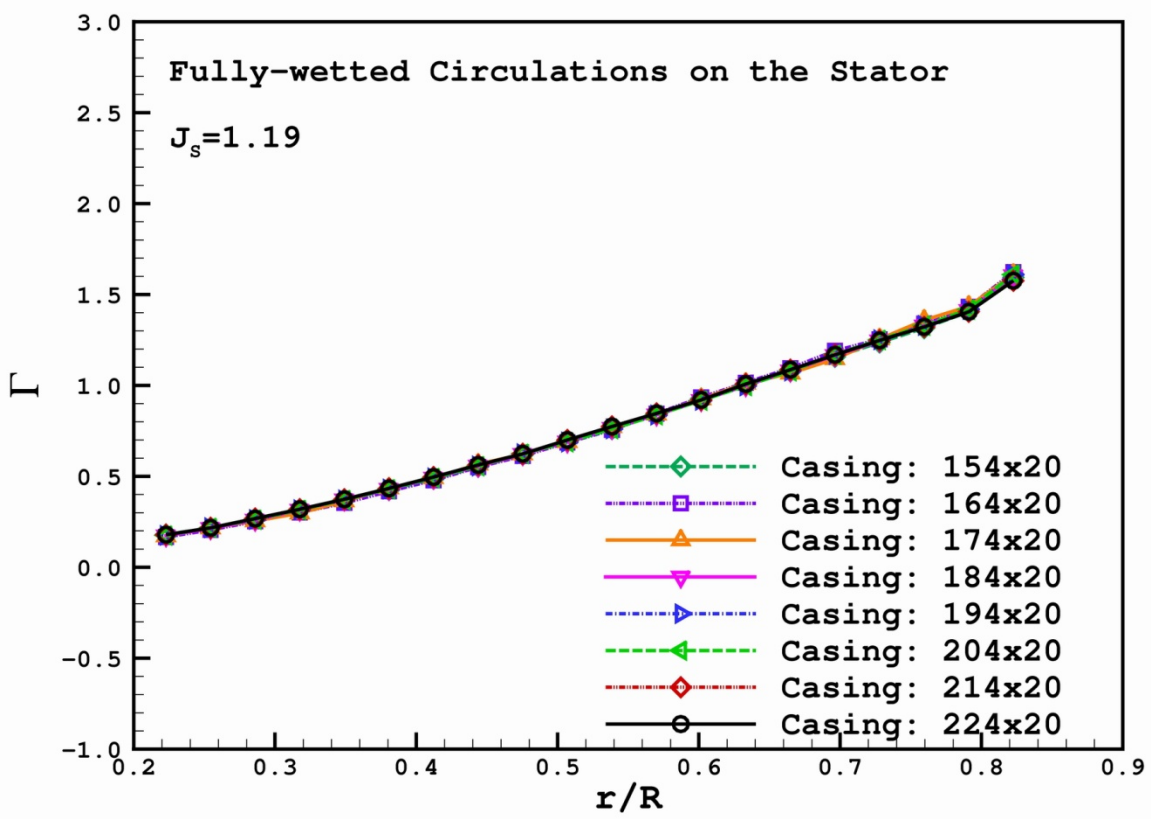

Figure 4.17: Convergence of fully-wetted circulation distributions on the stator of the ONR AxWJ2 water-jet with number of panels on the casing. J_S=1.19. Number of panels in the circumferential direction is 20. *NN*×*MM* on the blade is 60×20 and Δθ=6°. Wake length is 4.50.

4.3 VALIDATION OF CIRCUMFERENTIALLY AVERAGED ROTOR INDUCED VELOCITIES

In the induced velocity method, the circumferentially averaged induced tangential velocities $u_{tan,SR}$ are evaluated via the integral equation (3.8) by using the RPAN subroutine from Newman (1986). RPAN evaluates the induced velocities by a unit strength dipole or source panel. In order to validate this approach, $u_{tan,SR}$ calculated via Equation (3.8) are compared with those evaluated by using Stokes' theorem and those from the RANS simulation of the rotor only problem. According to Stokes' theorem, the circumferentially averaged tangential velocities, $u_{tan,SR}$ at any point in the rotor trailing wake can be calculated from the formula as following:

$$u_{\tan,SR} = \frac{N_b \Gamma_b}{2\pi R} \tag{4. 3}$$

where Γ_b is the strength of the vortex ring at a certain radius, and can be interpolated from the solution of the rotor problem. N_b is the total number of rotor blades. R is the radius to the axis of the rotor. Figure 4.18 shows a sketch of a rotor and its wake for the evaluation of tangential velocities by using Stokes' theorem and Figure 4.19 shows a ketch where tangential velocities are calculated behind the rotor wake in RANS. In these three approaches, the evaluation of tangential velocities is done by taking the average of the velocities at the points distributed evenly between two rotor blades and then interpolated to the control points on the stator blade.

The comparison of the circumferentially averaged $u_{tan,SR}$ by using Equation (3.8) and by using Stokes' theorem are shown in Figure 4.20. The induced swirl velocities by the rotor on the control points of the stator blade at several sections by these two methods are compared in Figure 4.21. The results by using these two methods agree well with each other. Figure 4.22 presents the comparison of the circumferentially averaged $u_{tan,SR}$ by using Equation (3.8) and by using RANS solver. The comparison of the

induced swirl velocities by the rotor on the control points of the stator blade at several sections by these two methods are shown in Figure 4.23. Some discrepancies occur at the place close to the stator tip but the rest results still have good agreements.

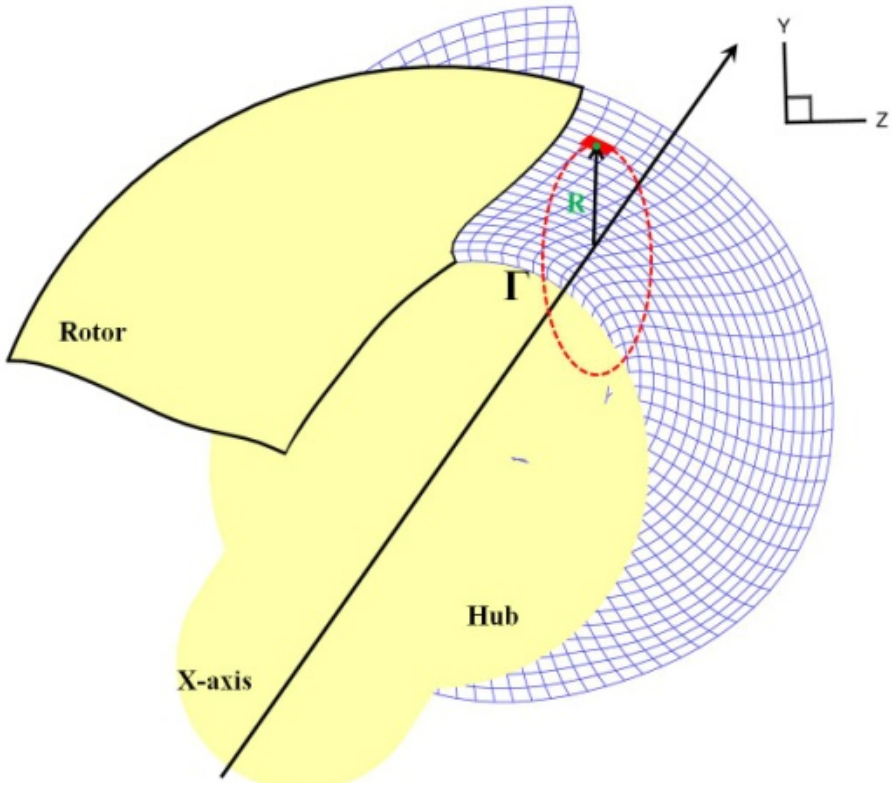

Figure 4.18: Sketch showing the rotor blade of the ONR AxWJ2 water-jet and its wake for the evaluation of circumferentially averaged tangential velocities by using Stokes' theorem at any point in the rotor wake sheet.

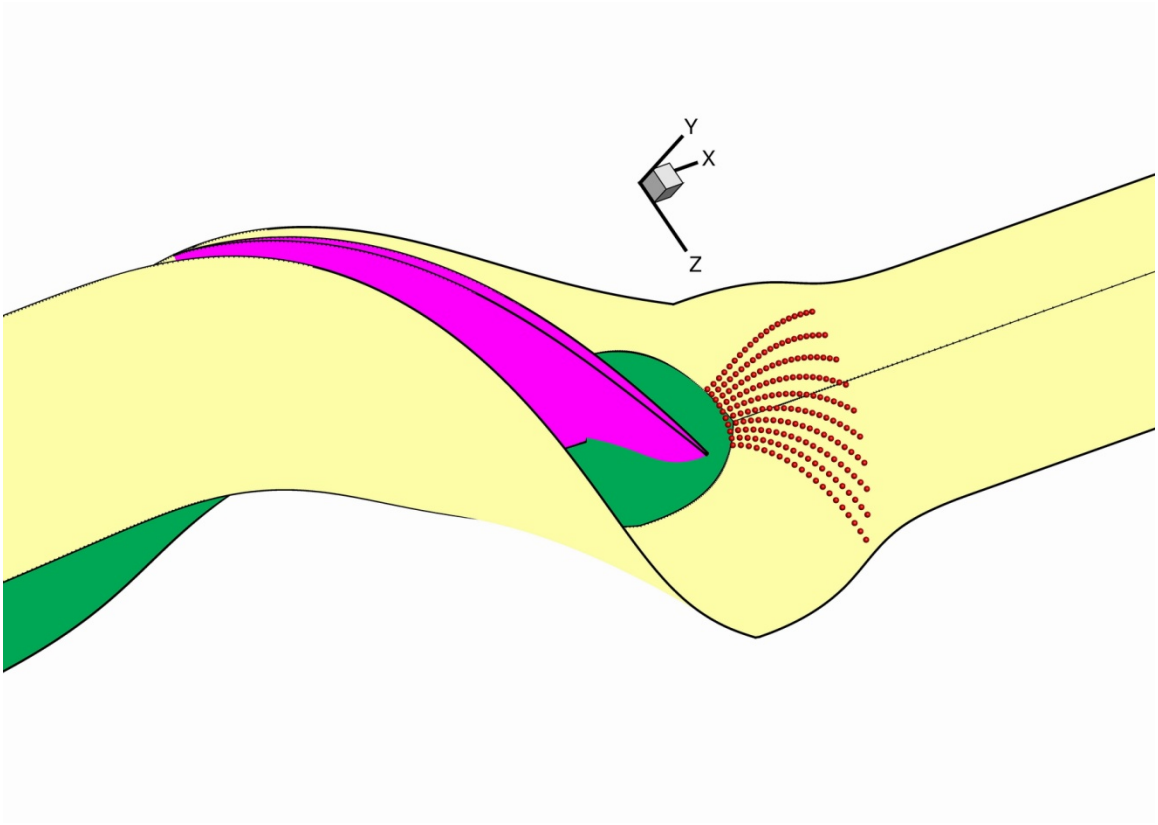

Figure 4.19: Sketch showing where the tangential velocities are calculated behind the rotor (pink) at the location of the stator. 10 evenly distributed points (red) are used for the evaluation of circumferentially averaged tangential velocities in FLUENT. The hub (green) and periodic boundaries (yellow) are also shown.

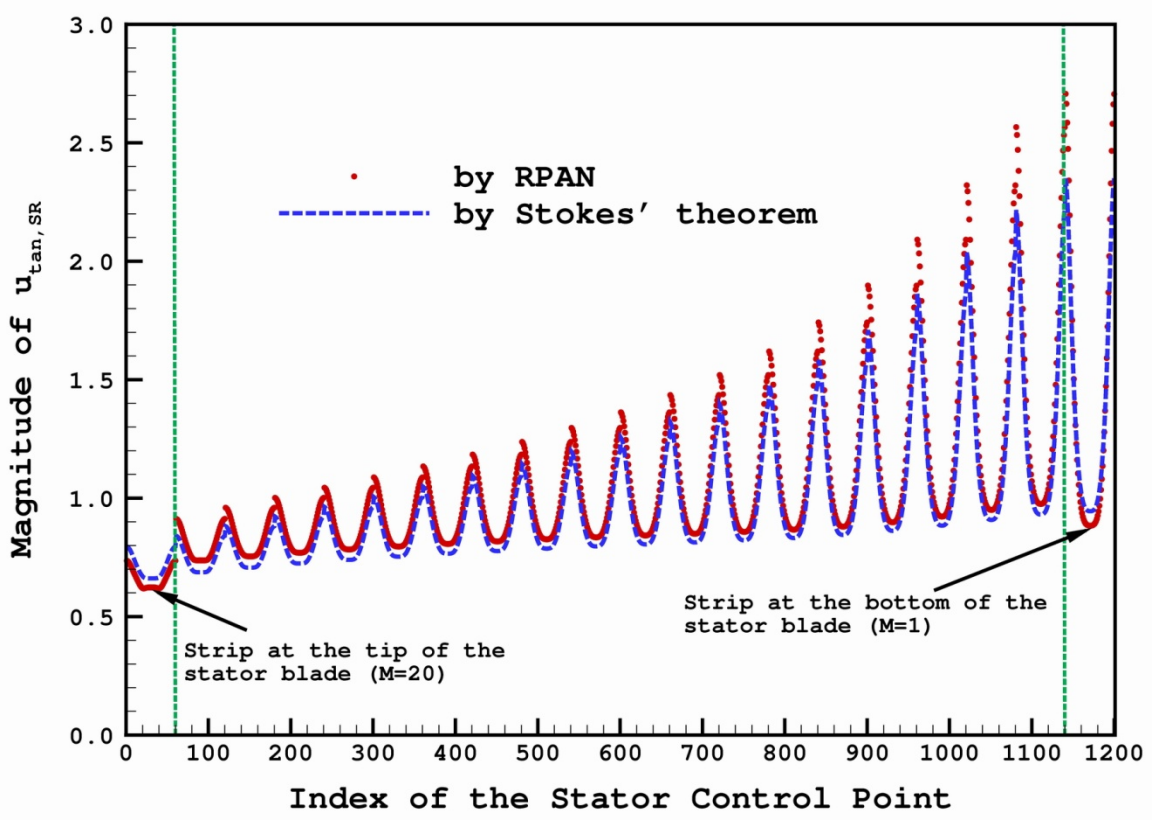

Figure 4.20: The circumferentially averaged $u_{tan,SR}$ on the stator by the rotor and its wake predicted by the present method via RPAN and via Stokes' theorem are compared.

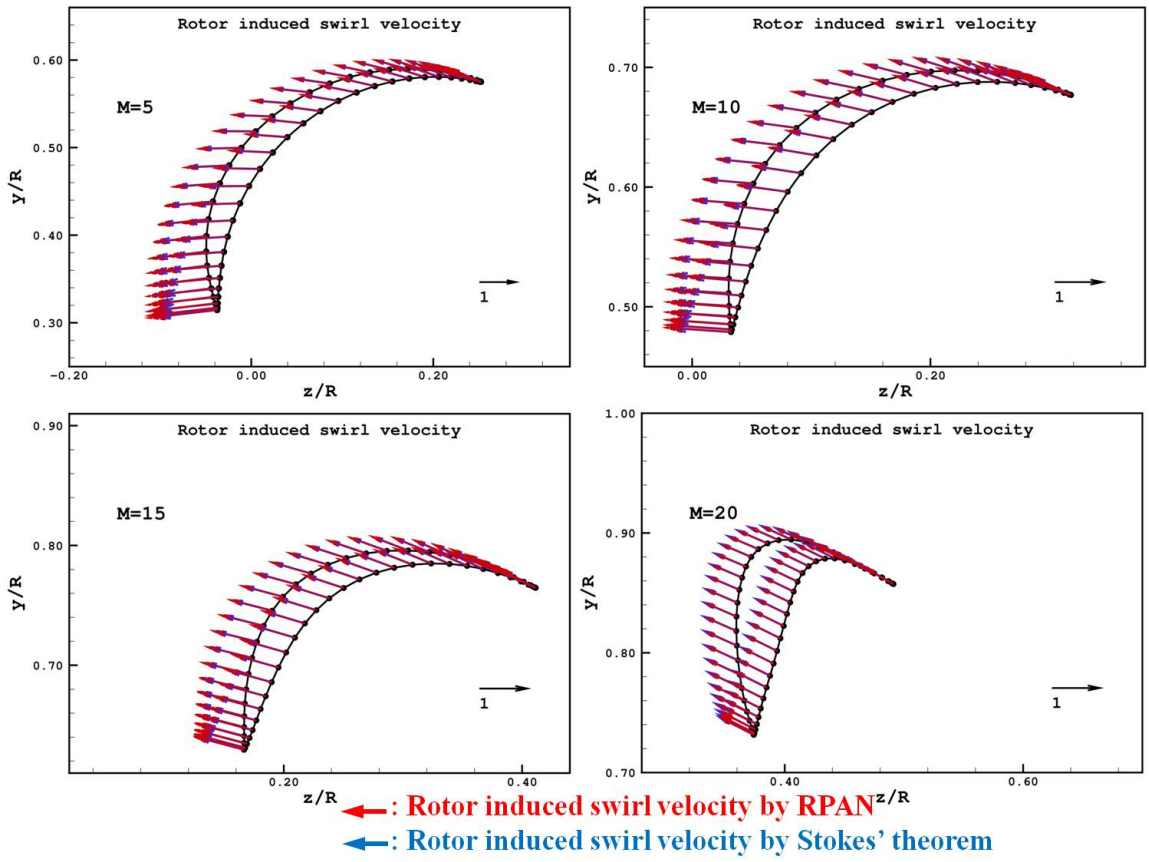

Figure 4.21: The comparison of the rotor induced swirl velocities on the stator blade predicted by the present method via RPAN and via Stokes' theorem.

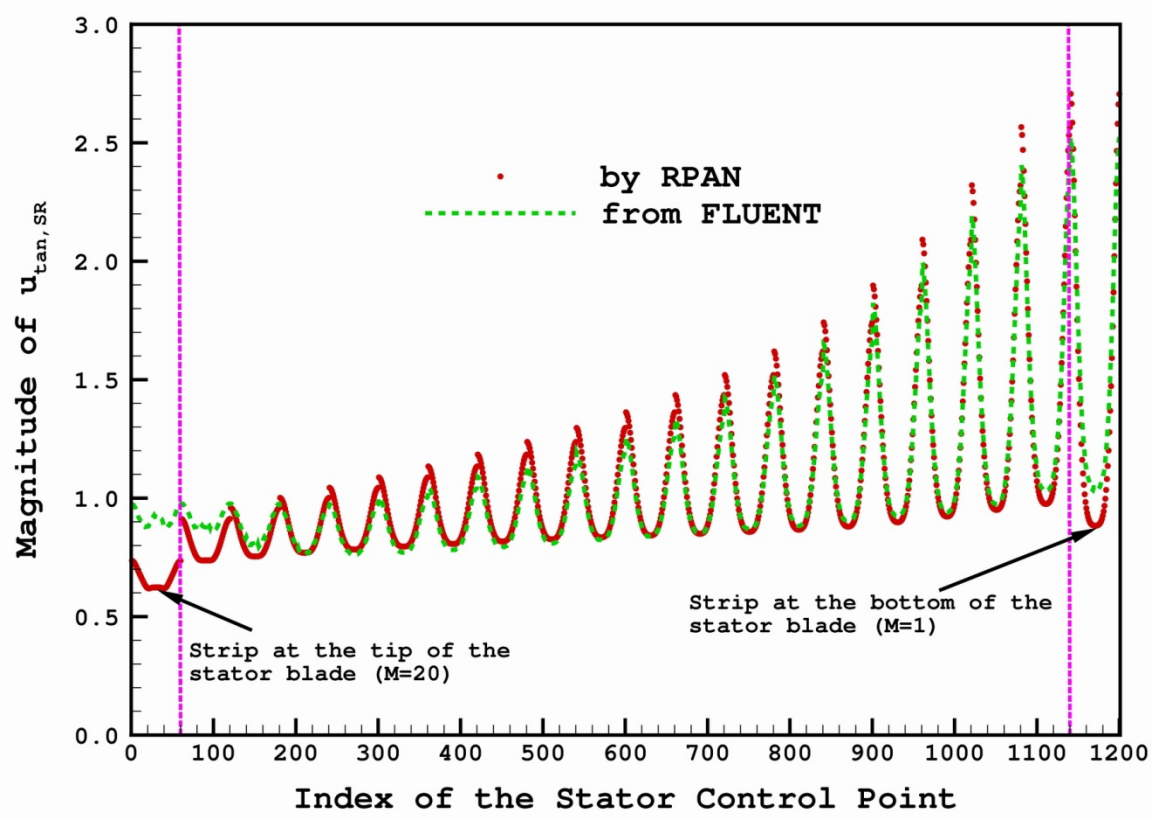

Figure 4.22: The circumferentially averaged $u_{tan,SR}$ on the stator by the rotor and its wake predicted by the present method via RPAN and via FLUENT are compared.

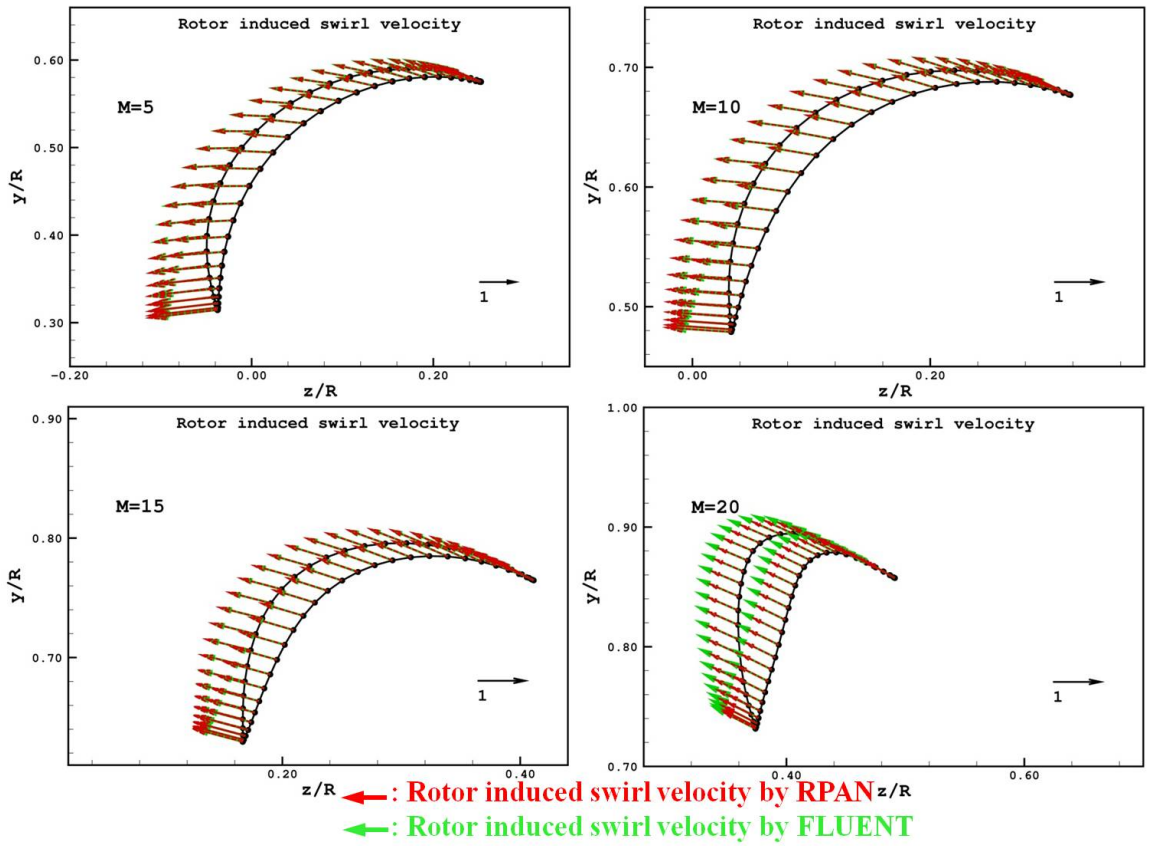

Figure 4.23: The comparison of the rotor induced swirl velocities on the stator blade predicted by the present method via RPAN and from FLUENT.

4.4 SUMMARY

The present numerical method has been validated in several different cases, the rotor only problem, the stator only problem and the rotor induced swirl velocities on the stator blade. The results predicted by the present approach show a fairly good convergence, consistency and agreement with either the results from the experimental observation or other numerical methods. In the next chapter, the present method will be applied to the prediction of the hydrodynamic performance of ONR AxWJ2 water-jet pump.

Chapter 5: Numerical Results of the ONR AxWJ2 Water-jet Pump

In this chapter, the present numerical scheme based on the potential flow theory is utilized to analyze the cavitating hydrodynamic performance including thrust breakdown of water-jet propulsion system. In order to include the viscosity effects over the casing and hub inside the pump, the present method is coupled with a RANS solver to evaluate the pressure rise on the casing surface for rotor only and rotor/stator interaction simulations. The interaction between the rotor and stator is carried out by applying induced velocity approach. The rotor or stator effect is represented by distributing body forces over the corresponding blade areas in a 2-D axisymmetric fluid domain in RANS solver. The numerical results, including the power coefficient (P^*), head coefficient (H^*), pump efficiency (η), thrust and torque coefficients (K_T and K_Q), as well as the cavity patterns are compared with the experimental data from a series of measurements on ONR AxWJ2 pump at NSWCCD (Naval Surface Warfare Center at Carderock Division). The experimental data are obtained from the report of Chesnakas et al. (2009), who also made calculations by using commercial RANS solvers (CFX and FLUENT). The geometry of the tested pump has an inlet diameter of 0.3048 m and an outlet diameter of 0.2134 m. The design pump has a 6-bladed rotor and an 8-bladed stator as shown in Figure 5.1. The paneled geometries used for the numerical calculation of the present method are shown in Figure 5.2 and 5.3 for the rotor problem and stator problem, respectively. The design advance ratio J_S is 1.19 and the rotational frequency is 2000 *rpm* for the cavitating condition and 1400 *rpm* for the non-cavitating condition.

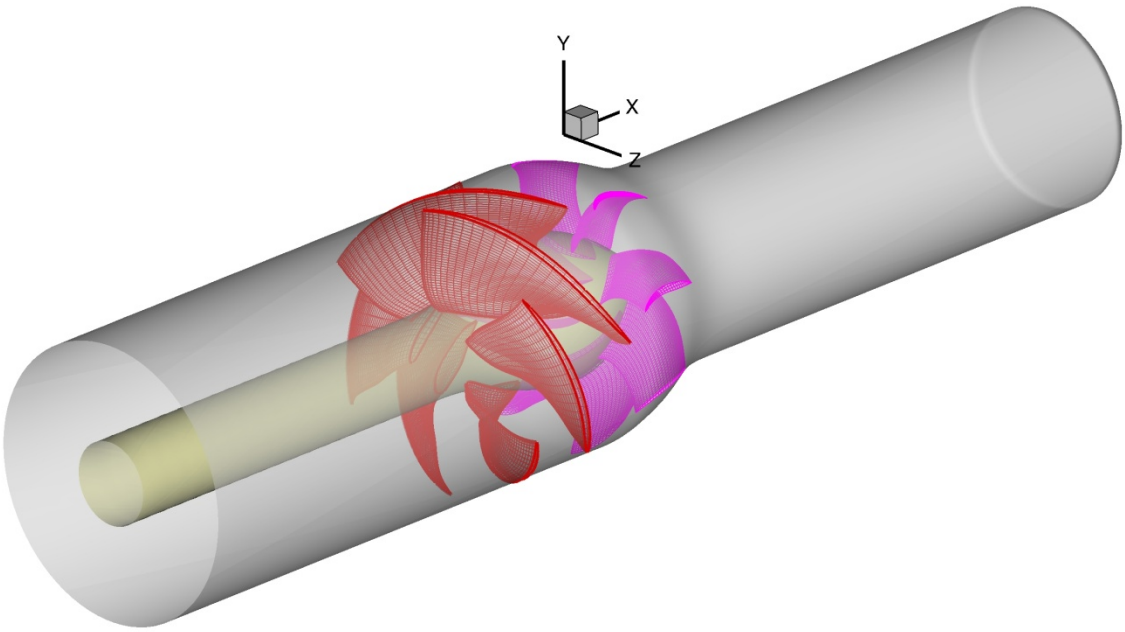

Figure 5.1: Paneled geometry of the ONR-AxWJ2 water-jet pump with a 6-bladed rotor and an 8-bladed stator viewed from upstream. *NN*×*MM* on the rotor and stator blades is 60×20.

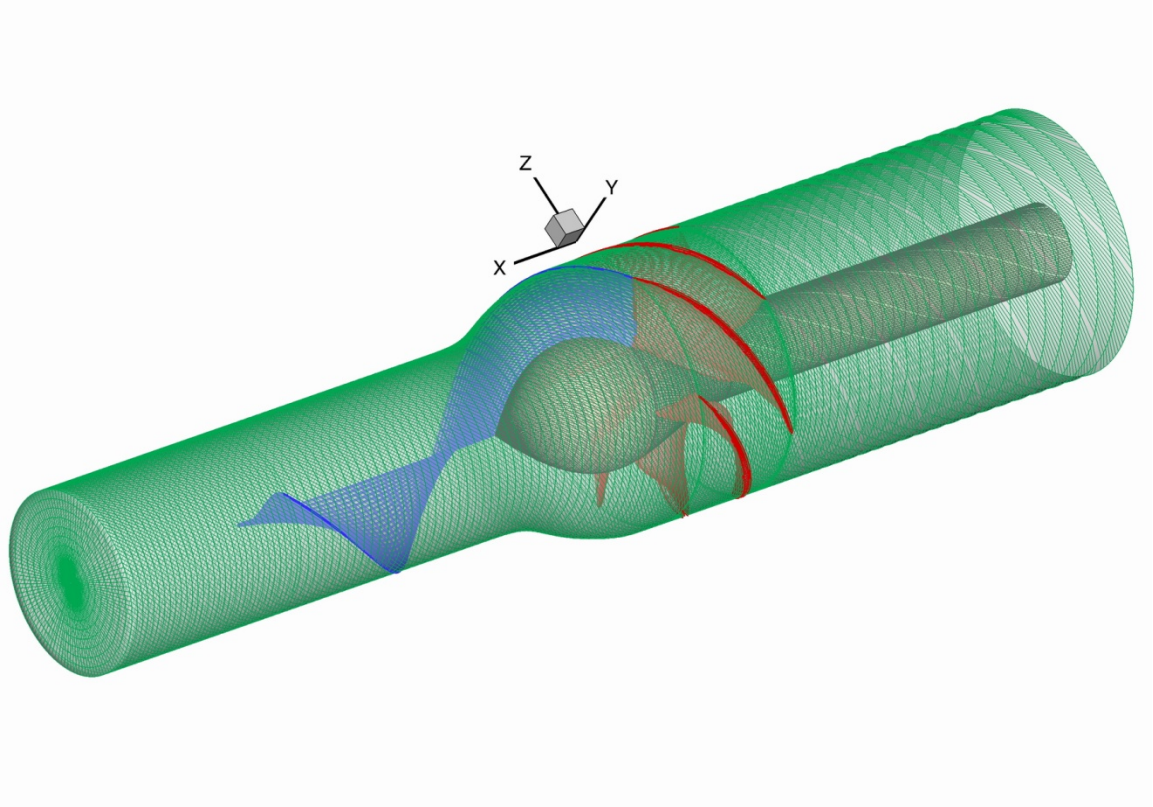

Figure 5.2: Paneled geometry of the ONR AxWJ2 water-jet pump for the rotor problem (the key blade trailing wake is shown), viewed from down-stream. Number of panels in the circumferential direction is 20. *NN*×*MM* on the rotor blade is 60×20 and wake length is 4.50. $\Delta\theta=6°$.

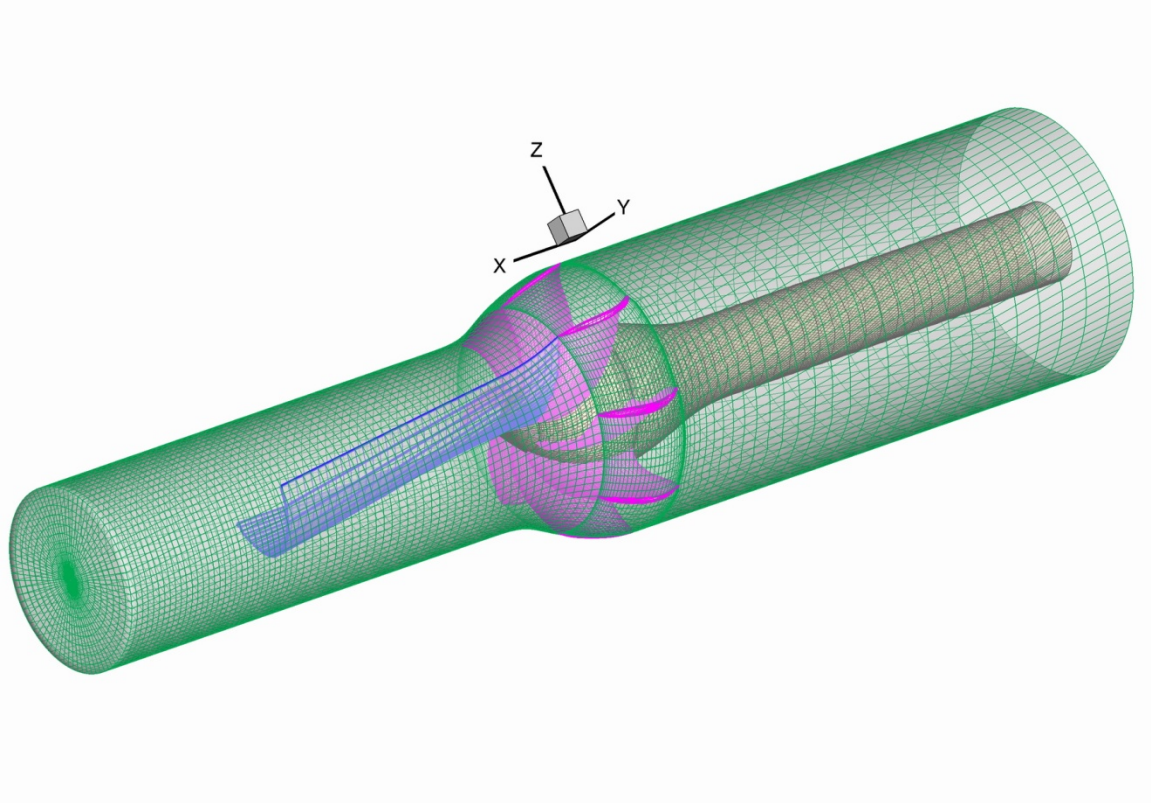

Figure 5.3: Paneled geometry of the ONR AxWJ2 water-jet pump for the stator problem (the key blade trailing wake is shown), viewed from down-stream. Number of panels in the circumferential direction is 20. *NN*×*MM* on the stator blade is 60×20 and wake length is 4.50. $\Delta\theta=6°$.

5.1 FORCES AND PARAMETERS

In this section, the definition of the non-dimensionalized coefficients used in this dissertation is addressed.

The thrust coefficient K_T and the torque coefficient K_Q are defined as:

$$K_T = \frac{F}{\rho n^2 D^4},\ K_Q = \frac{Q}{\rho n^2 D^5} \tag{5.1}$$

The head coefficient H^* and the power coefficient P^* are defined as:

$$H^* = \frac{P_{t6} - P_{t3}}{\rho n^2 D^2},\ \mathrm{P}^* = \frac{2\pi nQ}{\rho n^3 D^5} = 2\pi K_Q \tag{5.2}$$

The flow coefficient Q^* and the pump efficiency η can be expressed as:

$$Q^* = \frac{Q_J}{nD^3},\ \eta = \frac{Q^* H^*}{P^*} \tag{5.3}$$

where ρ denotes water density, n represents the propeller revolution per second (*rps*), D is the diameter of the propeller, F and Q are the thrust and the torque calculated from the present method. P_{t3} is the measured pressure at station 3 close to the upstream, and P_{t6} is the measured pressure at station 6 which is downstream close to the nozzle exit in the pump as shown in Figure 5.4. Q_J is volumetric flow rate.

The advance ratio J_S and the Reynolds number Re are also given as:

$$J_S = \frac{V_{in}}{nD},\ \mathrm{Re} = \frac{V_{in} D}{\nu} \tag{5.4}$$

where V_{in} is the flow velocity at the inlet boundary, D represents the diameter of the rotor, and ν denotes the kinematic viscosity.

The pressure coefficient C_P and cavitation number σ_n used in the present method are defined as follows:

$$C_P = \frac{P - P_0}{0.5\rho n^2 D^2},\ \sigma_n = \frac{P_o - P_v}{0.5\rho n^2 D^2} \tag{5.5}$$

where P_0 is the far upstream pressure on the shaft axis, and P_v is the vapor pressure.

The cavitation coefficient N^* in the experiment is defined as:

$$N^* = \frac{P_{t3} - P_v}{\rho n^2 D^2} = \frac{(P_3 + \frac{1}{2}\rho V_3^2) - P_v}{\rho n^2 D^2} = \frac{P_3 - P_v}{\rho n^2 D^2} + \frac{1}{2}\frac{V_3^2}{n^2 D^2} = \frac{1}{2}\sigma_n + \frac{1}{2}J_S^2 \tag{5.6}$$

We assume the station 3 is far upstream, thus, the pressure P_3 equals to P_0 and velocity V_3 equals to V_{in}.

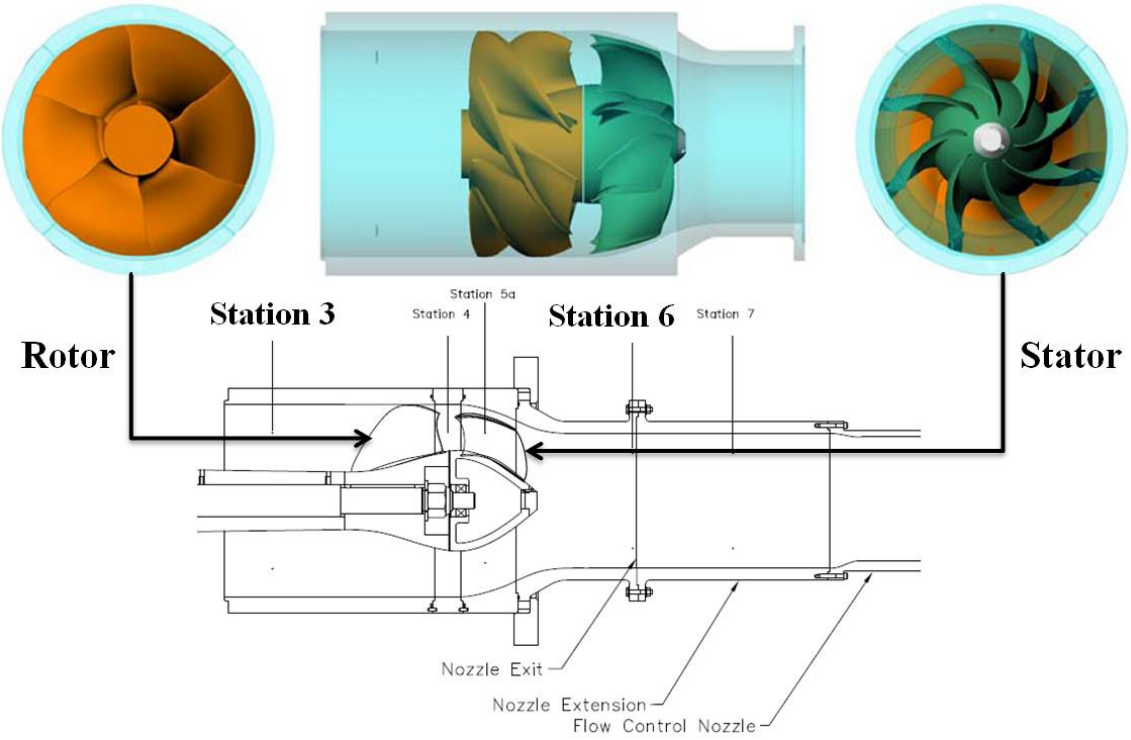

Figure 5.4: ONR AxWJ2 pump with nozzle extension and flow control nozzle (from Chesnakas et al. 2009).

5.2 ROTOR ONLY CALCULATIONS

In this section, the numerical simulation is performed without the present of the stator.

Fully-wetted Solution

The fully-wetted results including the pressure distributions on the rotor sections, power coefficient (P^*) and the pressure rise on the casing surface are compared with those from the experiments and FLUENT.

The potential solver of the present method takes 2 minutes for a fully-wetted analysis and 6 minutes for a cavitating calculation by using 60×20 panels on the blade, 90×20 panels on the hub and 190×20 panels on the casing.

A 2-D axisymmetric domain is used for the potential solver coupling with FLUENT as shown in Figure 5.5. The body forces of the rotor are distributed in the 2-D projected blade area while the stator region remains the fluid domain with no body force distributions. A mesh consisting of 12,000 cells takes about 2 minutes for less than 1,000 iterations by 1 CPU on a cluster with 2.43 GHZ quad-core 64-bit Intel Xeon processors and 16 GB of RAM. A 3-D rotor only periodic mesh consisting of 3.07 million cells as shown in Figure 5.6 is also used to analyze the rotor only simulation. The calculation takes about 28 hours by using 32 CPUs to finish the calculation of 20,000 iterations on the same cluster.

The geometries used in the present method and the 3-D FLUENT have some discrepancies at the blade trailing edge as shown in Figure 5.7. Figure 5.8 shows the pressure contours on the rotor blade from two methods. The pressure distributions at different constant radius are compared in Figure 5.9. The major differences of the pressures are near the blade trailing edge, and the main reason is caused by the different thickness used for two analyses. The pressures close to the trailing edge of the blade can

be improved by coupling the present method with a boundary layer solver (XFOIL) as shown in Figure 5.10.

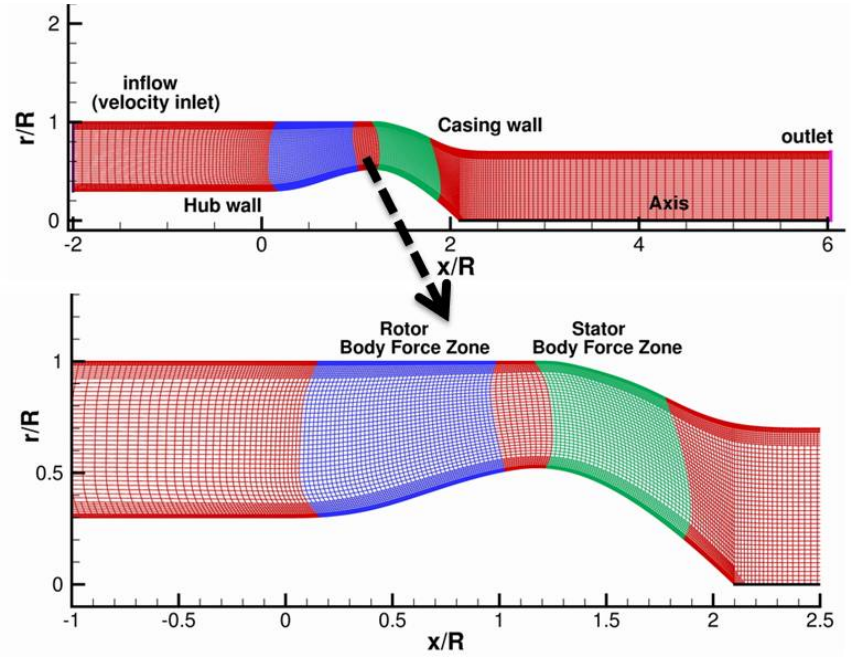

Figure 5.5: 2-D axisymmetric computational domain, meshes and boundaries of the ONR AxWJ2 water-jet.

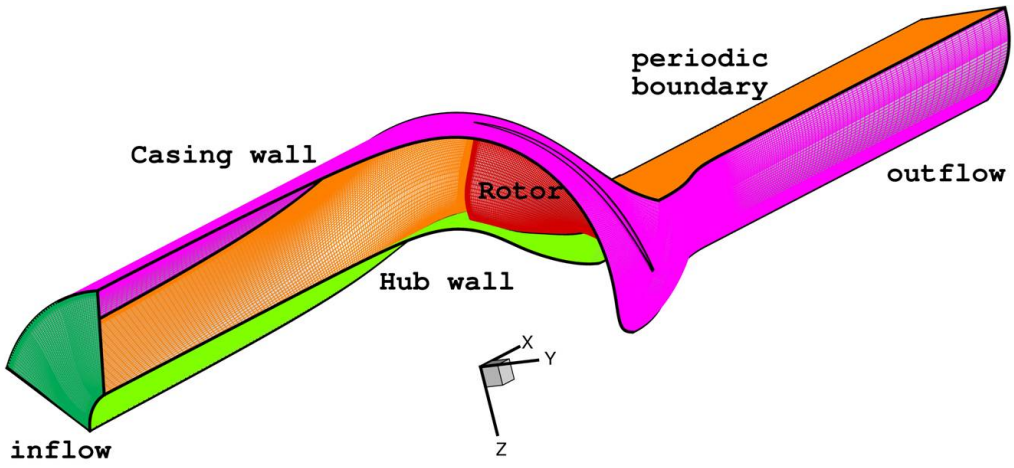

Figure 5.6: 3-D periodic computational domain, meshes and boundaries of the ONR AxWJ2 water-jet.

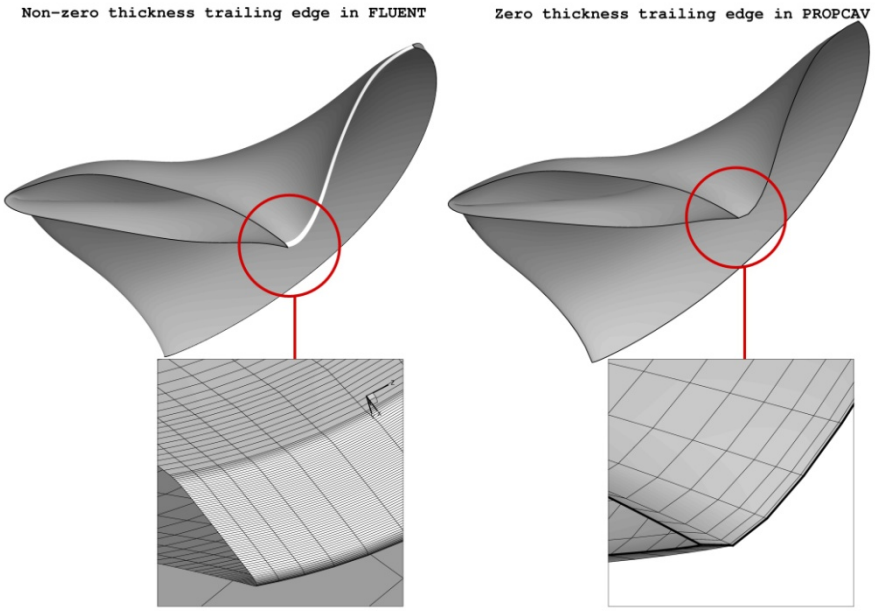

Figure 5.7: Comparison of the ONR AxWJ2 rotor blade geometry. The trailing edge of the geometry used in FLUENT (left) is blunt and has non-zero thickness and that in PROPCAV-WJ (right) is sharp and has zero thickness.

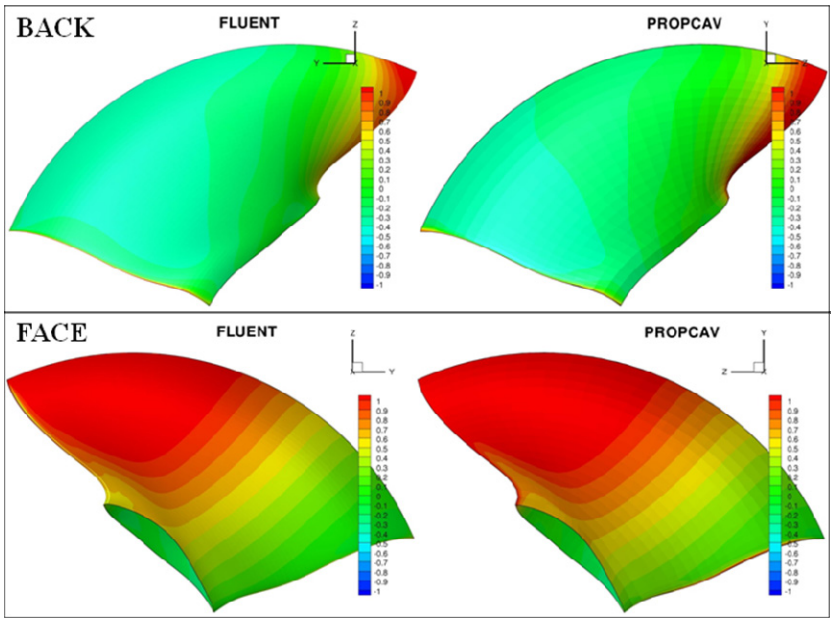

Figure 5.8: Comparison of $-C_P$ (fully-wetted condition) on the rotor blade of the ONR AxWJ2 water-jet at J_S=1.19.

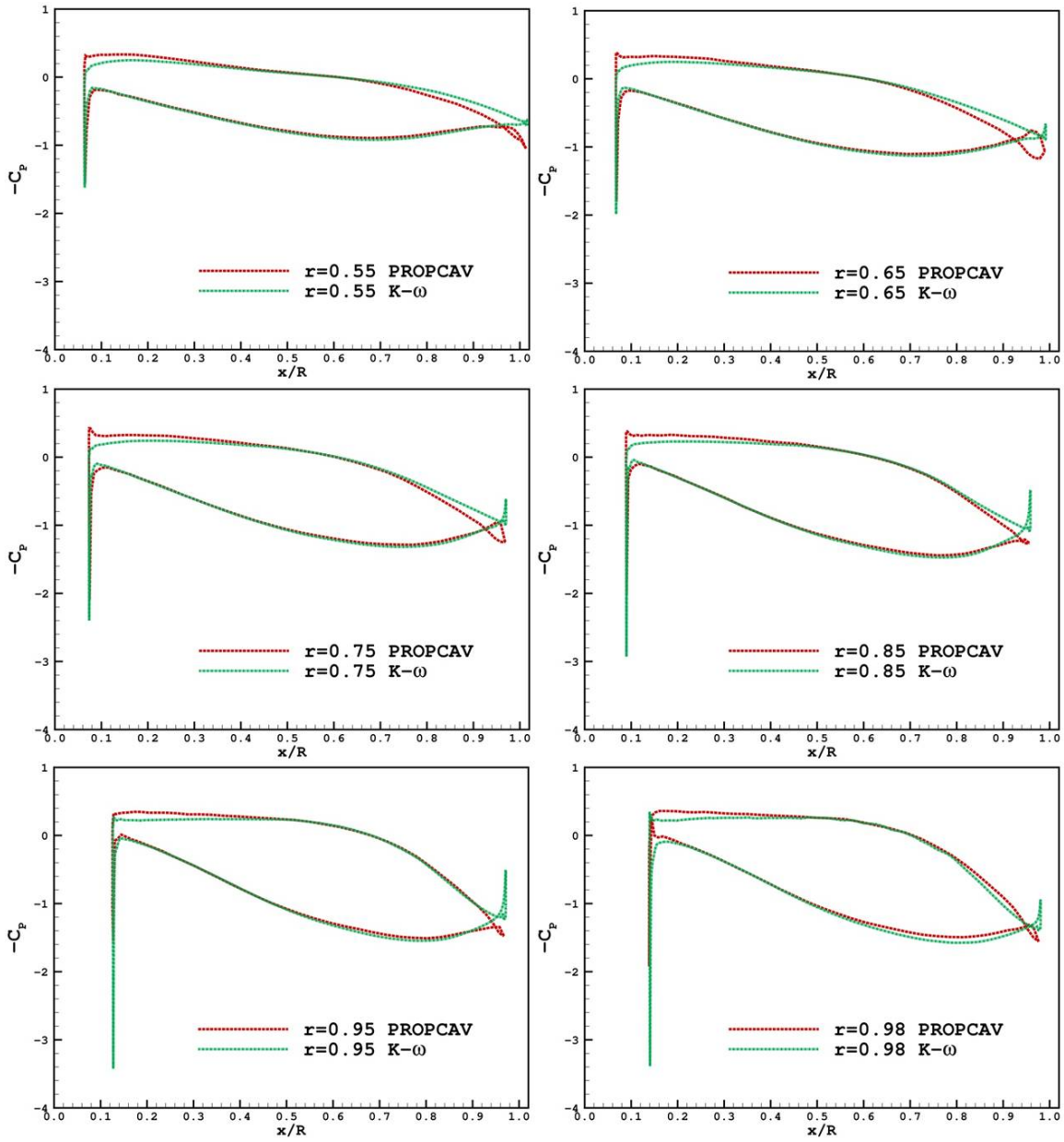

Figure 5.9: Comparison of pressure distributions (fully-wetted condition) by using C_f =0.004 and viscous pitch correction at different constant radius of the rotor blade the ONR AxWJ2 water-jet at J_S=1.19.

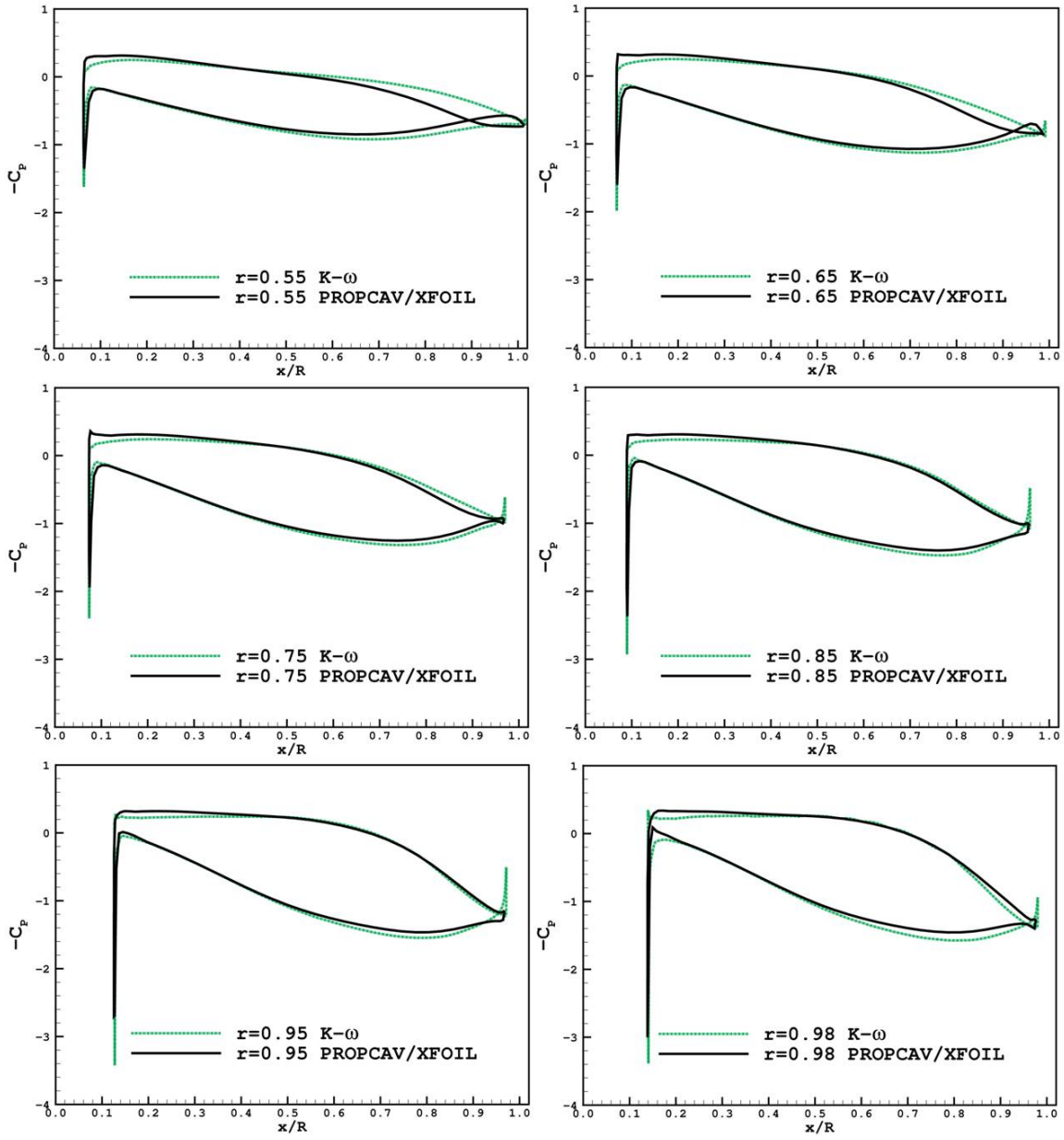

Figure 5.10: Comparison of pressure distributions (fully-wetted condition) by coupling with XFOIL (Re=2.26×10^6, fixed transition point at 0.05 chord length of each section and 1% turbulence level) at different constant radius of the rotor blade the ONR AxWJ2 water-jet at J_S=1.19.

The comparison of the experimental and predicted, either by using C_f=0.004 and viscous pitch correction or by coupling with XFOIL, power coefficient (P^*) of the ONR AxWJ2 water-jet pump for different flow rate (Q^*) are shown in Figures 5.11 and 5.12, respectively. The results from the present method are by using viscous pitch correction and empirical friction coefficient from Equation (3.27) (Re=2.26×10^6, thus $C_f=0.004$), which seem to agree well with the experimental data and the largest error is about 1.5% at Q^*=0.93. Table 5.1 shows the data from the experiment and predicted results from the present by using viscous pitch correction and empirical friction coefficient. Table 5.2 shows the data from the experiment and predicted results from the present method by coupling with the boundary layer solver XFOIL (Re=2.26×10^6, fixed transition point at 0.05 chord length of each section and 1% turbulence level).

Q^*	Experiment	PROPCAV-WJ	|Error| (%)
0.72	2.106	2.096	0.47
0.75	2.105	2.089	0.76
0.80	2.104	2.084	0.95
0.85	2.090	2.079	0.53
0.90	2.069	2.042	1.30
0.93	2.035	2.004	1.52

Table 5.1: Experimental and predicted (by using C_f=0.004) power coefficients (P^*) of the ONR AxWJ2 water-jet pump at different flow coefficients (Q^*).

Q^*	Experiment	PROPCAV-WJ	|Error| (%)
0.72	2.106	2.089	0.81
0.75	2.105	2.078	1.28
0.80	2.104	2.070	1.62
0.85	2.090	2.065	1.20
0.90	2.069	2.056	0.63
0.93	2.035	2.020	0.74

Table 5.2: Experimental and predicted (by coupling with *XFOIL*) power coefficients (P^*) of the ONR AxWJ2 water-jet pump at different flow coefficients (Q^*).

The pressure rise on the casing for the rotor only case is investigated. The prediction of the pressure distributions obtained from the hybrid scheme is compared with those from 3-D FLUENT simulation. Figure 5.13 shows the body force distributions in 2-D axisymmetric calculation. The comparison of pressure distributions on the casing surface is shown in Figure 5.14. The two C_P curves are the results of circumferentially averaged pressures of all stripes on the casing surface from 3-D FLUENT simulation and those from 2-D axisymmetric inviscid/viscous coupling.

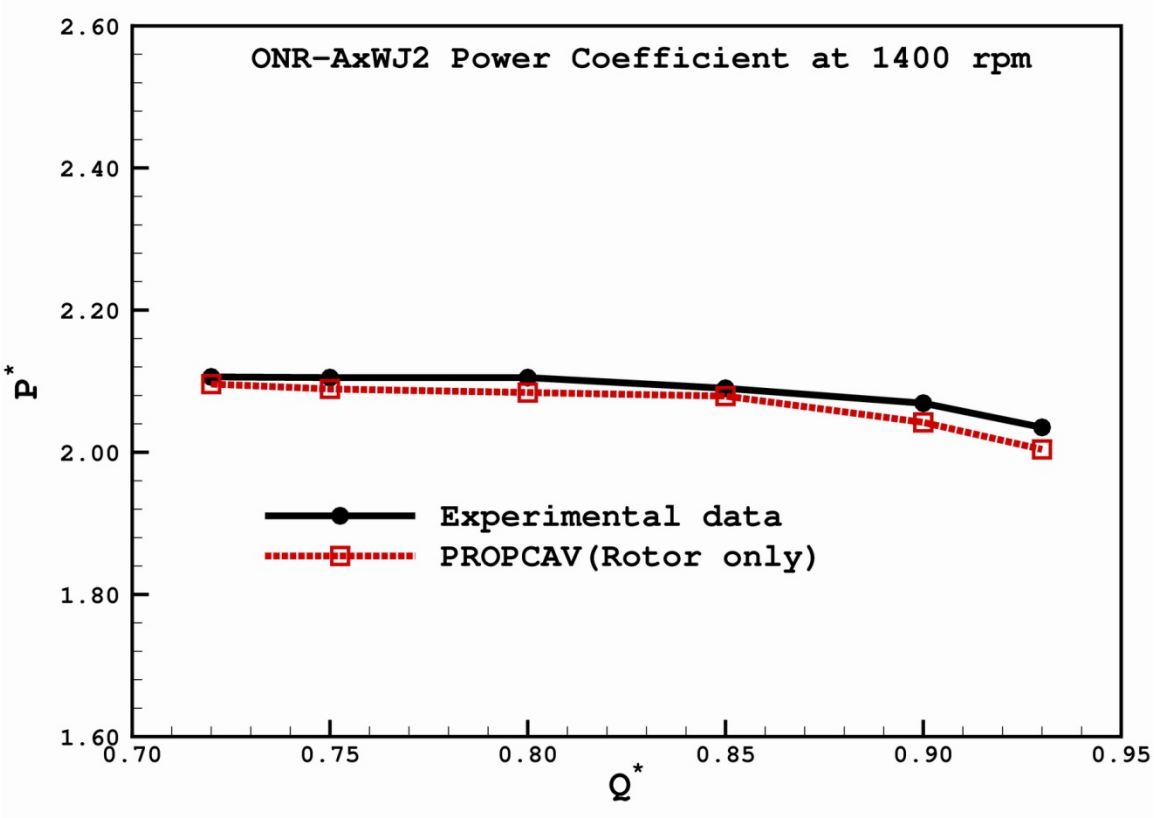

Figure 5.11: Comparison of the predicted (by using C_f=0.004) power coefficients of the ONR AxWJ2 water-jet with the experimental data from Chesnakas et al. (2009).

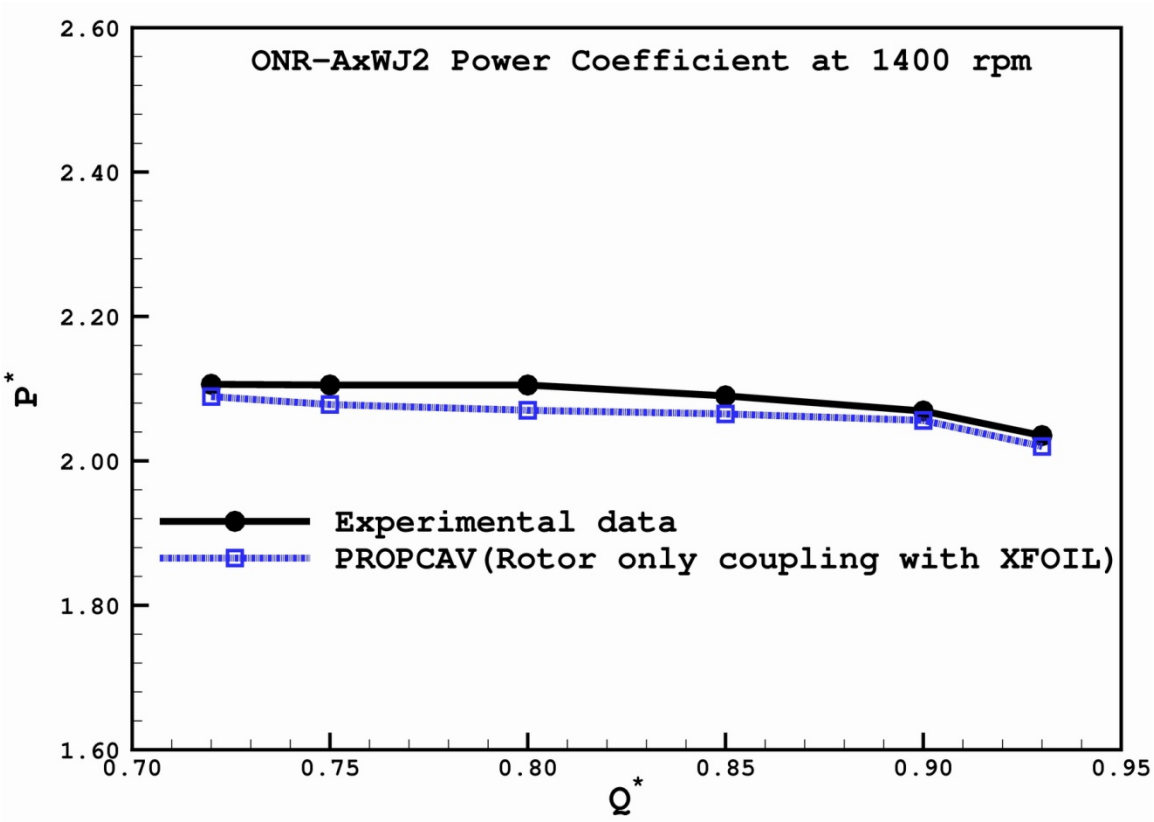

Figure 5.12: Comparison of the predicted (by coupling with XFOIL, Re=2.26×10^6, fixed transition point at 0.05 chord length of each section and 1% turbulence level) power coefficients of the ONR AxWJ2 water-jet with the experimental data from Chesnakas et al. (2009).

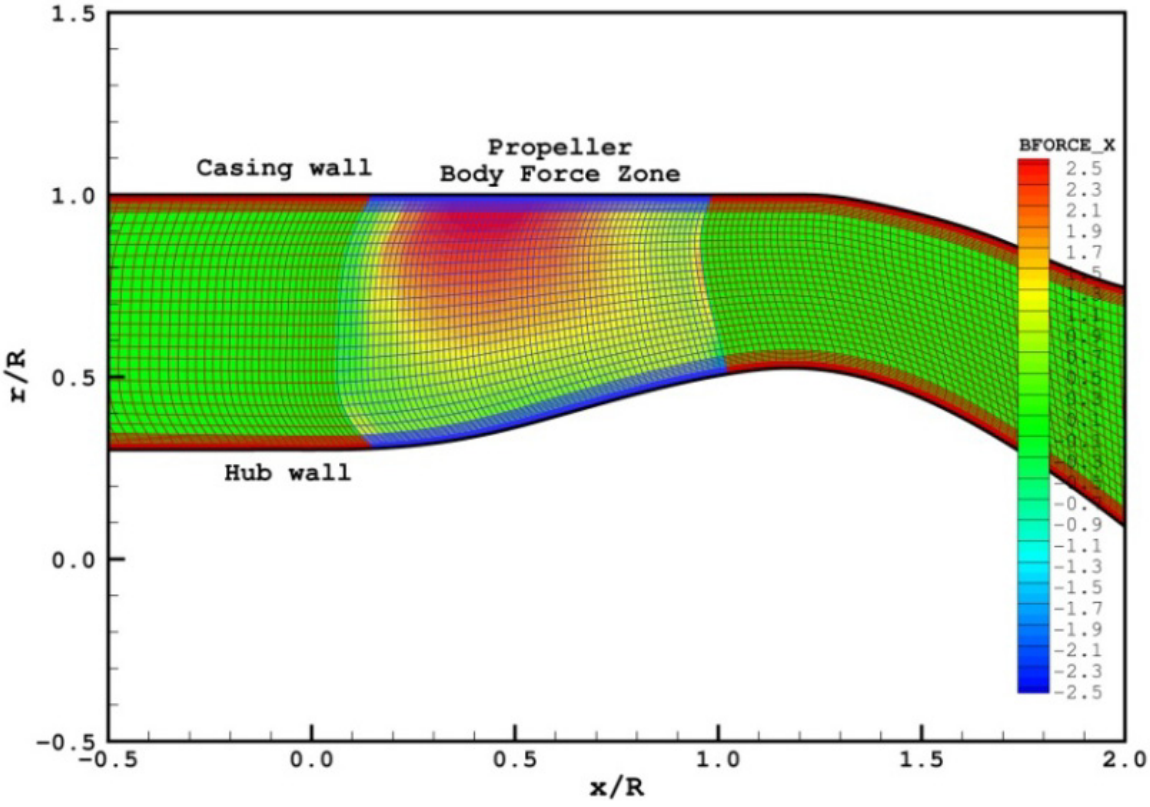

Figure 5.13: Body force distributions of the ONR AxWJ2 water-jet at J_S=1.19 in 2-D axisymmetric FLUENT (rotor only). Re=2.26×10^6.

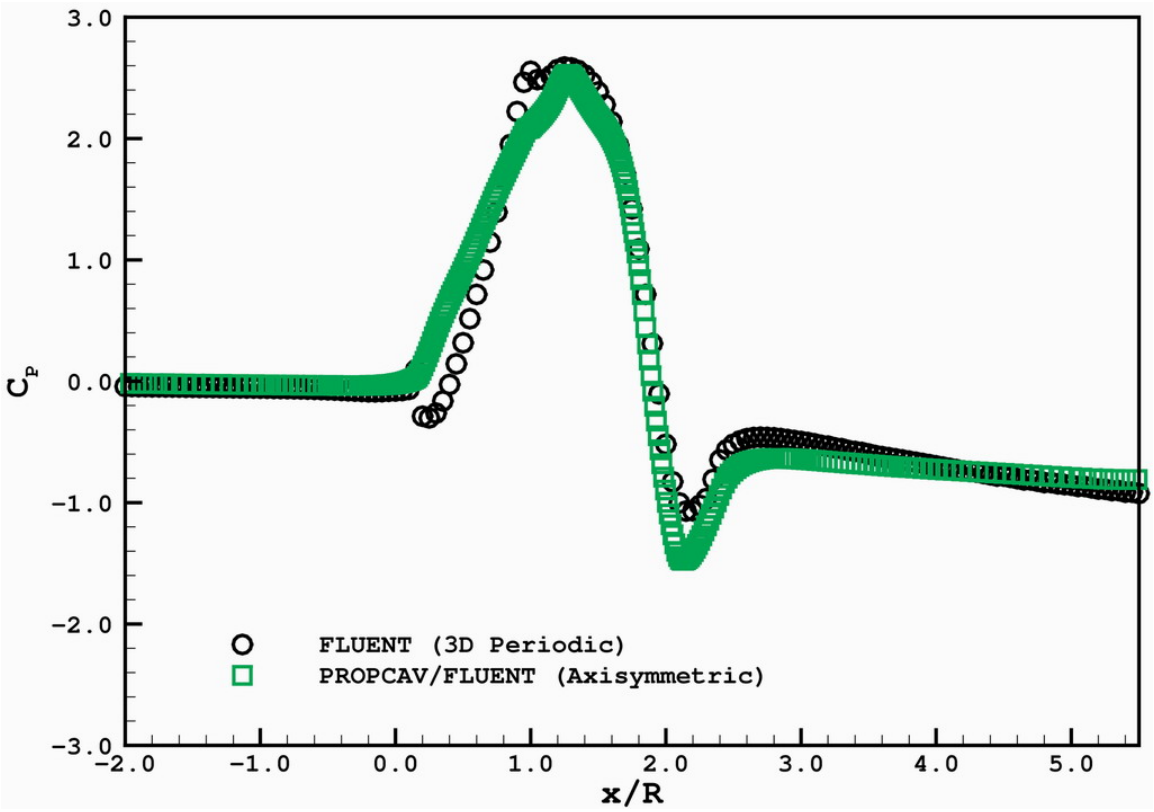

Figure 5.14: Comparison of C_P*on the casing surface for the rotor only case at J_S=*1.19* (Q^*=*0.85*). Re=2.26×10^6.

* The source terms due to the rotor blade thickness (Kinnas et al. 2009) are not included in the continuity equation in RANS, and that may improve the correlation of pressures on the casing surface.

Cavitating Solution

The J_S and cavity number σ_n used in the present method for the cavitating calculation correspond to the flow coefficient (Q^*) and cavitation coefficient (N^*) in the experiments.

The comparisons of cavitation coverage on the rotor blade are shown in Figure 5.15 together with those from the experimental observations and those predicted by *CFX*. The prediction of the cavity patterns seems to agree well with those from the experiments. At highest cavitation coefficient condition ($N^*=4.044$), the present method is able to predict small sheet cavities starting from the leading edge of the blade while RANS solver shows no cavities. For lower cavitation coefficients, the present method tends to predict slightly larger extent of cavity patterns with than those from the experiments.

5.3 ROTOR AND STATOR INTERACTION

In this section, the numerical simulation is performed with the effects of one component to the other. Results from the present method are compared with experimental measurements and FLUENT rotor/stator simulation.

The rotor and stator interactions are carried out via using induced velocity method in an iterative procedure until the forces of the two components are converged. The convergence history of fully-wetted circulation distributions on the rotor and stator versus number of iterations (between the rotor and stator) at design $J_S=1.19$ is shown in Figure 5.16 and Figure 5.17 respectively. The results of the 0^{th} iteration in the figures are the rotor only or the stator only solutions without including the effect of the other. The circulation distributions verify that, as expected, the rotor significantly changes the

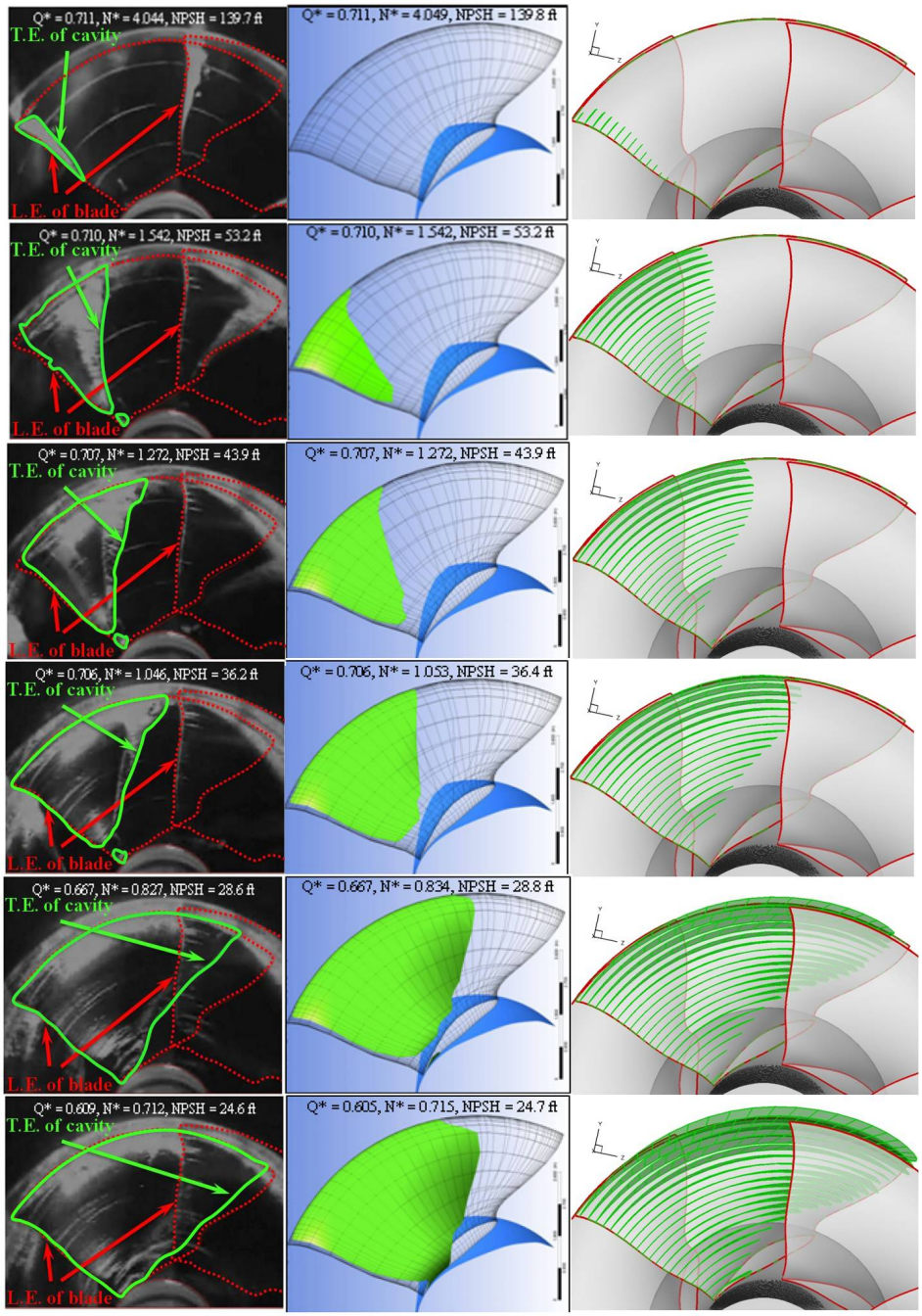

Figure 5.15: Comparison of the rotor cavitation coverage of the ONR AxWJ2 water-jet from Chesnakas et al. (2009)'s experimental observation (left), numerical calculation by CFX (middle) and the present method (right); in the left pictures, the red arrows point to the leading edge of two adjacent rotor blades and the green arrow points to the trailing edge of the cavities and green curve areas denote cavitation coverage of the observations.

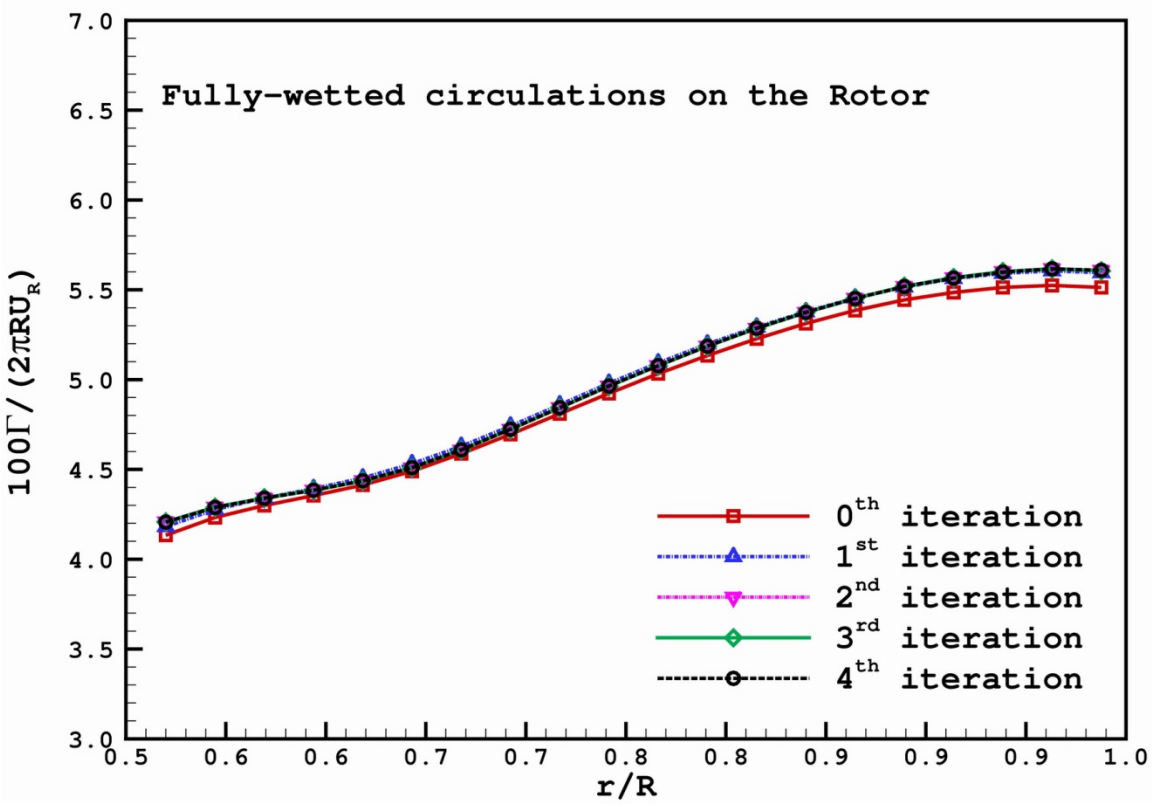

Figure 5.16: Convergence history of fully-wetted circulation distributions on the rotor of the ONR AxWJ2 water-jet pump at J_S=*1.19* (The 0th iteration corresponds to the rotor only solution).

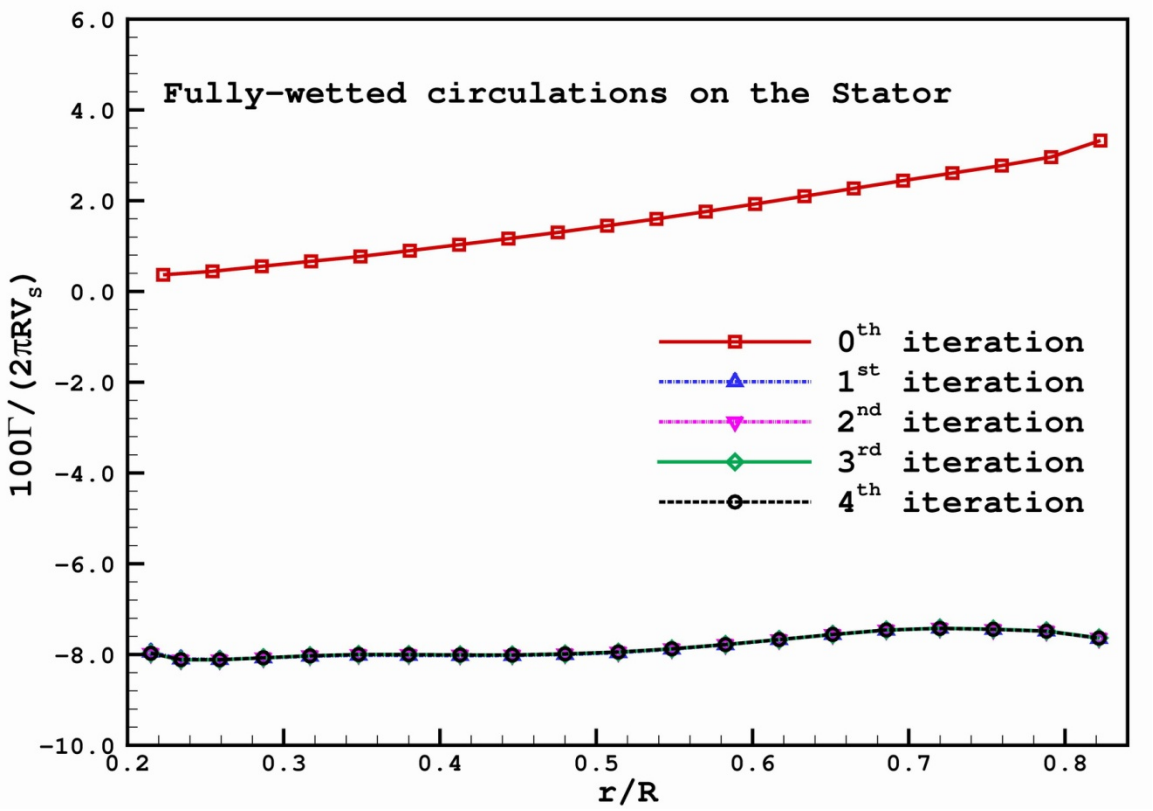

Figure 5.17: Convergence history of fully-wetted circulation distributions on the stator of the ONR AxWJ2 water-jet pump at J_S=*1.19* (The 0th iteration corresponds to the stator only solution).

loading on the stator, and that the stator affects the loading on the rotor by a small amount. The total computational time for *5* iterations between the two components is about 2 and half hours by using a single CPU with 2.43 GHz quad-core Intel Xeon processor and 16 GB of RAM. It should be noted that the major part of the CPU time is devoted on evaluating the velocities induced by each component on the other.

The predicted total thrust and torque coefficients on the rotor and stator from 1st to 4th iterations are shown in Figure 5.18 and Figure 5.19. The iterative process reaches to convergence within two iterations in the case. The total K_T and K_Q of the rotor after the interaction are 1.158 and 3.320 and increase about 1.58% and 0.33% higher than rotor only prediction as shown in Table 5.3. The total K_T and K_Q of the stator after the interaction are 0.212 and -3.342. One should notice that the torque coefficient of the two components has almost the same magnitude but different sign since the stator is designed to cancel the swirls shedding from the rotor blades. The predicted results of including the influence of the stator to the rotor are compared with the experimental data and those from FLUENT simulations. Figure 5.20 and Figure 5.21 show the predicted thrust and power coefficients on the rotor with and without the stator effect by the present method. The stator effect makes the total K_T and P^* of the rotor increase in a range of 1.0%~2.0% and 0.2%~0.8% respectively.

J_S=*1.19*	Rotor only	Rotor/Stator	Δ(*%*)
K_T	1.140	1.158	1.58
$10K_Q$	3.309	3.320	0.33

Table 5.3: Comparison of predicted K_T and K_Q by the present method between rotor only calculation and rotor/stator interaction of the ONR AxWJ2 water-jet at J_S=1.19.

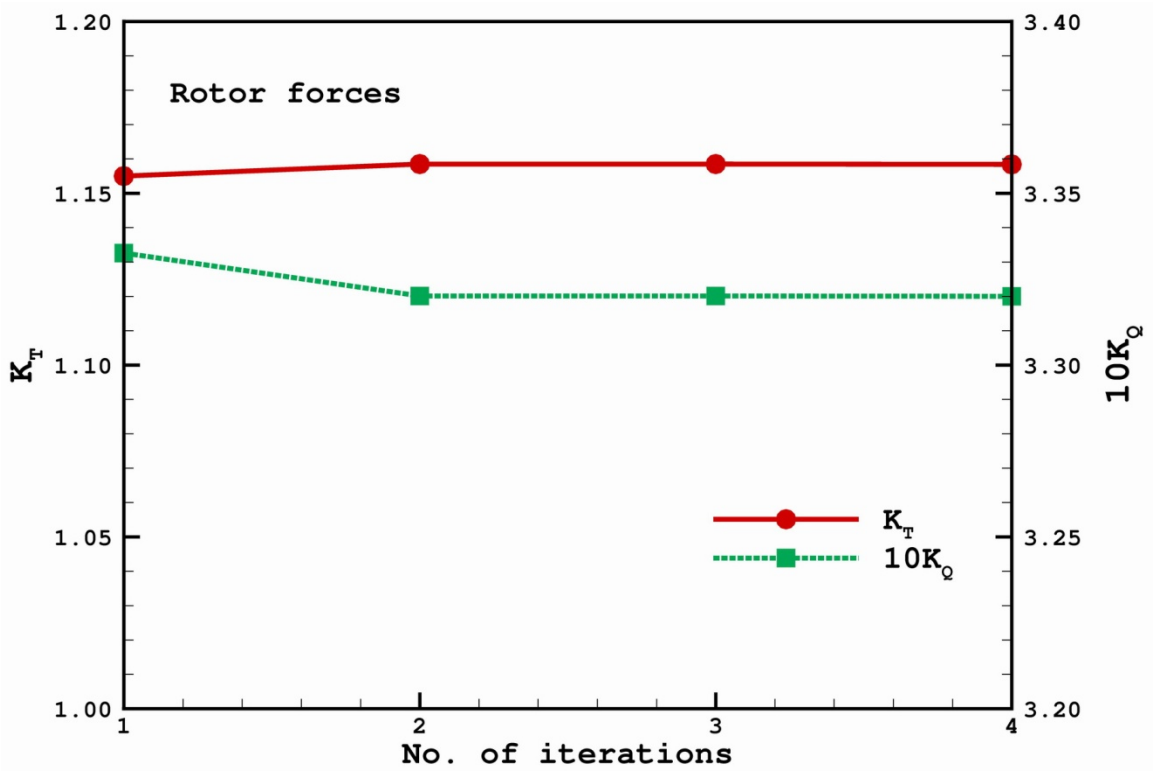

Figure 5.18: Convergence history of the rotor total K_T and K_Q of the ONR AxWJ2 water-jet with number of iterations during the interaction at J_S=*1.19* (Q^*=*0.85*). C_f=0.004 and viscous pitch correction.

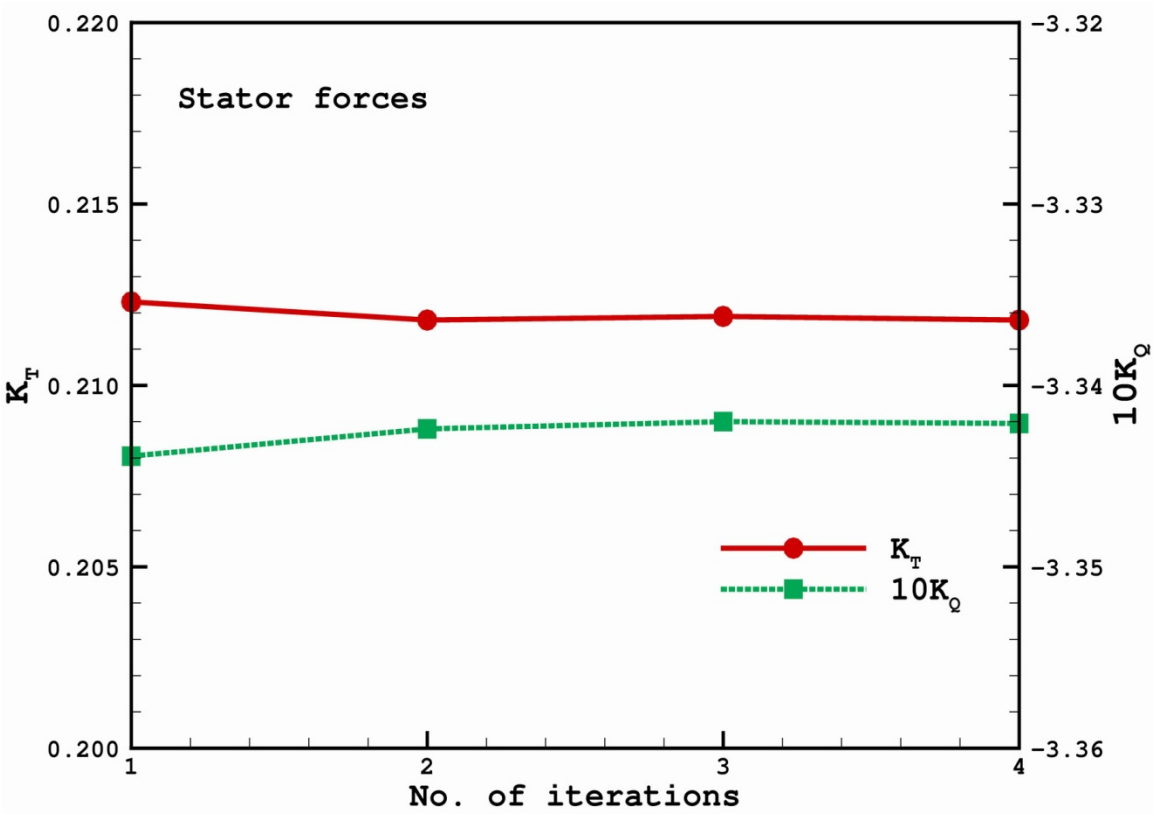

Figure 5.19: Convergence history of the stator total K_T and K_Q of the ONR AxWJ2 water-jet with number of iterations during the interaction at J_S=*1.19* (Q^*=*0.85*). C_f=0.004 and viscous pitch correction.

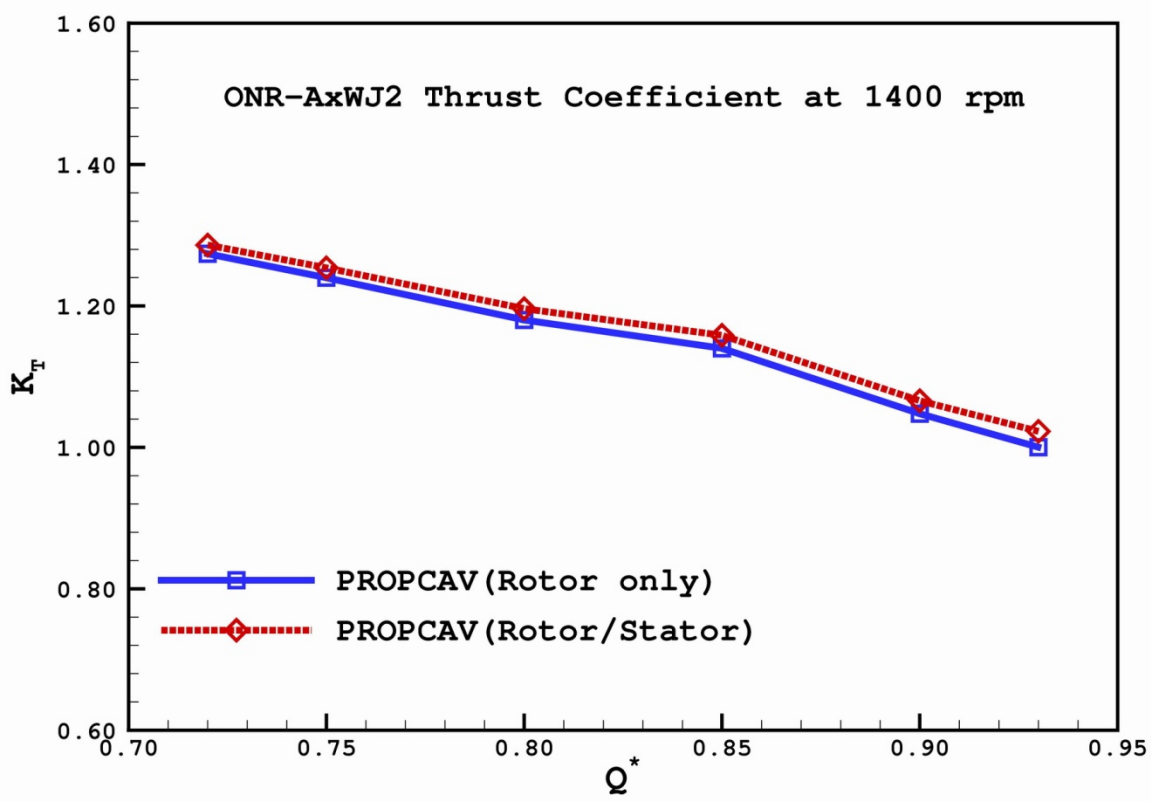

Figure 5.20: Predicted thrust coefficients on the rotor of the ONR AxWJ2 water-jet versus flow coefficients, with and without including the stator effect. C_f=0.004 and viscous pitch correction.

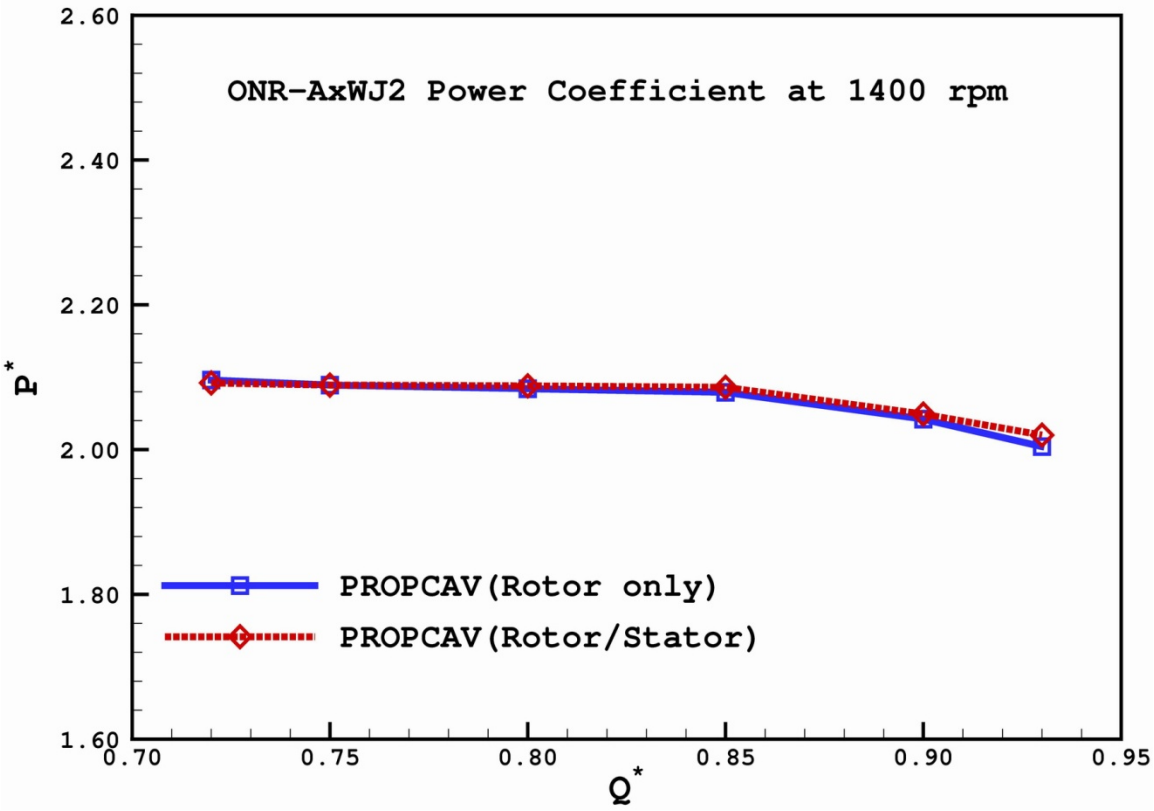

Figure 5.21: Predicted power coefficients on the rotor of the ONR AxWJ2 water-jet versus flow coefficients, with and without including the stator effect. C_f=0.004 and viscous pitch correction.

The comparison of pressure distributions including the influence of the stator on the casing inner surface is shown in Figure 5.22. The predicted results by the coupling method in 2-D axisymmetric domain have good agreements with those from the circumferentially averaged 3-D simulation. The power coefficients, pressure heads, and pump efficiency predicted by the present method at different flow coefficients are compared with the experimental data and those from 3-D FLUENT simulations as shown in Figure 5.23, 5.24, and 5.25, respectively. The predicted power coefficients by the present method have about 1.0% error compared with the measurements. The pressure heads obtained by using the coupling method have good correlations with the measurements the largest error is about 2.0% at Q^*=0.72. The predicted pump efficiency by the present method is about 1% error from the experimental data.

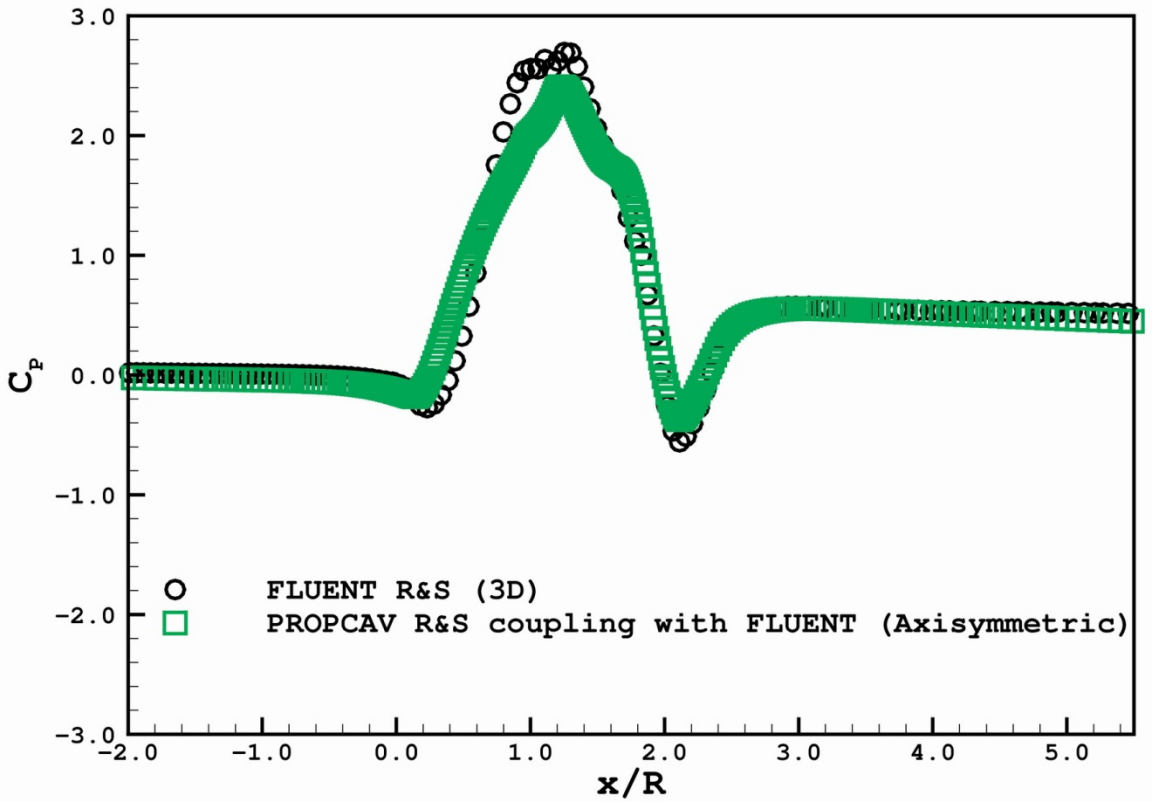

Figure 5.22: Comparison of C_P* on the casing surface of the ONR AxWJ2 water-jet for the rotor and stator interaction at $J_S = 1.19$ ($Q^* = 0.85$). Re=2.26×10^6.

* The source terms due to the rotor blade thickness (Kinnas et al. 2009) are not included in the continuity equation in RANS, and that may improve the correlation of pressures on the casing surface.

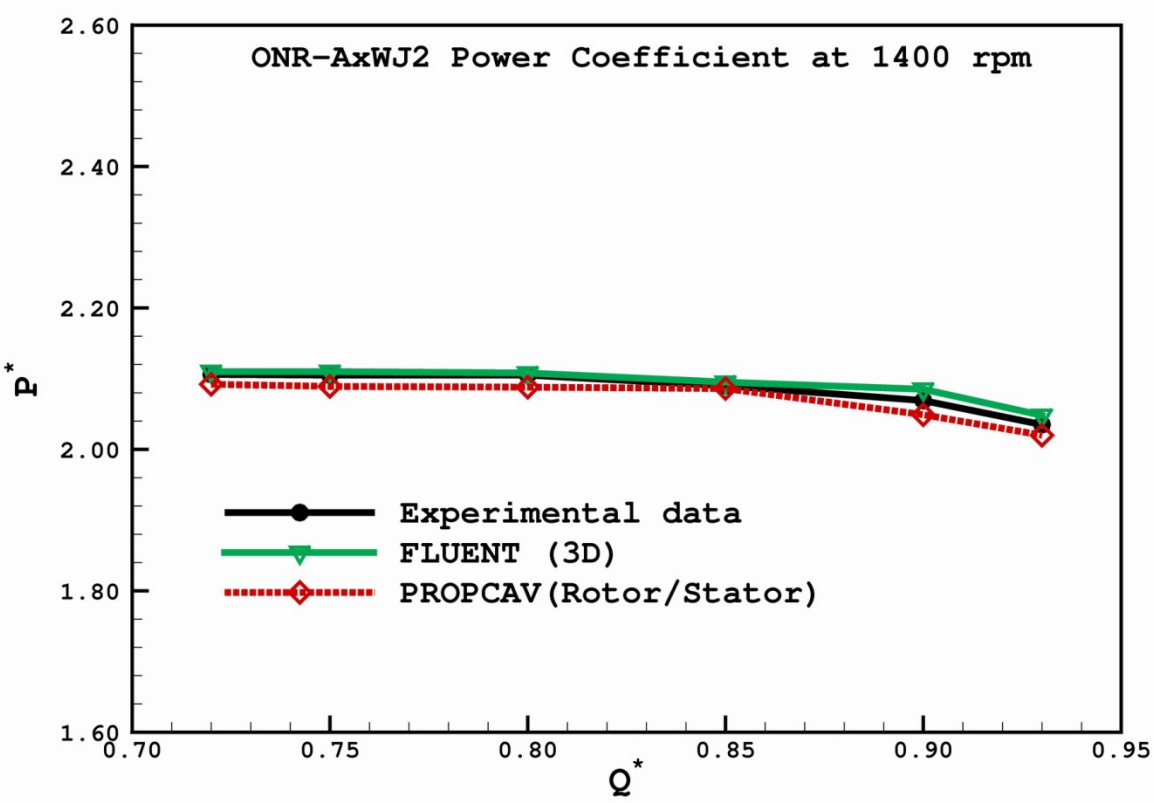

Figure 5.23: Comparison of the predicted power coefficients of the ONR AxWJ2 water-jet with the experimental data and FLUENT simulation from Chesnakas et al. (2009).

Q^*	Experiment	The present method (RS Interaction)	|Error| (%)
0.72	2.106	2.092	0.66
0.75	2.105	2.089	0.76
0.80	2.104	2.088	0.79
0.85	2.090	2.086	0.19
0.90	2.069	2.049	0.97
0.93	2.035	2.020	0.74

Table 5.4: Comparison of experimental and predicted power coefficients (P^*) of the ONR AxWJ2 water-jet at different flow coefficients (Q^*).

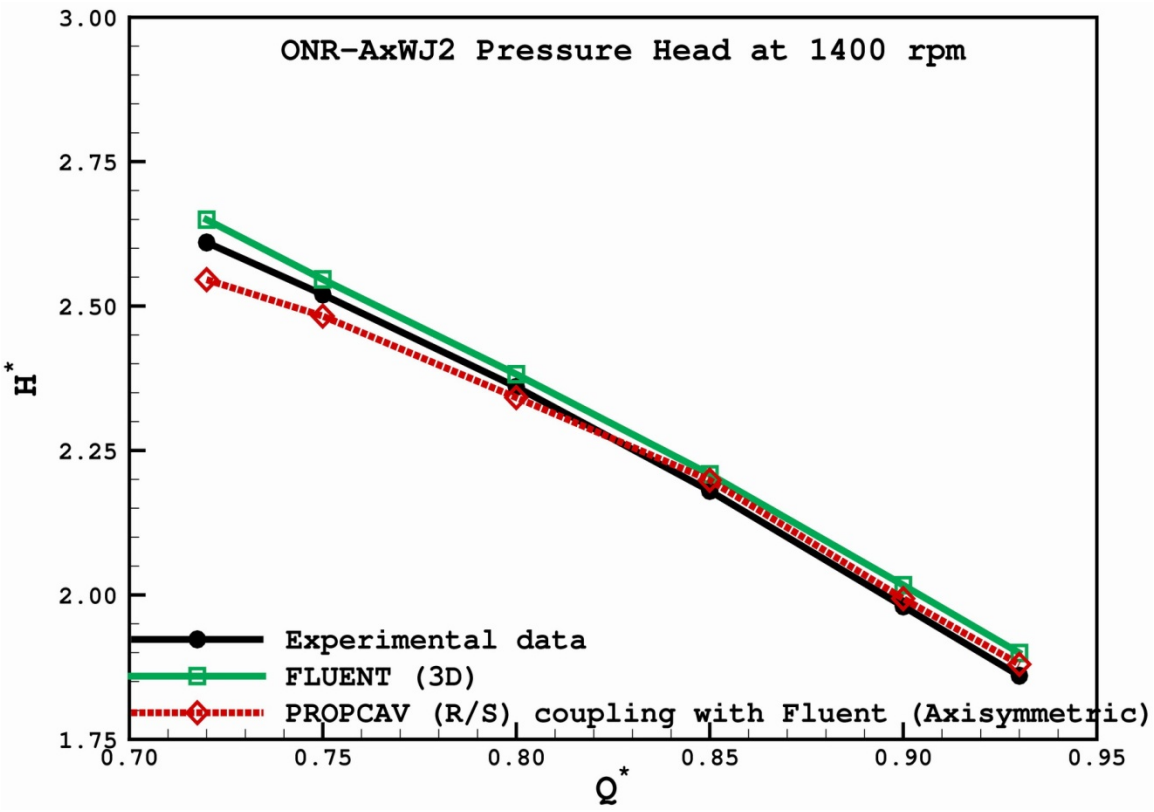

Figure 5.24: Comparison of the predicted pressure heads of the ONR AxWJ2 water-jet with the experimental data and FLUENT simulation from Chesnakas et al. (2009). Re=2.26×10^6.

Q^*	Experiment	The present method (RS Interaction)	|Error| (%)
0.72	2.61	2.55	2.30
0.75	2.52	2.48	1.59
0.80	2.36	2.34	0.85
0.85	2.18	2.20	0.92
0.90	1.98	1.99	0.51
0.93	1.86	1.88	1.08

Table 5.5: Comparison of experimental and predicted pressure heads (H^*) of the ONR AxWJ2 water-jet at different flow coefficients (Q^*).

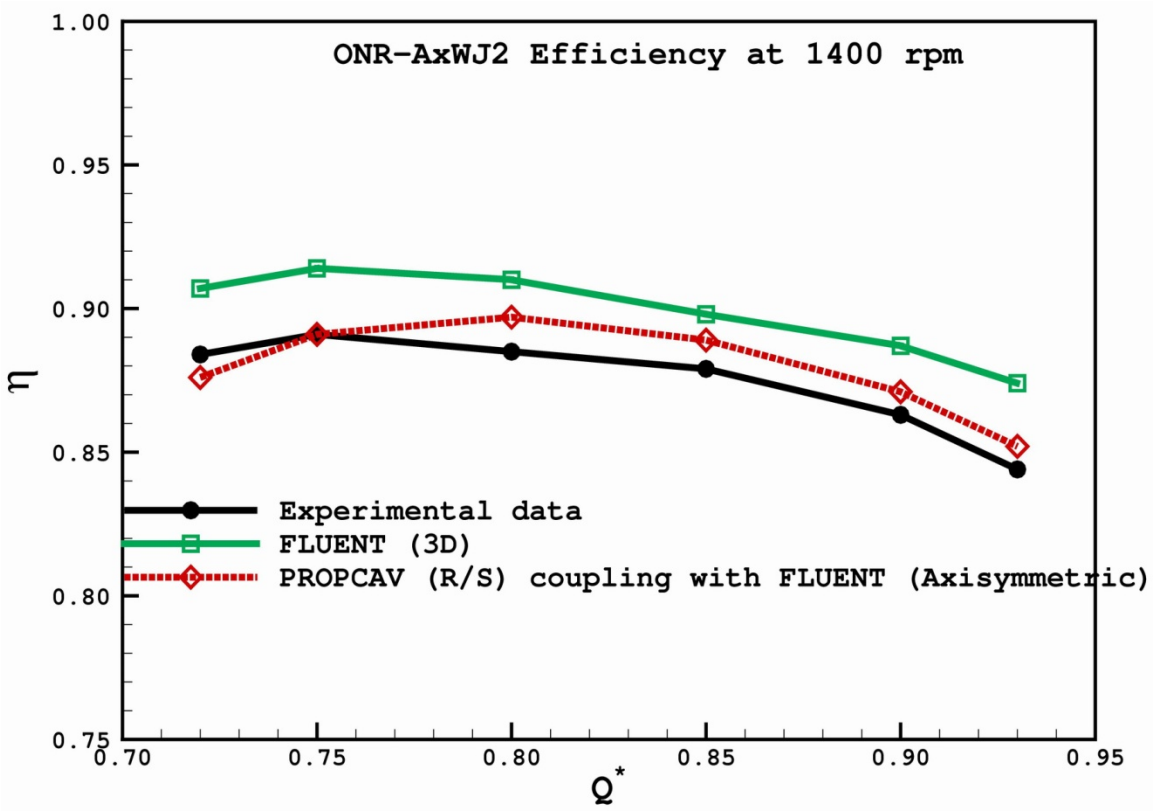

Figure 5.25: Comparison of the predicted efficiency of the ONR AxWJ2 water-jet with the experimental data and FLUENT simulation from Chesnakas et al. (2009). Re=2.26×10^6.

Q^*	Experiment	The present method (RS Interaction)	|Error| (%)
0.72	0.884	0.876	0.90
0.75	0.891	0.891	0.00
0.80	0.885	0.897	1.36
0.85	0.879	0.889	1.14
0.90	0.863	0.871	0.93
0.93	0.844	0.852	0.95

Table 5.6: Comparison of experimental and predicted efficiency (η) of the ONR AxWJ2 water-jet at different flow coefficients (Q^*).

5.4 SUPER CAVITATION AND THRUST BREAKDOWN

In this section, the thrust breakdown due to super cavitation is simulated by the present method for the rotor only calculation without the effects from the stator. In addition, it should be noted that in the experiment Q^* was reduced due to the chocking of cavities inside the pump. The value of Q^* measured in the experiment were used in the simulations by the present method.

The experimental values and the numerical computations of the normalized thrust and torque at Q^*=0.83 are compared as shown in Figure 5.26 and Figure 5.27. The comparison of pressure distributions between cavitating and fully-wetted solutions at r/R=0.988 for Q^*=0.83 and N^*=0.993 (where the pump performance, or thrust breakdown, is of 1% drop in torque at Q^*=0.83) is shown in Figure 5.28. The cavity pattern and its corresponding circulation distributions on the rotor blade at Q^*=0.83 and N^*=0.993 are presented in Figure 5.29 and Figure 5.30, respectively. The normalized thrust and torque at Q^*=0.774 from the experiment and the present method are compared and shown in Figure 5.31 and Figure 5.32. The comparison of pressure distributions between cavitating and fully-wetted solutions at r/R=0.988 for Q^*=0.774 and N^*=0.901 (where the pump performance, or thrust breakdown, is of 1% drop in torque at Q^*=0.774) is shown in Figure 5.33. The cavity pattern and its corresponding circulation distributions on the rotor blade at Q^*=0.774 and N^*=0.901 are presented in Figures 5.34 and 5.35. The normalized thrust and torque at Q^*=0.711 from the experiment and the present method are compared and shown in Figures 5.36 and 5.37. The comparison of pressure distributions between cavitating and fully-wetted solutions at four different sections for Q^*=0.711 and N^*=0.743 (where the pump performance, or thrust breakdown, is of 1% drop in torque at Q^*=0.711) are shown in Figure 5.38. The cavity pattern and its

corresponding circulation distributions on the rotor blade at Q^*=0.711 and N^*=0.743 are presented in Figures 5.39 and 5.40, respectively.

Due to the occurrence of super cavities, the circulation distributions at certain sections drop significantly and are lower than those under fully wetted condition. Under cavitating conditions, the pressure difference between the pressure and suction sides becomes limited, and finally decreases when the extent of cavitation is increased. When most of the rotor surface is covered by cavity bubbles, the pressure difference between the pressure side and suction side of the blade drops considerably, and so does the thrust and torque produced by the impeller.

Generally, the thrust breakdown phenomenon can be predicted by the present method and the trend of the prediction follows that of the experimental data.

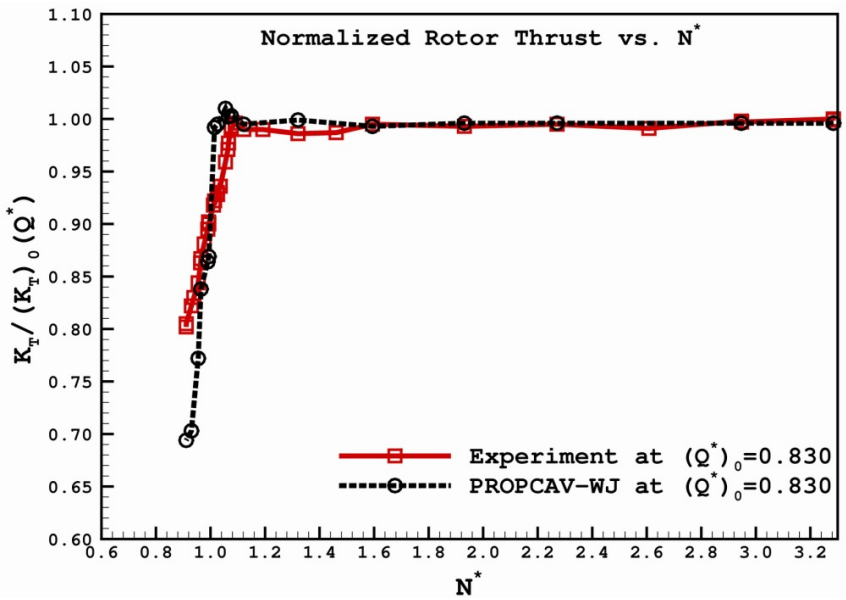

Figure 5.26: Comparison of the rotor normalized thrust of the ONR AxWJ2 water-jet predicted by the present method (at Q^*=0.83) with the experimental data for various flow coefficients (N^*) from Chesnakas et al. (2009). C_f=0.004 and viscous pitch correction.

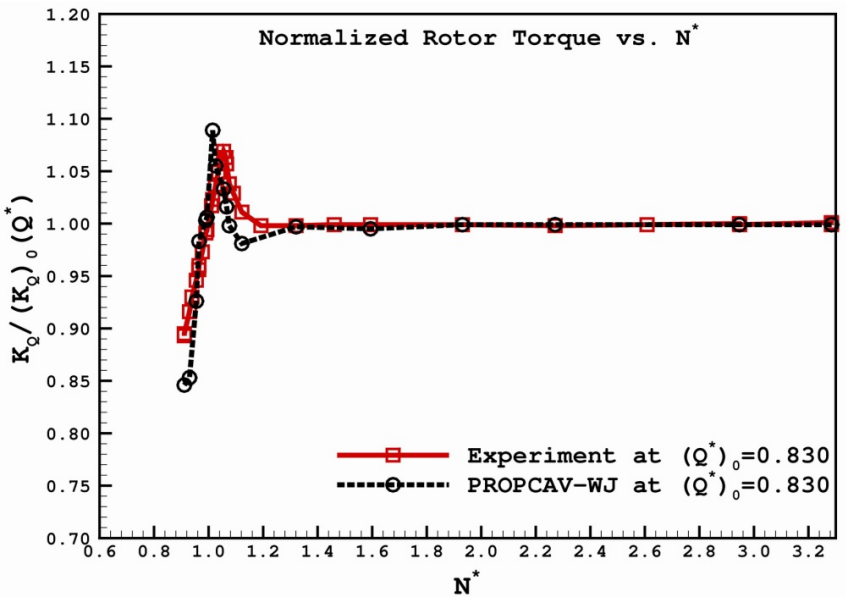

Figure 5.27: Comparison of the rotor normalized torque of the ONR AxWJ2 water-jet predicted by the present method (at Q^*=0.83) with the experimental data for various flow coefficients (N^*) from Chesnakas et al. (2009). C_f=0.004 and viscous pitch correction.

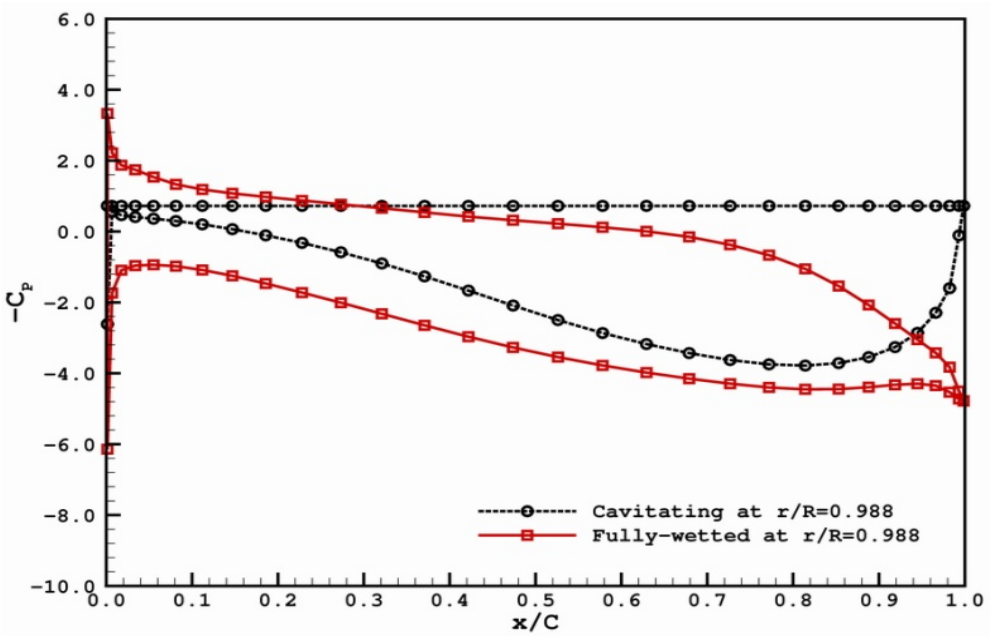

Figure 5.28: Pressure distributions on the rotor of the ONR AxWJ2 water-jet predicted by the present method at the section of r/R=0.988. Comparison between fully-wetted and cavitating solutions (at Q^*=0.830 and N^*=0.993).

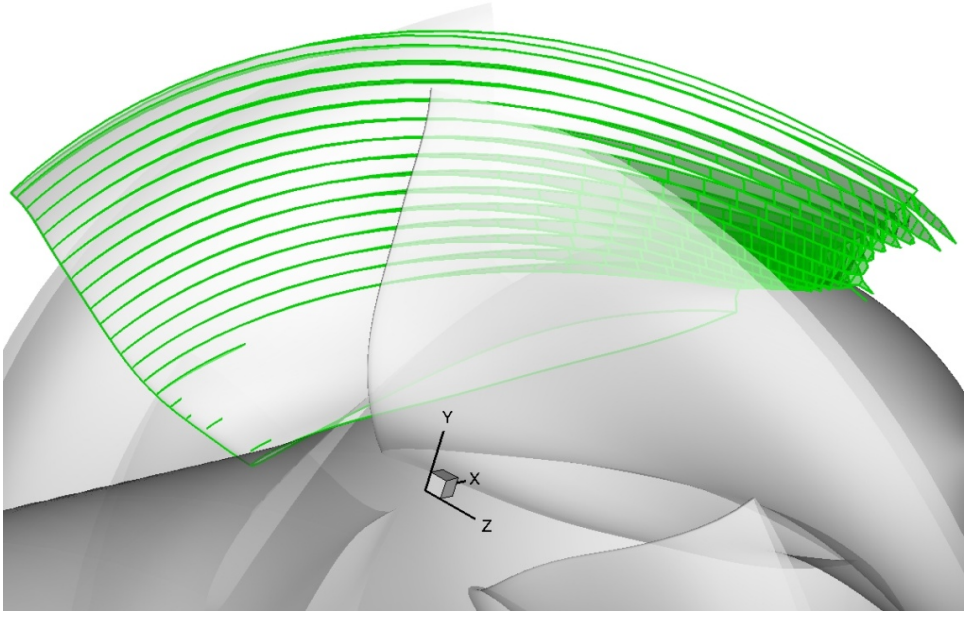

Figure 5.29: Cavity patterns on the rotor of the ONR AxWJ2 water-jet predicted by the present method (at Q^*=0.830 and N^*=0.993).

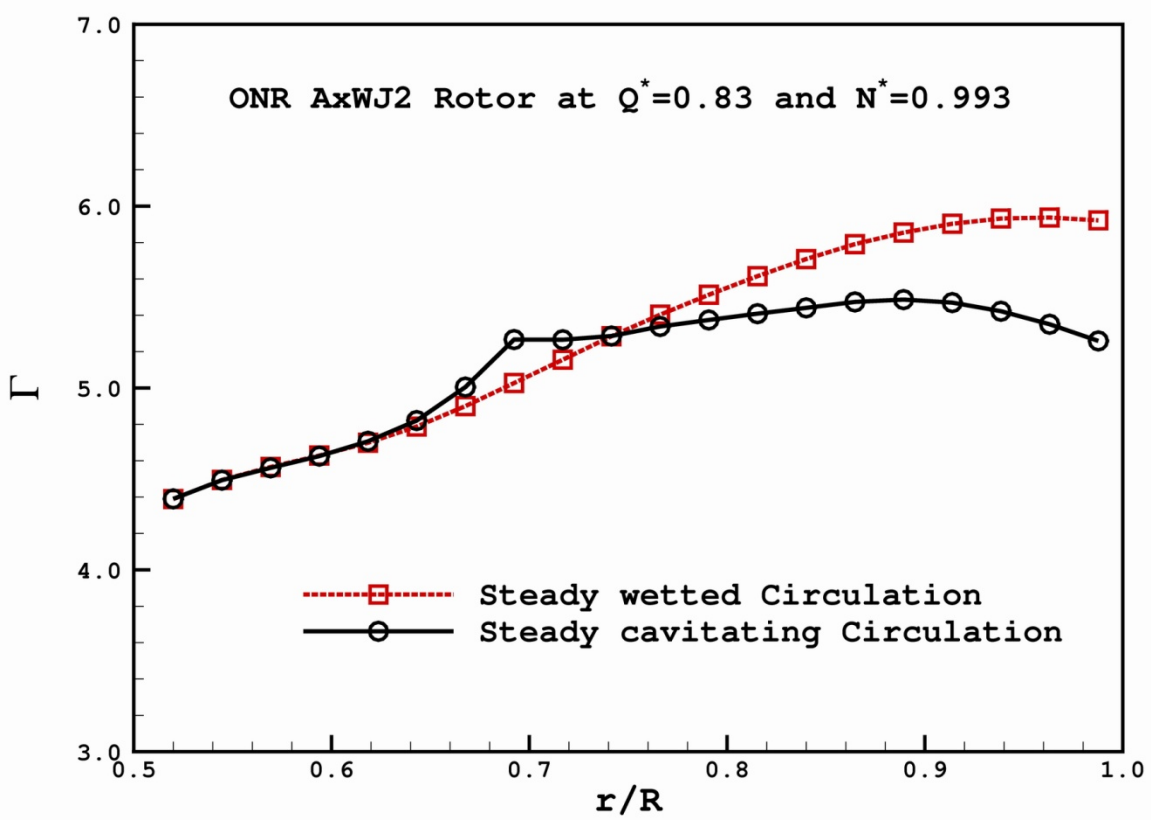

Figure 5.30: Comparison of the fully-wetted and cavitating circulation distributions on the rotor of the ONR AxWJ2 water-jet predicted by the present method (at Q^*=0.830 and N^*=0.993).

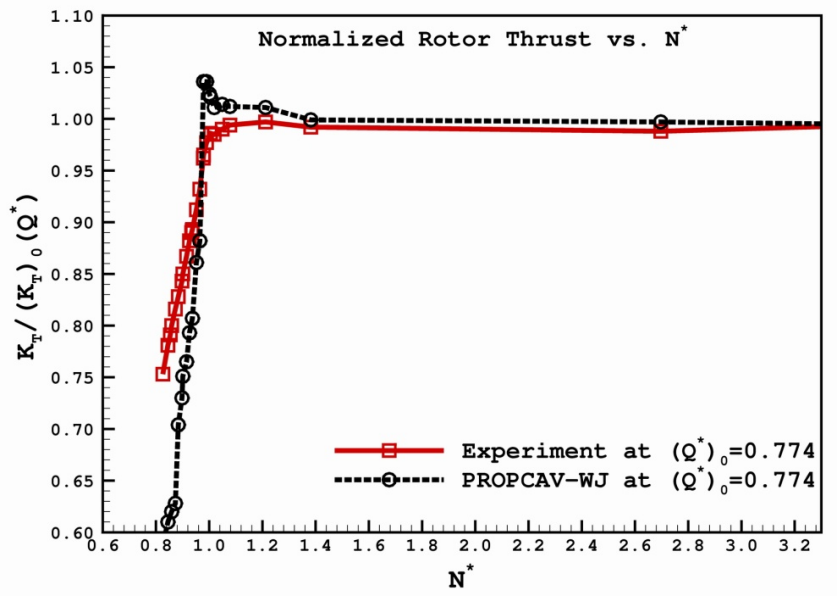

Figure 5.31: Comparison of the rotor normalized thrust of the ONR AxWJ2 water-jet predicted by the present method (at Q^*=0.774) with the experimental data for various flow coefficients (N^*) from Chesnakas et al. (2009). C_f=0.004 and viscous pitch correction.

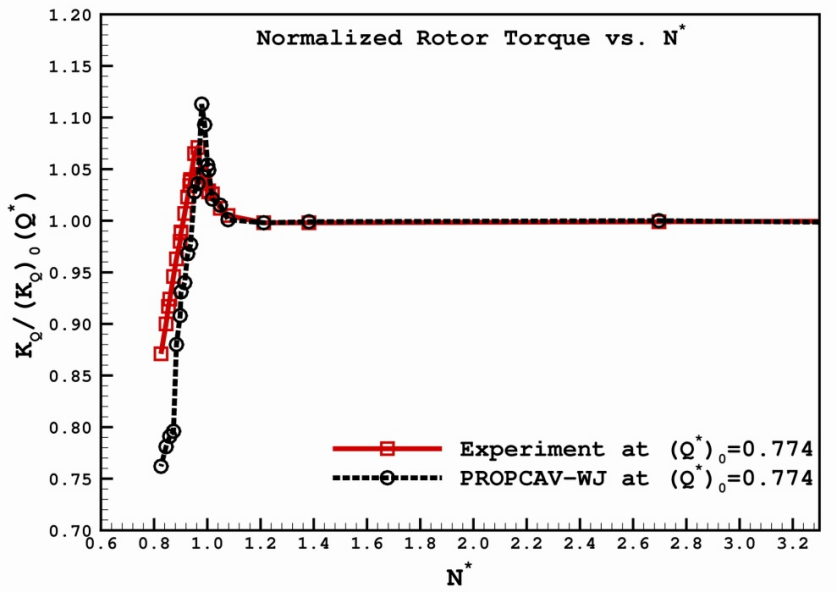

Figure 5.32: Comparison of the rotor normalized torque of the ONR AxWJ2 water-jet predicted by the present method (at Q^*=0.774) with the experimental data for various flow coefficients (N^*) from Chesnakas et al. (2009). C_f=0.004 and viscous pitch correction.

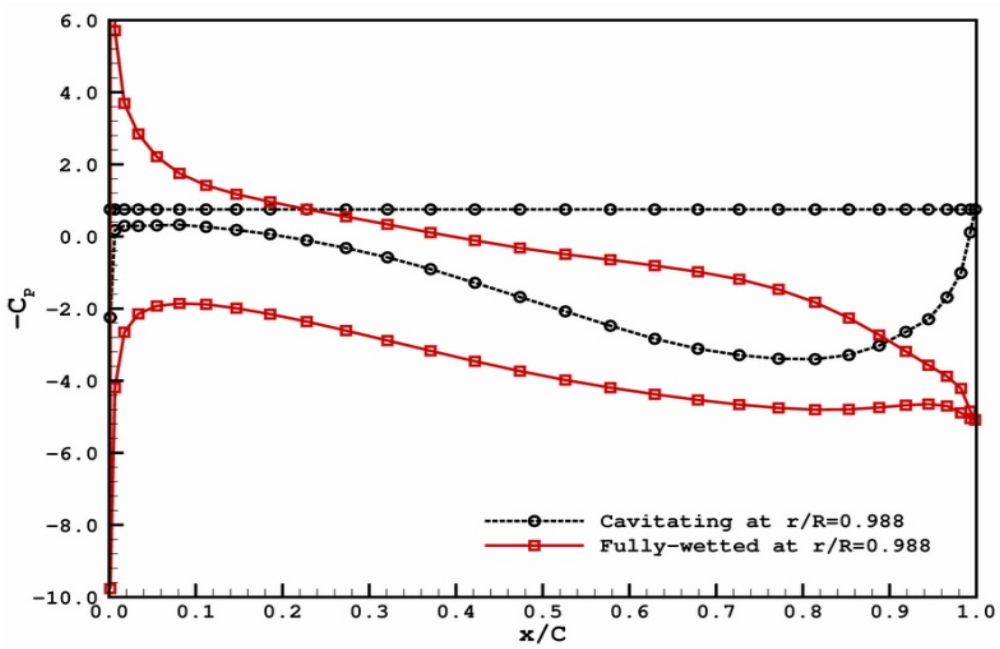

Figure 5.33: Pressure distributions on the rotor of the ONR AxWJ2 water-jet predicted by the present method at the section of r/R=0.988. Comparison between fully-wetted and cavitating solutions (at Q^*=0.774 and N^*=0.901).

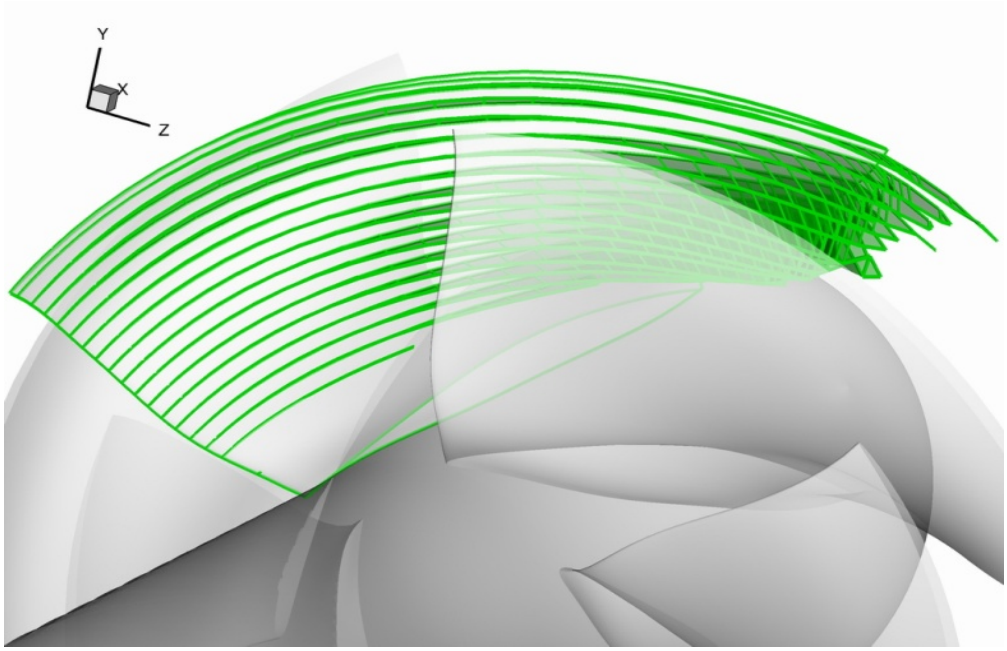

Figure 5.34: Cavity patterns on the rotor blade of the ONR AxWJ2 water-jet predicted by the present method (at Q^*=0.774 and N^*=0.901).

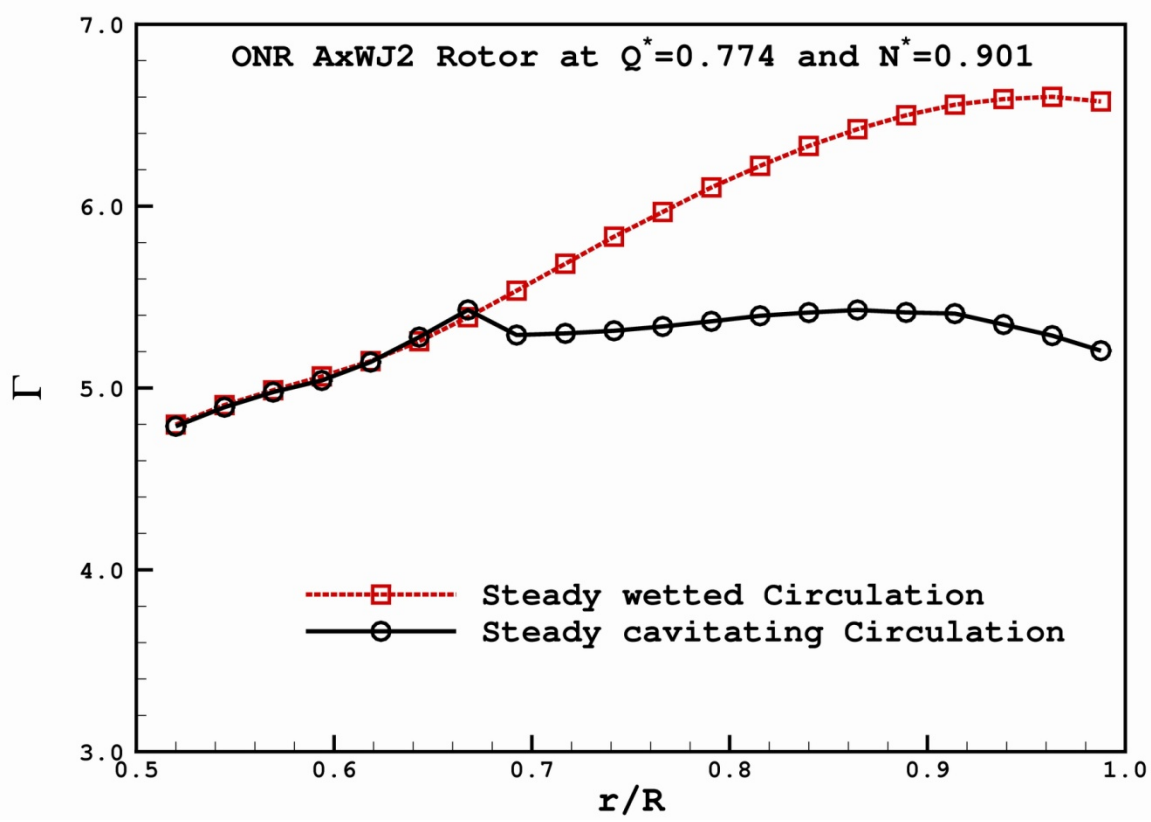

Figure 5.35: Comparison of the fully-wetted and cavitating circulation distributions on the rotor of the ONR AxWJ2 water-jet predicted by the present method (at Q^*=0.774 and N^*=0.901).

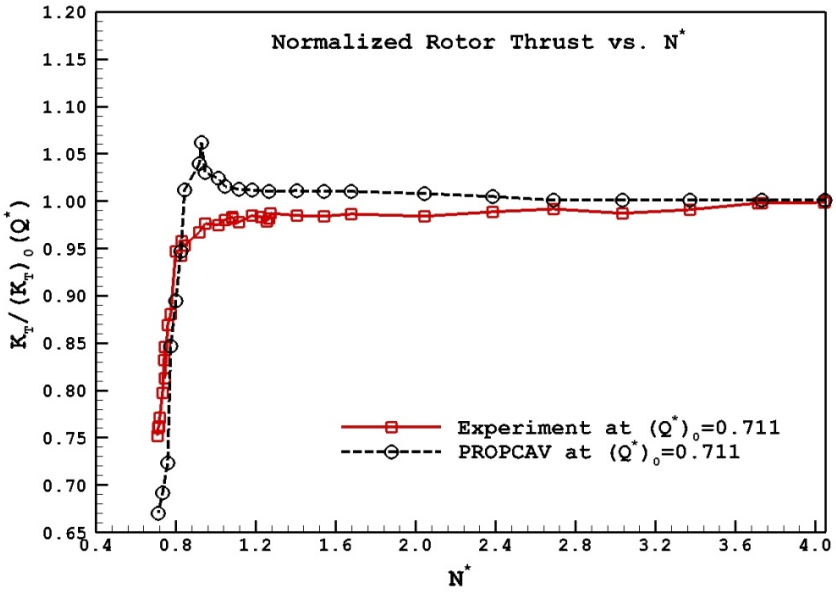

Figure 5.36: Comparison of the rotor normalized thrust of the ONR AxWJ2 water-jet predicted by the present method (at Q^*=0.711) with the experimental data for various flow coefficients (N^*) from Chesnakas et al. (2009). C_f=0.004 and viscous pitch correction.

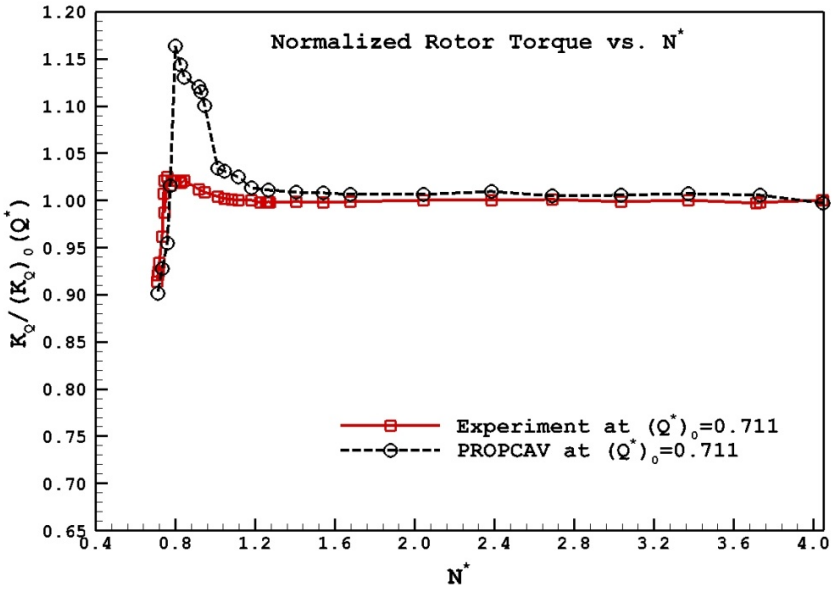

Figure 5.37: Comparison of the rotor normalized torque of the ONR AxWJ2 water-jet predicted by the present method (at Q^*=0.711) with the experimental data for various flow coefficients (N^*) from Chesnakas et al. (2009). C_f=0.004 and viscous pitch correction.

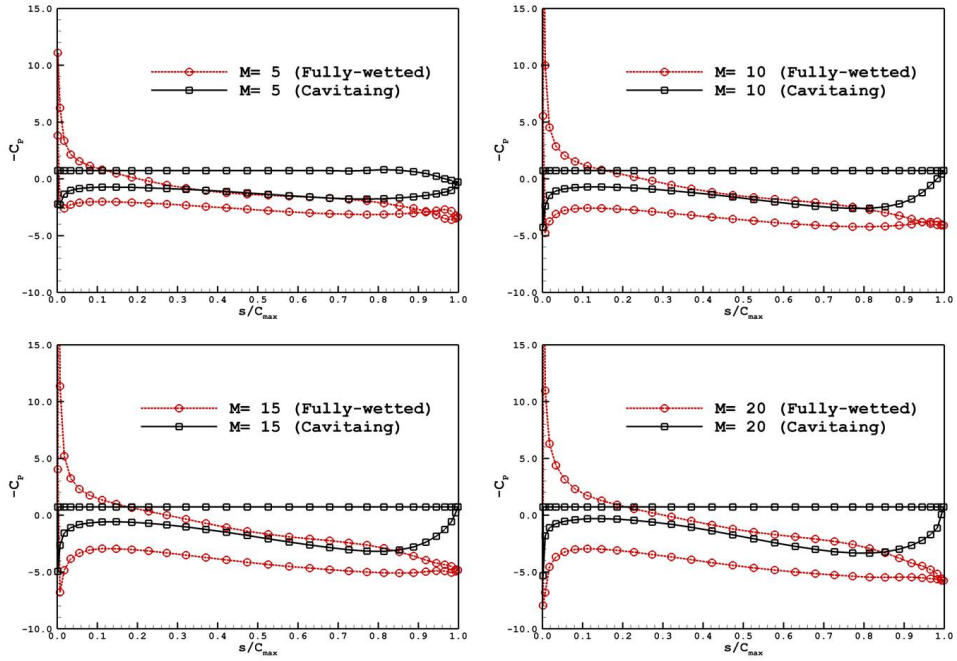

Figure 5.38: Pressure distributions on the rotor at four different sections of the ONR AxWJ2 water-jet predicted by the present method. Comparison between fully-wetted and cavitating solutions (at Q^*=0.711 and N^*=0.743).

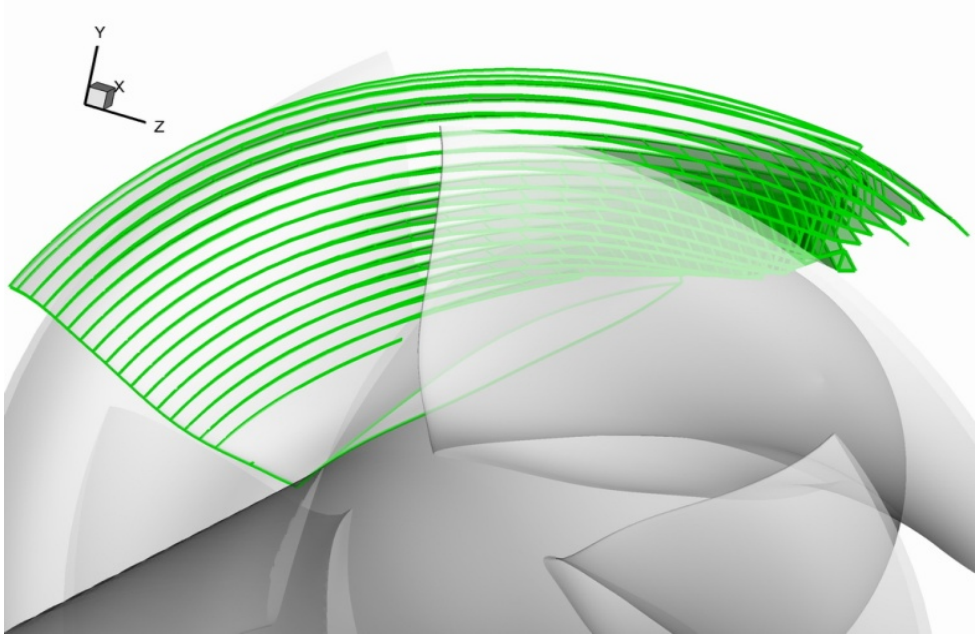

Figure 5.39: Cavity patterns on the rotor blade of the ONR AxWJ2 water-jet predicted by the present method (at Q^*=0.711 and N^*=0.743).

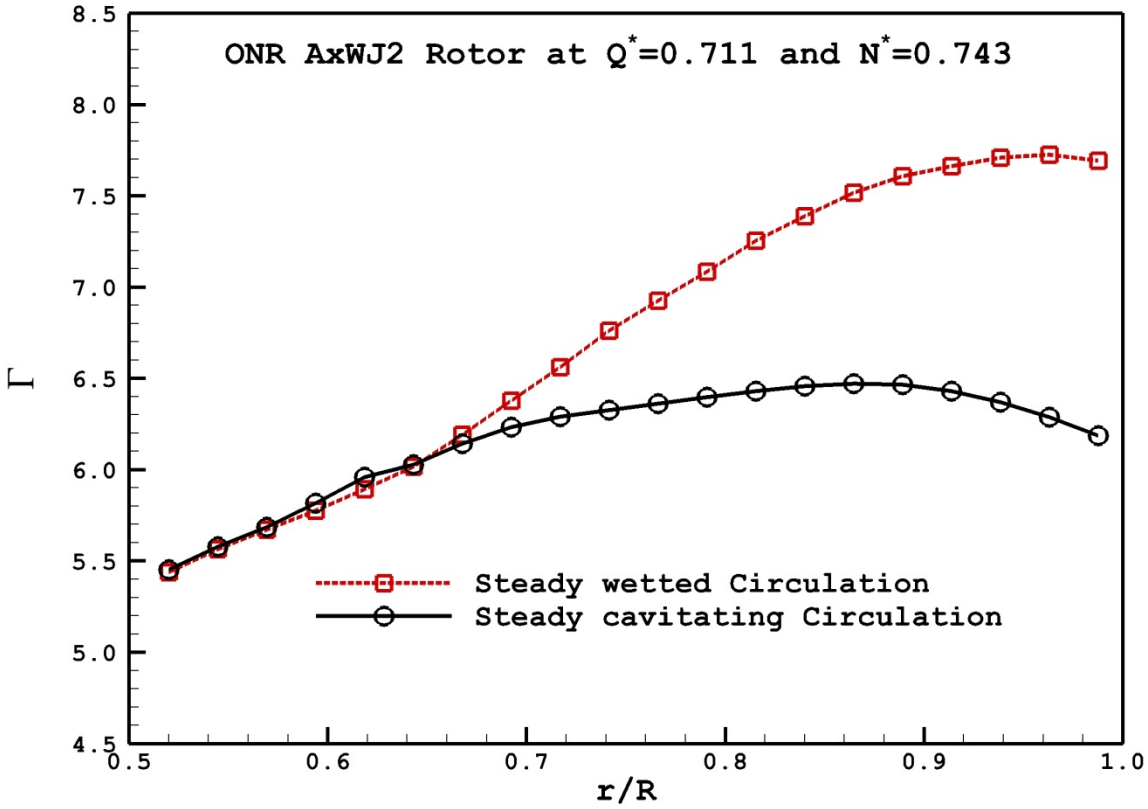

Figure 5.40: Comparison of the fully-wetted and cavitating circulation distributions on the rotor of the ONR AxWJ2 water-jet predicted by the present method (at Q^*=0.711 and N^*=0.743).

5.5 THE TIP GAP MODEL FOR ROTOR ONLY CALCULATION

The effect of a gap size is studied before applying the tip gap model to the ONR-AxWJ2 water-jet rotor. Figure 5.41 shows the circulation distributions on the rotor for various gap values, 0% (sealed gap); 0.33% (real size in the design); 0.5%; 1%; 2%. It can be observed that a small difference of the gap sizes can influence the circulation distributions on the rotor drastically. To see the effect of the present tip gap model, the gap is represented by an extra row of panels, and the boundary condition of Equation (3.35) is applied to the gap for various discharge coefficients between 0.0 and 1.0. Figure 5.42 shows the sensitivity of the rotor circulations to different discharge coefficients. C_Q =0.0 corresponds to the sealed gap while C_Q=1.0 implies the case where there is no energy loss by the fluid as it passes through the clearance. It may be noticed that the case of C_Q=1.0 does not follow the behavior of non-zero gap in Figure 5.42. It is because the different boundary conditions are applied to the blade panels adjacent to the inner wall of the casing, and the pressure differences exist between the pressure side and suction side of the blade tip. The pressure distributions on the rotor at a constant strip where r/R=0.99 are compared with 3-D FLUENT simulation for the rotor only calculation as shown in Figure 5.43.

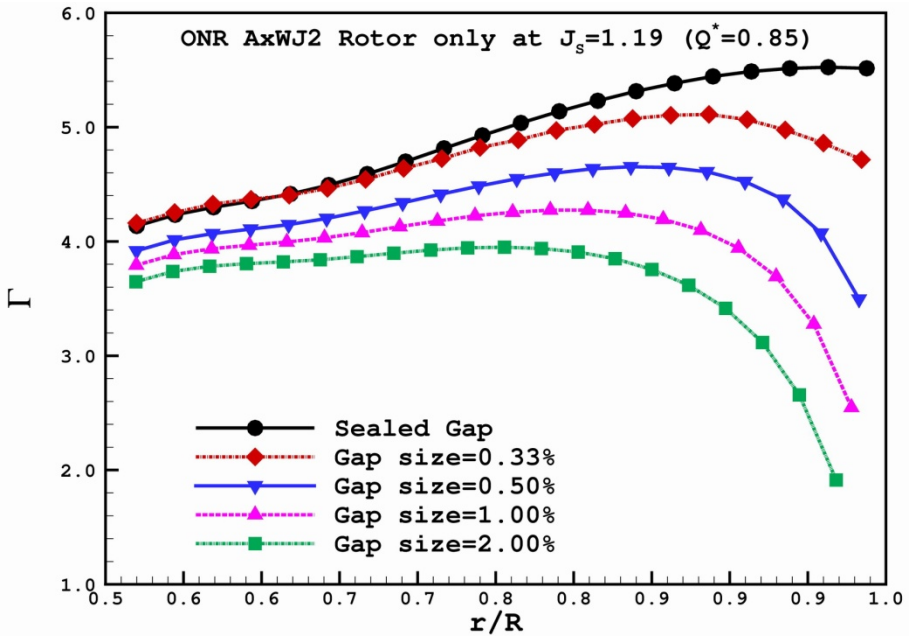

Figure 5.41: Circulation distributions on the rotor blade of the ONR AxWJ2 water-jet with varying gap distance from the inner surface of a shroud.

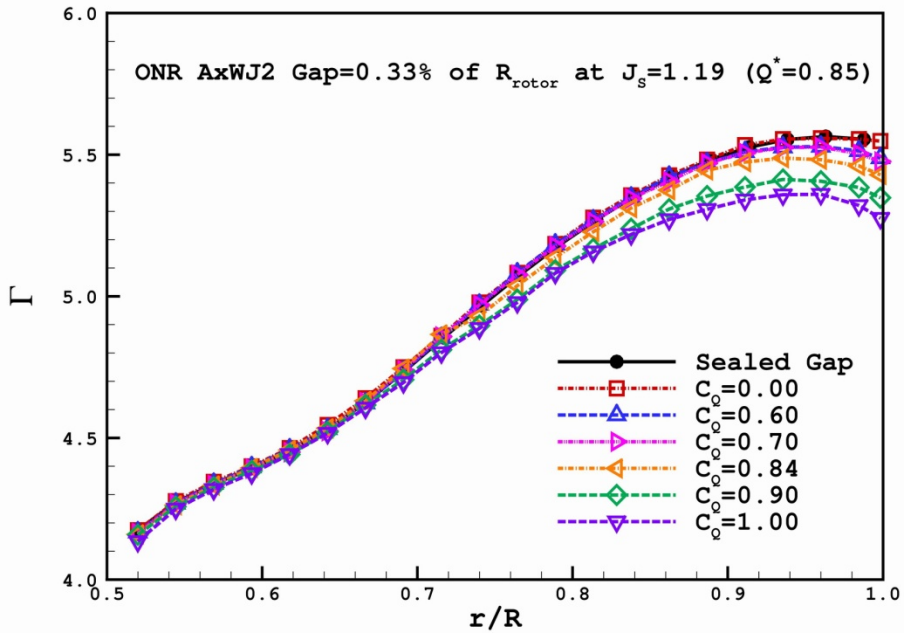

Figure 5.42: Sensitivity of the circulation distributions on the rotor blade of the ONR AxWJ2 water-jet to the discharge coefficient (C_Q) and gap size is 0.33% of the rotor radius.

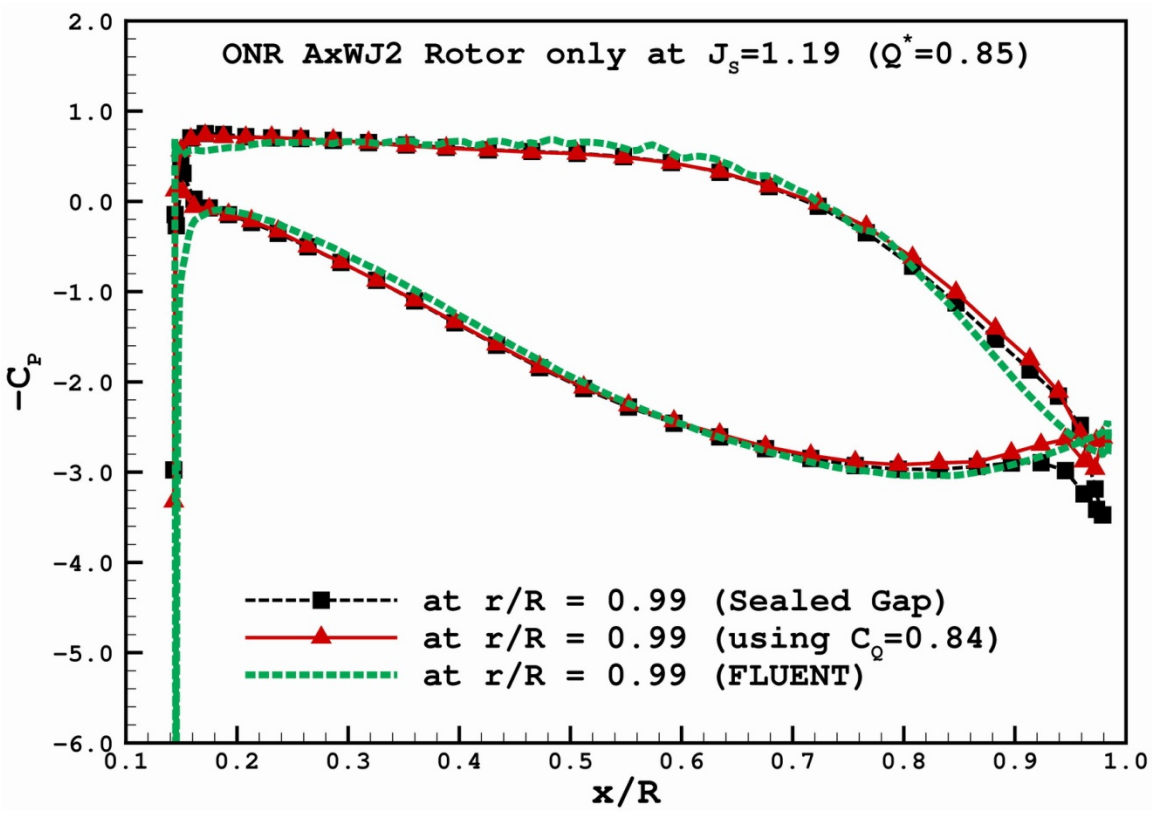

Figure 5.43: Comparison of -C_P on the rotor blade of the ONR AxWJ2 water-jet at a strip of constant r/R=0.99 predicted by the present method.

5.6 THE STEADY WAKE ALIGNMENT FOR ROTOR ONLY CALCULATION

The effect of a full wake alignment to the ONR AxWJ2 rotor performance is studied in this section. The original pitch wake alignment model simply applies the rotor blade pitch to alignment its trailing wake. However, in order to take the influences of all the geometry components into account, Equation (3.36) is used to evaluate the induced velocities on the wake surface by the rotor, hub and casing. Figure 5.44 shows the comparison of the wake shapes by using pitch alignment model and by applying full wake alignment model. The procedure of full wake alignment takes 6 iterations about 5 minutes to determine the final wake geometry. The history of the rotor circulation distributions during the iteration process is shown in Figure 5.45. Table 5.7 shows the power coefficient (P^*) from the experiment and those predicted by using full wake alignment. The comparison of power coefficient is shown in Figure 5.46. After applying full wake alignment, the power coefficients increase about 0.9~1.8% higher than those of using pitch alignment.

Q^*	Experiment	The present Method	|Error| (%)
0.72	2.106	2.134	1.33
0.75	2.105	2.127	1.05
0.80	2.104	2.117	0.62
0.85	2.090	2.095	0.24
0.90	2.069	2.055	0.68
0.93	2.035	2.021	0.69

Table 5.7: Comparison of experimental and predicted power coefficients (P^*) by the present method for the rotor only simulation of the ONR AxWJ2 water-jet with full wake alignment at different flow coefficients (Q^*).

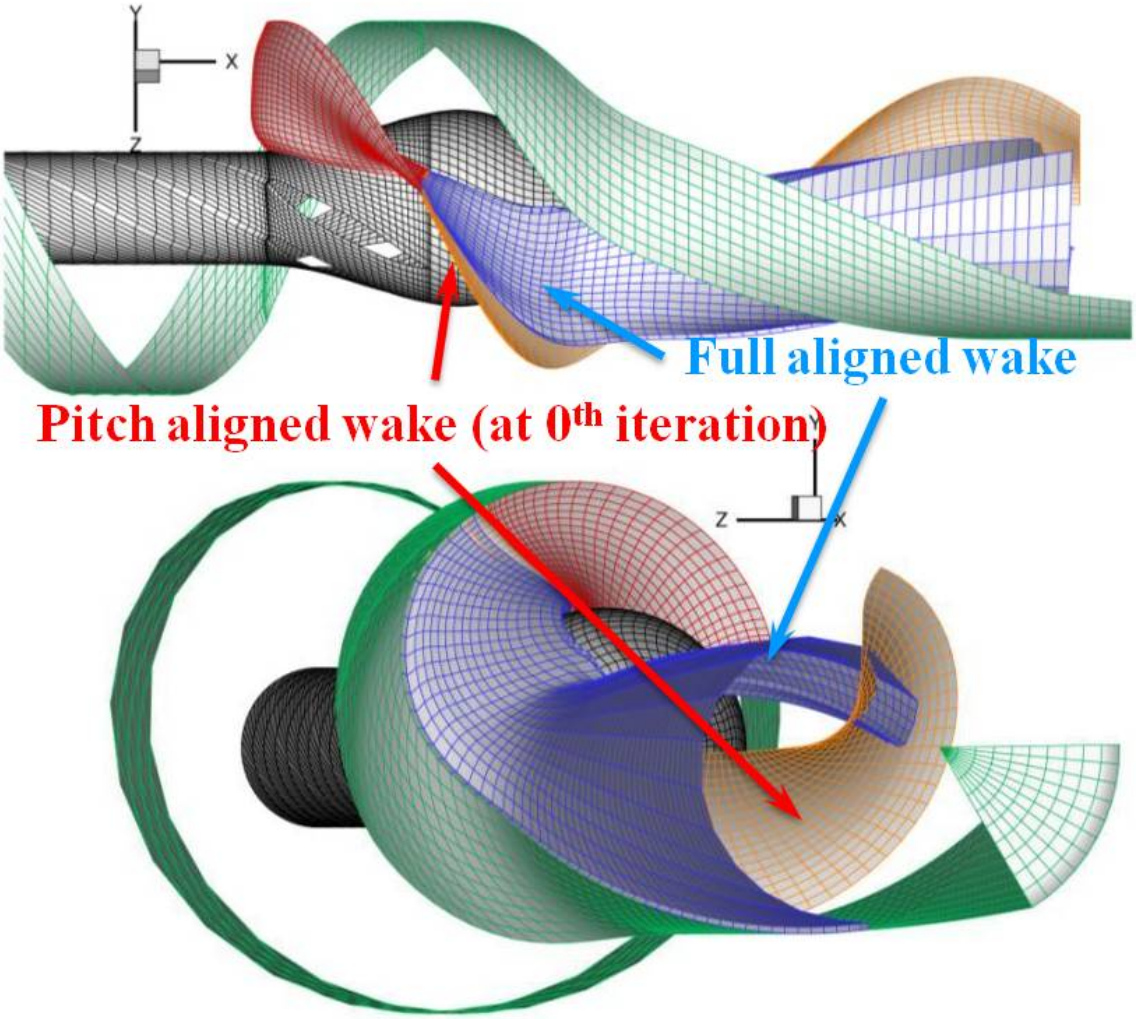

Figure 5.44: Comparison of the wake geometries of the ONR AxWJ2 water-jet by using pitch alignment and by applying full wake alignment.

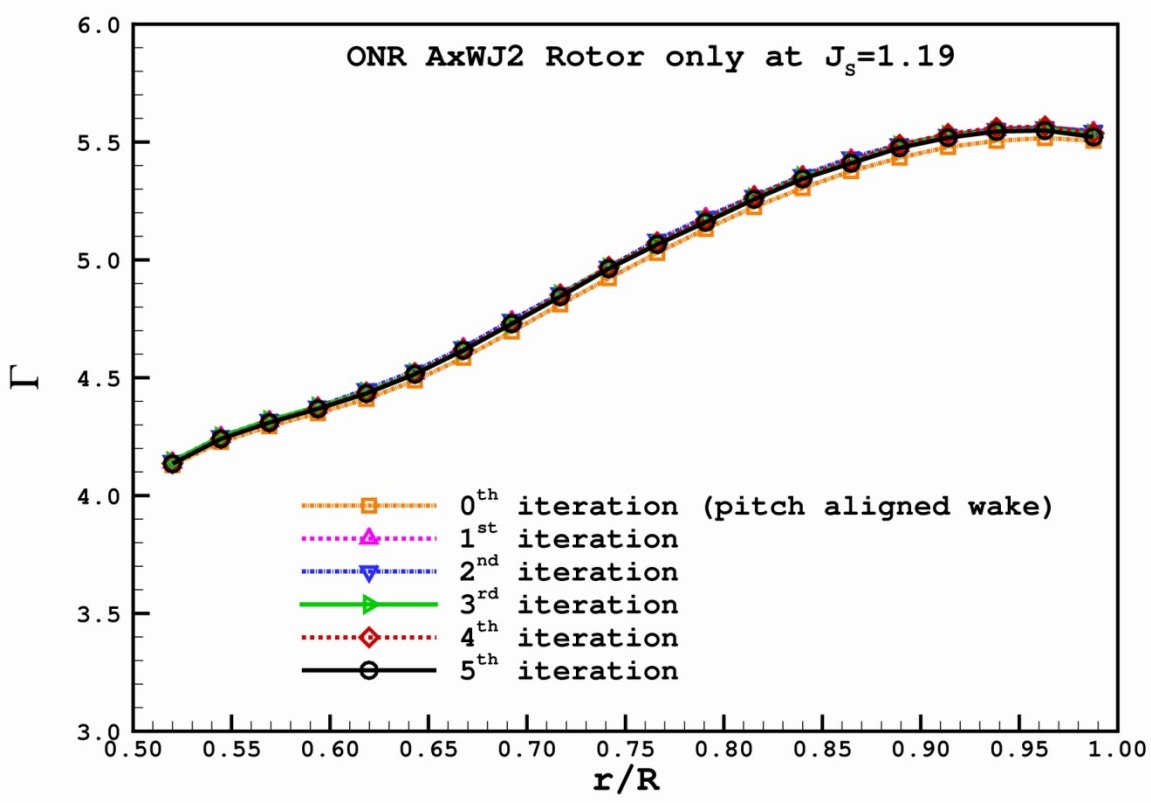

Figure 5.45: The rotor circulation distribution history of the ONR AxWJ2 water-jet at J_S=1.19 during the iterations. Rotor only without the effect of the stator.

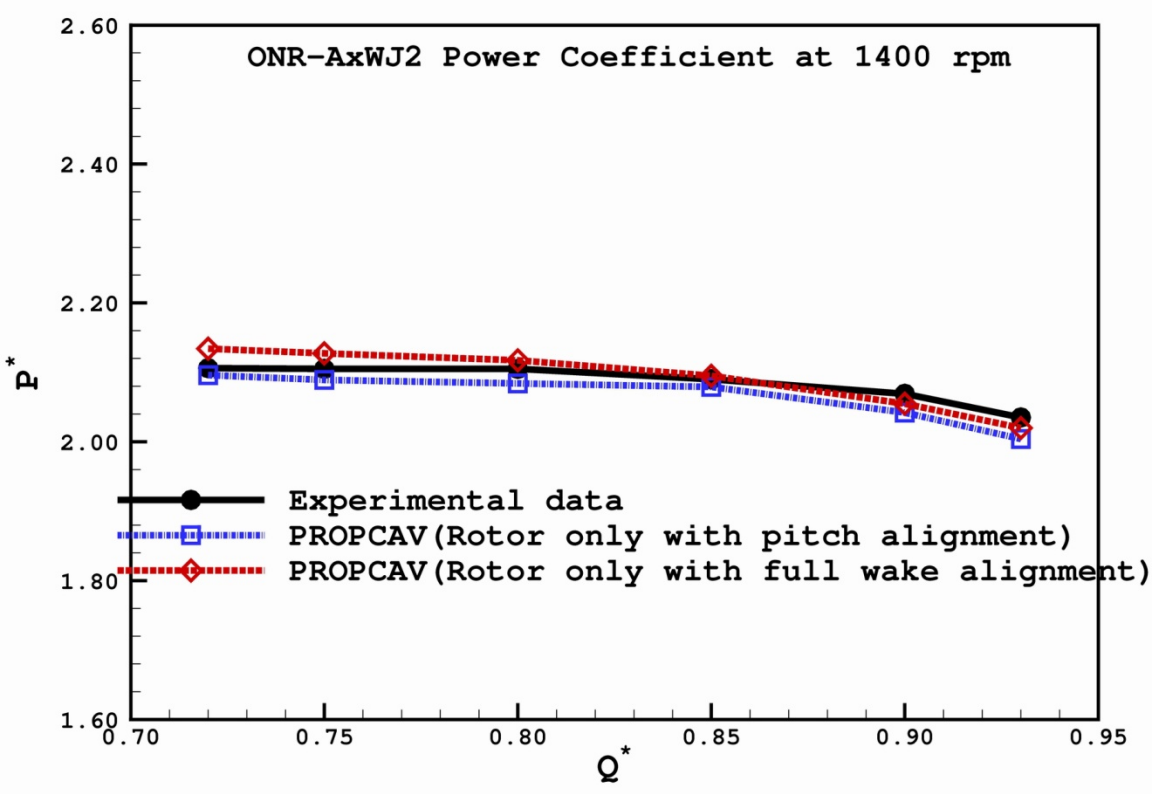

Figure 5.46: Comparison of the predicted power coefficients of the ONR AxWJ2 water-jet with the experimental data from Chesnakas et al. (2009).

5.7 UNSTEADY ROTOR ONLY CALCULATION

This section describes the results of a cavitating rotor calculation subject to a non-uniform inflow. The problem is unsteady in nature.

The time marching scheme is required in the unsteady calculation and is identical to that described in Fine (1992). A constant time step Δt is used. At each time step, the rotor blades rotate by an angle increment $\Delta\theta=\omega\Delta t$. Notice that in Equations (3.14) and (3.15), $\frac{\partial\phi}{\partial t}$ is assumed to be known. At each time step, the solution (ϕ) is only obtained for the key blade. The influence of each of the other blades is accounted for by using the solution from the previous time step when the key blade was in the position of that blade. The cavity thickness are calculated by differentiating Equations (3.17) and (3.19) with a second order central finite difference method. The correct cavity shape for each time step is achieved iteratively by using a Newton-Raphson scheme which requires the cavity closure condition to be satisfied.

Figure 5.47 shows a non-uniform inflow upstream of the ONR AxWJ2 water-jet pump measured in the Large Cavitation Channel (LCC*). For the given flow conditions (J_S=1.40, σ_n=2.50 and Fr=16.916), the dominant cavity patterns for the rotor are leading edge backside partial cavities.

Since the problem is unsteady, the numerical solutions depend on the time step size, which is expressed in terms of an angle increment, Δθ, in the present method. Four different angle increments, $\Delta\theta = 3^\circ, 4^\circ, 5^\circ$ and 6° are used. The effect of different time

* Pump system tests were conducted in the NSWCCD Large Cavitation Channel (LCC) in Memphis Tennessee. The LCC is a variable-pressure, re-circulating, cavitation tunnel with a test section that is 10×10 feet in cross section and 43 feet in length. Maximum velocity in the test section is 35 knots, and the pressure in the test section can be varied from 0.5 to 60 psi. The LCC employs hydro-acoustic silencing techniques for reducing acoustic reverberation introduced by the water flow of the tunnel.

steps on the predicted rotor cavitating mean circulation distributions is shown in Figure 5.48. As shown in the figure, the results are not sensitive to the time step size of the case.

In addition to the time step size, the panel discretization may also affect the convergence of the solution. The dependence of cavitating mean circulations on the rotor with different number of panels in the chord-wise direction and span-wise direction of the blade are shown in Figure 5.49 and 5.50, respectively. In Figure 5.50, the circulation distributions are also consistent except somewhat discrepancies from those of 10 elements in the span-wise direction. 20 circumferential elements are used between two blades on the hub and casing while doing these two convergence tests. Changing the number of panels on the rotor blade does not affect the unsteady cavitating prediction significantly. Figure 5.51 shows the convergence of the cavitating mean circulations on the rotor with number of panels in the circumferential direction between two blades. The figure shows slight discrepancies of the results close to the tip region, and using at least 20 elements in the circumferential direction is suggested for achieving convergent results.

Since the method accounts for the effect of other blades on the key blade in a progressive manner, the solutions depends on the number of revolutions. Figure 5.52 shows the convergence of the key forces with number of revolutions. The variation of the cavity volume with angel of rotation is shown in Figure 5.53. As shown in the two figures, the solution converged at the fourth revolution for this case.

The unsteady cavity patterns on the key blade at different time step are presented in Figure 5.54. The unsteady fully-wetted and cavitating thrust and torque coefficients per blade at different time step are shown in Figure 5.55.

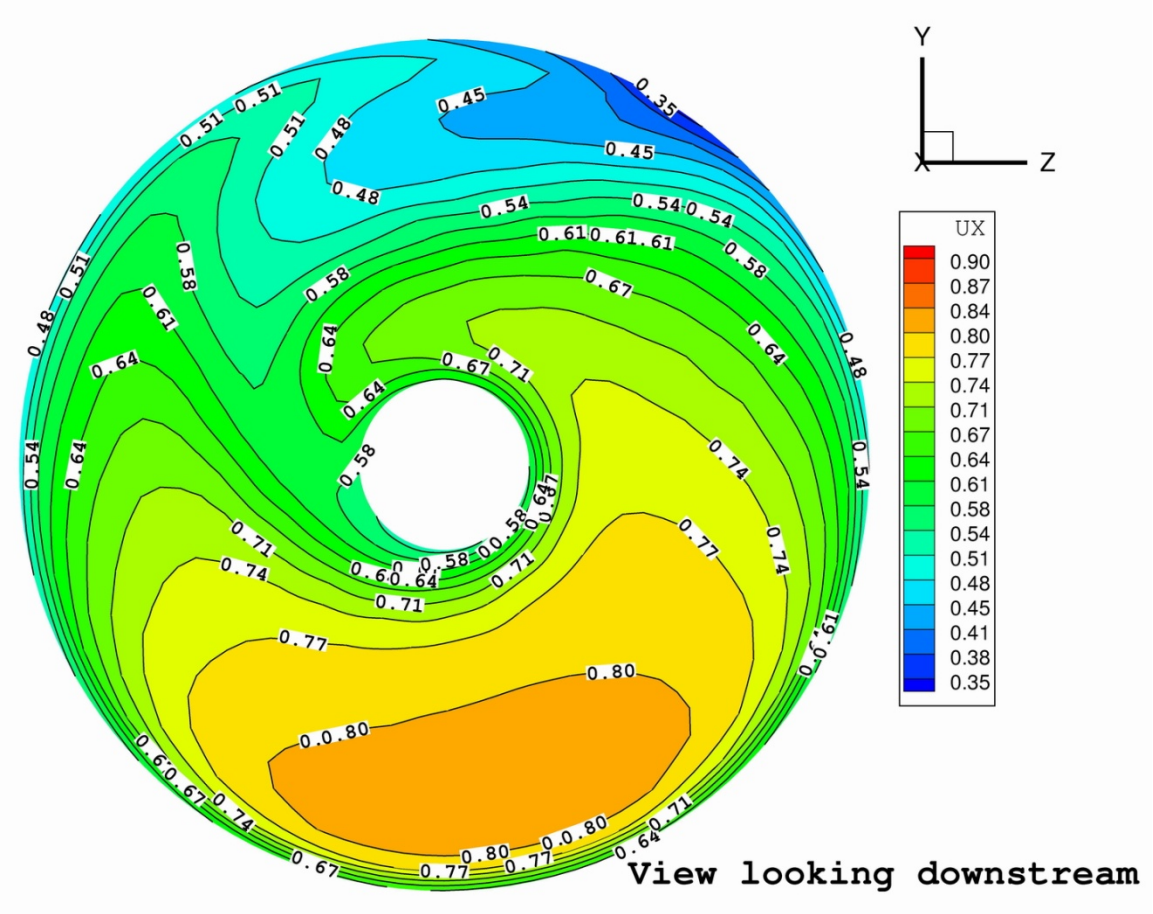

Figure 5.47: A non-uniform inflow upstream of the ONR AxWJ2 water-jet pump.

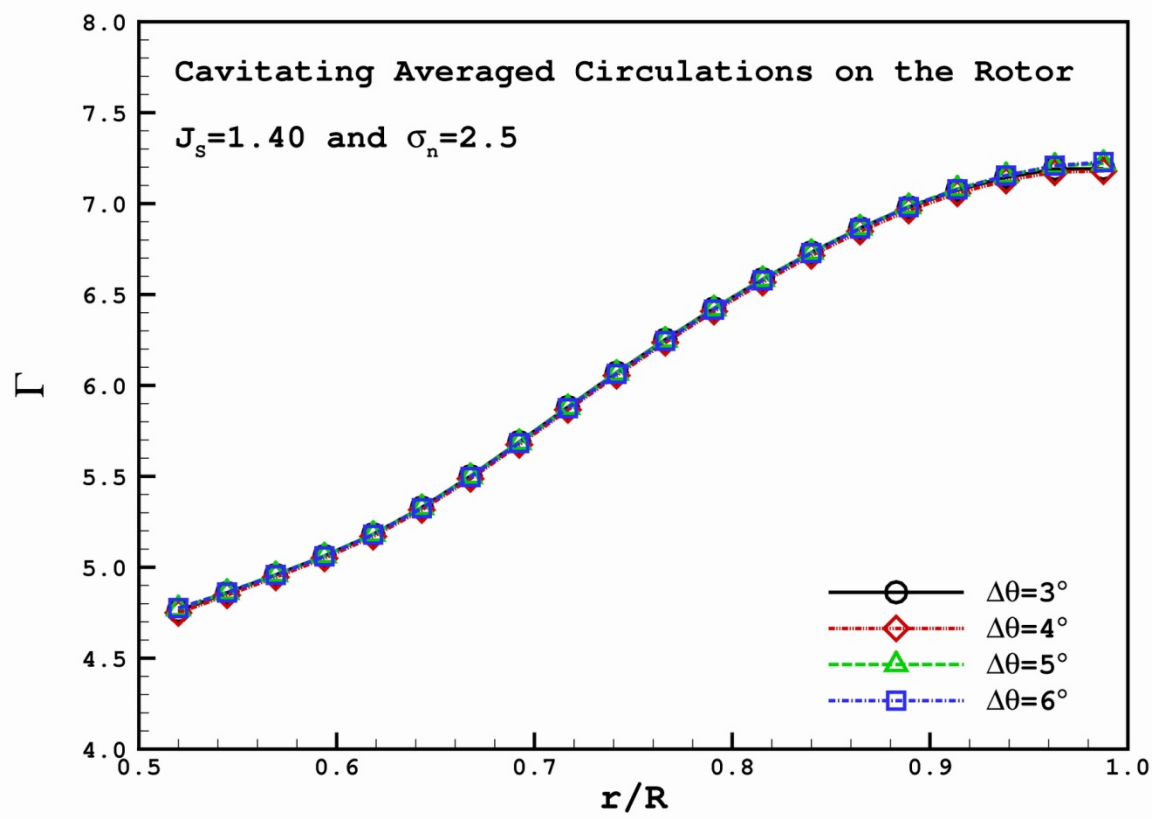

Figure 5.48: Convergence of cavitating averaged circulation distributions on the rotor of the ONR AxWJ2 water-jet with different time step sizes. J_S=1.40, σ_n=2.50 and *Fr*=16.916. Number of panels in the circumferential direction is 20. *NN*×*MM* on the blade is 60×20 and wake length is 4.50.

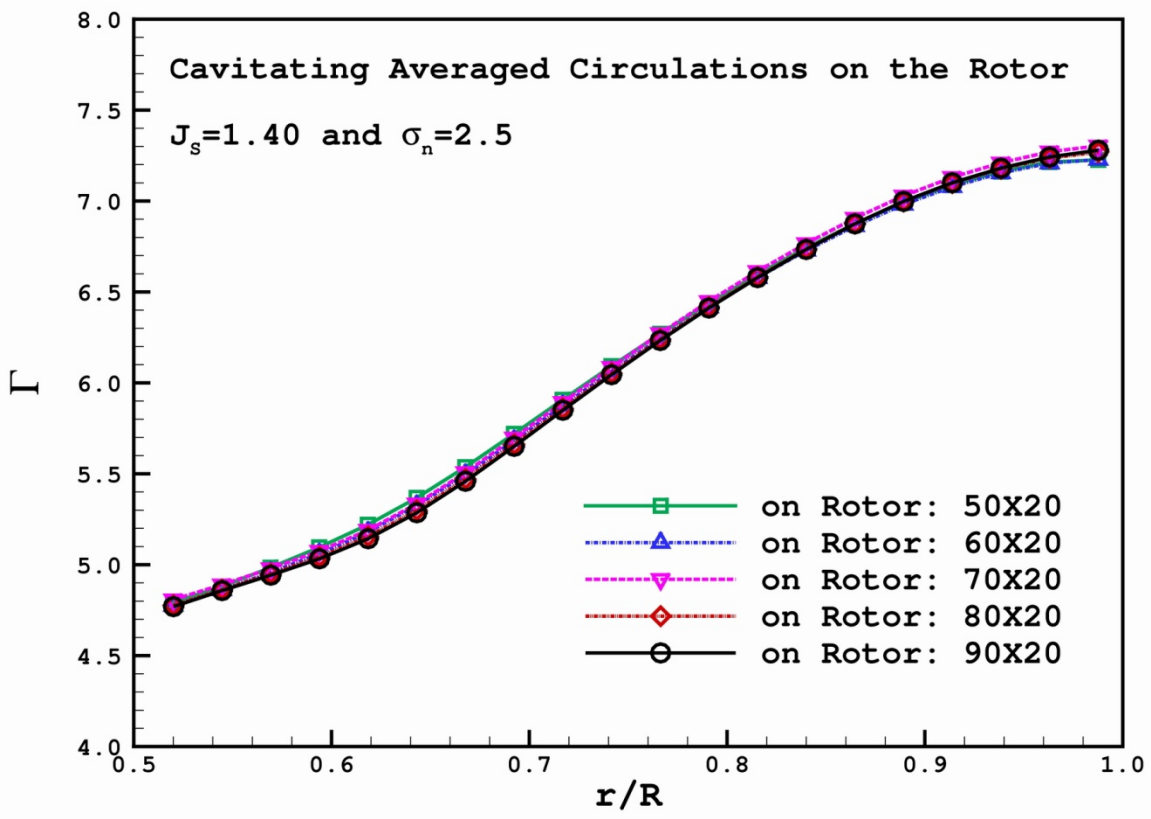

Figure 5.49: Convergence of cavitating averaged circulation distributions on the rotor of the ONR AxWJ2 water-jet with different number of panels in the chord-wise direction of the blade. J_S=1.40, σ_n=2.50 and Fr=16.916. Number of panels in the circumferential direction is 20. $\Delta\theta$=6° and wake length is 4.50.

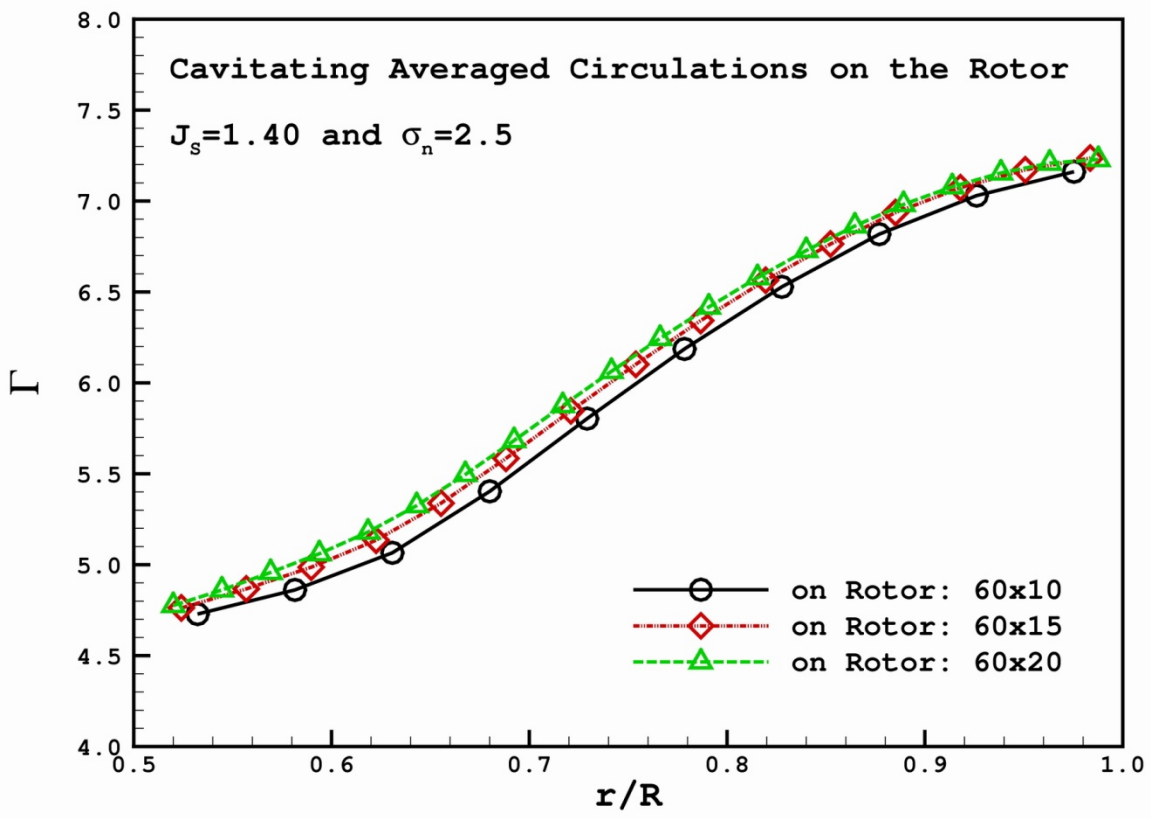

Figure 5.50: Convergence of cavitating averaged circulation distributions on the rotor of the ONR AxWJ2 water-jet with different number of panels in the span-wise direction of the blade. J_S=1.40, σ_n=2.50 and Fr=16.916. Number of panels in the circumferential direction is 20. $\Delta\theta$=6° and wake length is 4.50.

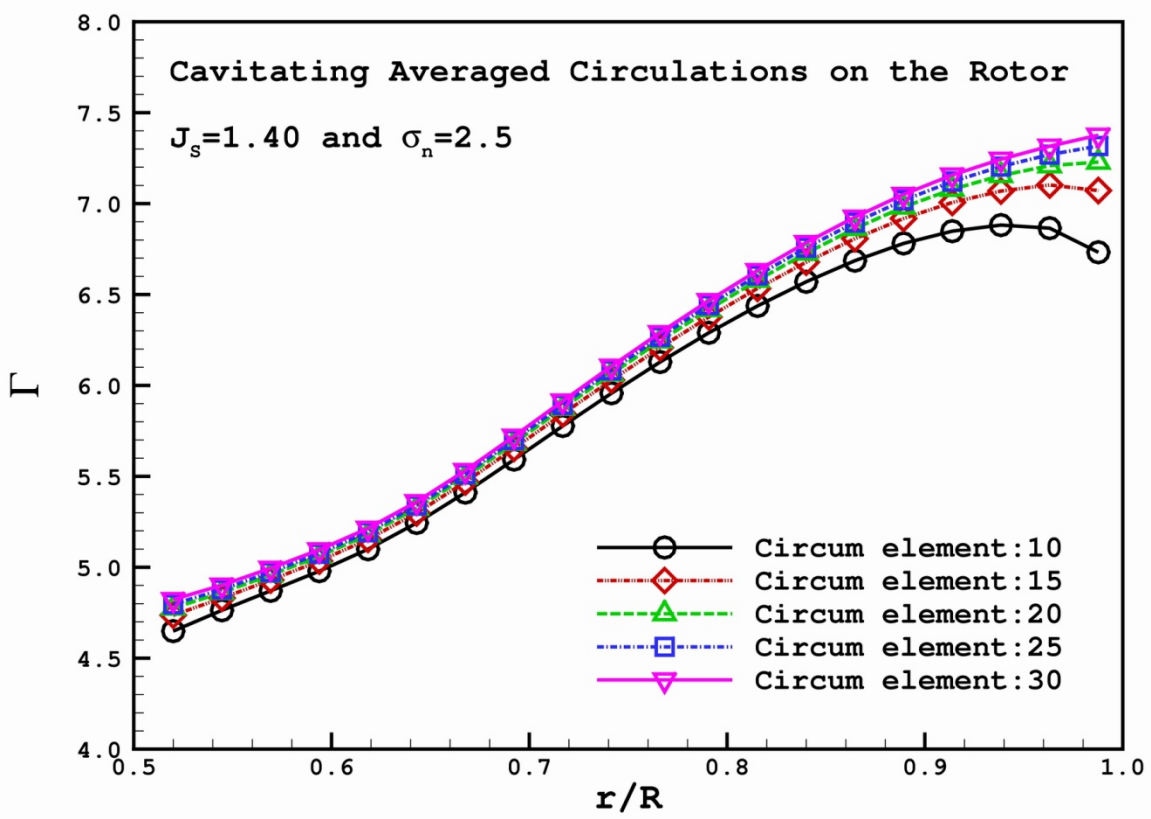

Figure 5.51: Convergence of cavitating averaged circulation distributions on the rotor of the ONR AxWJ2 water-jet with different number of panels in the circumferential direction between two blades. J_S=1.40, σ_n=2.50 and Fr=16.916. $NN \times MM$ on the blade is 60×20. $\Delta\theta$=6° and wake length is 4.50.

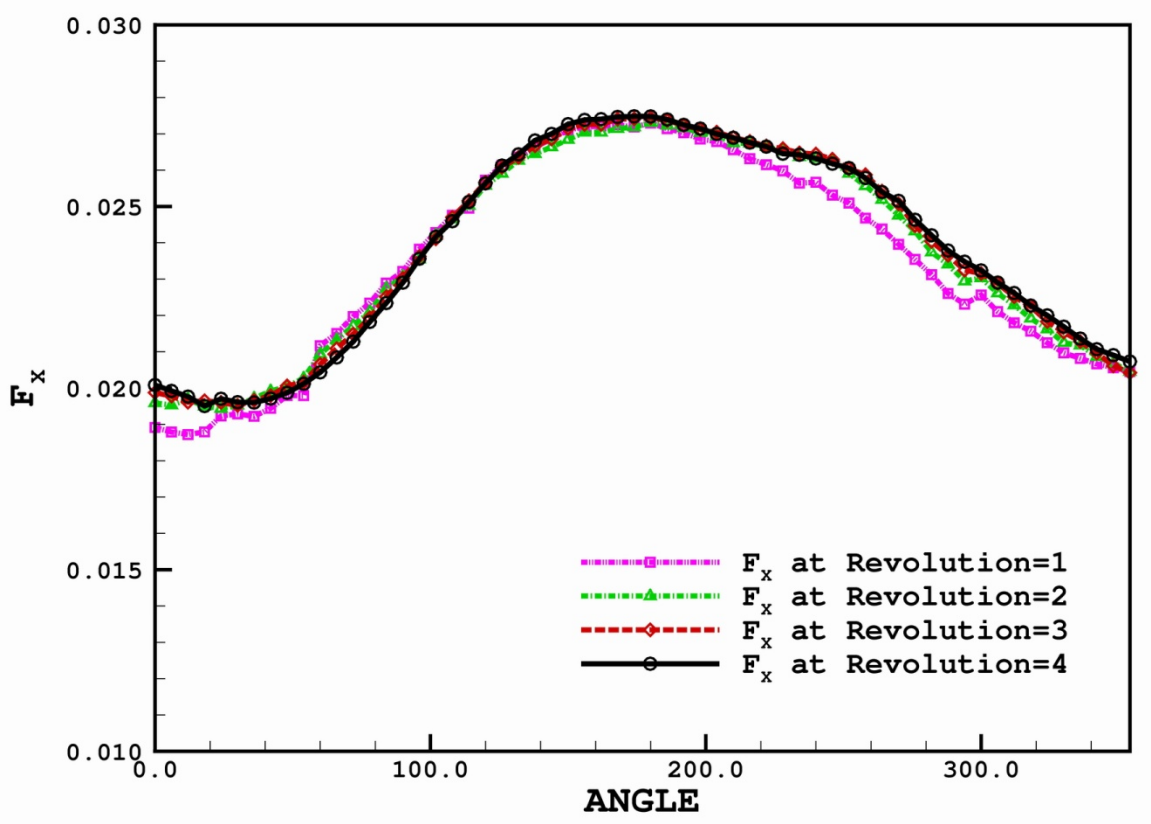

Figure 5.52: Convergence of the key rotor blade cavitating axial forces with number of revolutions. J_S=1.40, σ_n=2.50 and *Fr*=16.916. Number of panels in the circumferential direction is 20. *NN*×*MM* on the blade is 60×20. $\Delta\theta$=6° and wake length is 4.50.

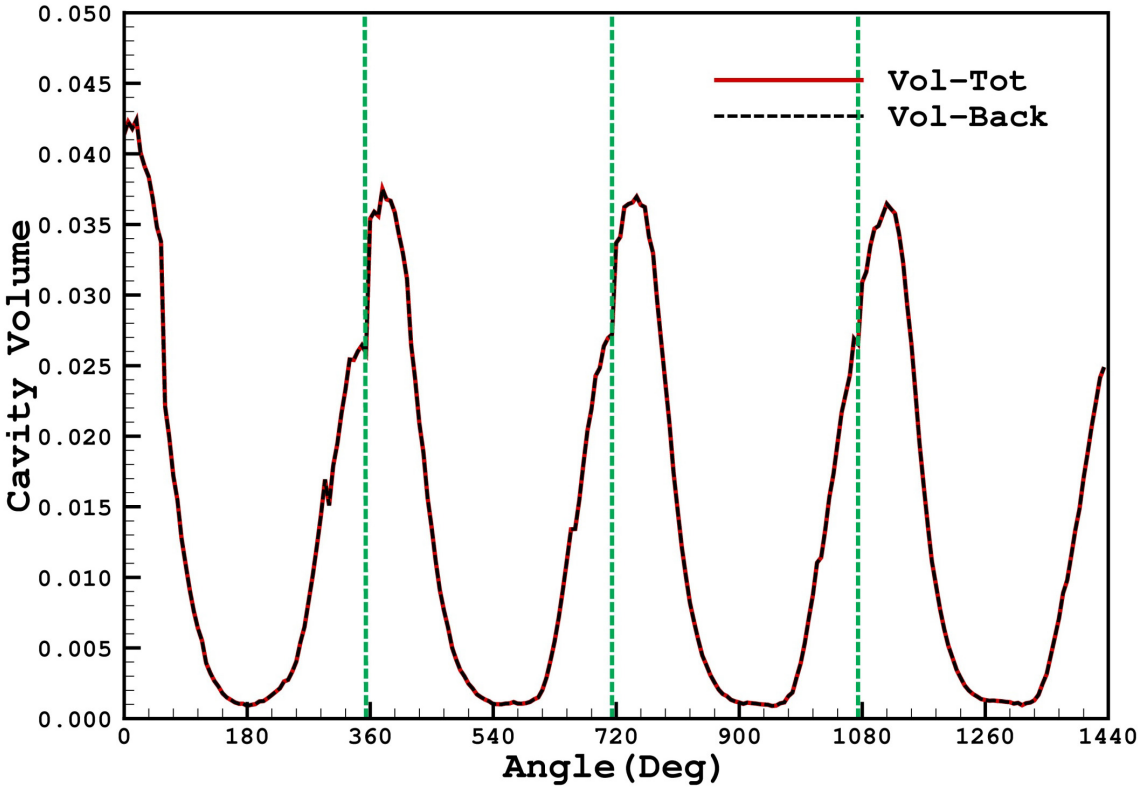

Figure 5.53: Variation of cavity volume on the rotor blade of the ONR AxWJ2 water-jet with blade angle. J_S=1.40, σ_n=2.50 and *Fr*=16.916. Number of panels in the circumferential direction is 20. *NN*×*MM* on the blade is 60×20. $\Delta\theta$=6° and wake length is 4.50.

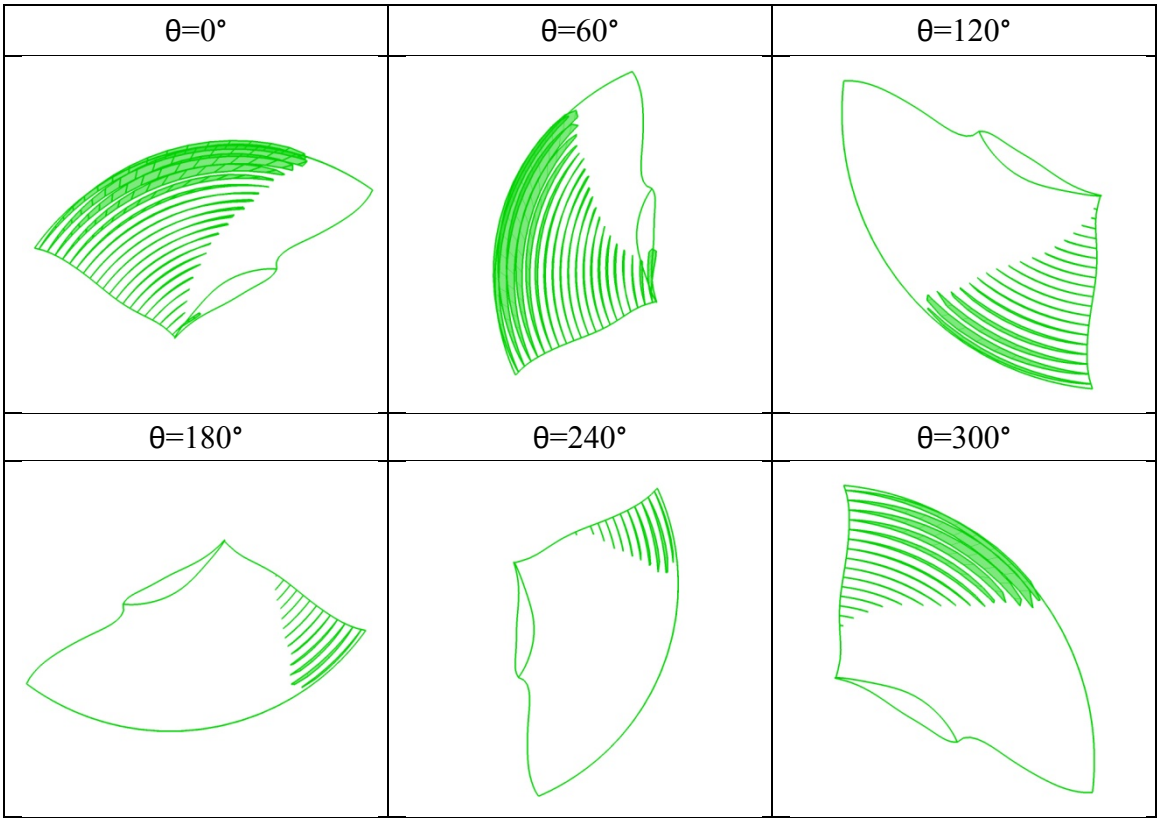

Figure 5.54: Cavity patterns on the rotor blade of the ONR AxWJ2 water-jet at different blade angles. J_S=1.40, σ_n=2.50 and Fr=16.916. Number of panels in the circumferential direction is 20. $NN \times MM$ on the blade is 60×20. $\Delta\theta$=6° and wake length is 4.50.

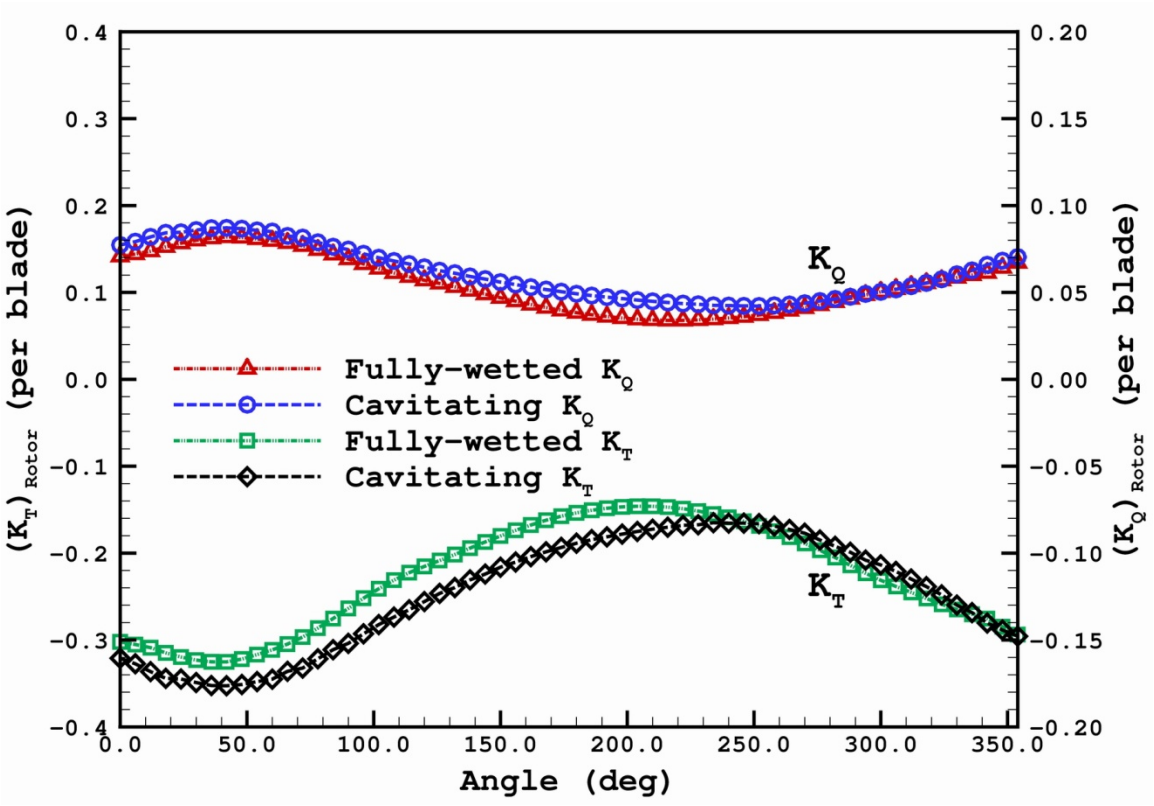

Figure 5.55: Comparison of thrust and torque coefficients (per blade) of the ONR AxWJ2 water-jet versus blade angle. J_S=1.40, σ_n=2.50 and Fr=16.916. Number of panels in the circumferential direction is 20. $NN \times MM$ on the blade is 60×20. $\Delta\theta$=6° and wake length is 4.50.

5.8 SUMMARY

A potential flow solver based on the panel method has been improved, refined and extended to analyze the hydrodynamic performance of a water-jet subject to uniform and non-uniform inflows. The interaction between the rotor and the stator was evaluated in an iterative manner via considering the circumferentially averaged effects (induced velocities) of one to the other. An Inviscid/Viscous hybrid scheme, using a potential flow solver and a RANS solver, has been used to evaluate the pressure rise on the casing surface in a water-jet pump. The predicted rotor torque (power coefficient) is in very good agreement with the results of experimental measurement, and the error is less than 2.0%. The predicted cavity patterns have somewhat larger extent than those from the observations. The predicted pressures (rotor only and rotor/stator) by the hybrid scheme on the casing surface are in good agreement with those predicted by FLUENT. The predicted thrust and torque breakdown of the rotor due to lower values of cavitation coefficients agree well with those measured. The tip gap model has been included in the present method. The effects of the gap size as well as different discharge coefficients (C_Q) were studied and the pressure distribution of the rotor at a constant radius (r/R=0.99) which is close to the tip were also compared with those calculated by FLUENT simulation. By applying full wake alignment, the rotor power coefficients can be enhanced 0.9~1.8% higher than those predicted by using pitch alignment. The present method is applied to analyze the unsteady cavitating flow inside a water-jet pump. The unsteady results show convergence and appear to be reasonable. However, due to the lack of experiments, they have not been validated with measurements or observations.

Chapter 6: Conclusions and Recommendations

6.1 CONCLUSIONS

In this dissertation, a robust, accurate and efficient numerical method based on the potential flow theory has been improved, refined and extended to analyze the hydrodynamic performance of a water-jet subject to uniform inflow for steady simulations. An Inviscid/Viscous hybrid scheme, using a potential flow solver (the present method) and a RANS solver (FLUENT), has been utilized to evaluate the pressure rise on the casing surface inside the water-jet pump. The thrust breakdown due to super cavitation has been successfully simulated by the present approach.

The main contributions of this research are:

- *Development of an effective method to predict the hydrodynamic performance of a water-jet pump*: A low order potential based panel method has been developed and improved considerably to simulate the water-jet problem. The potential flow inside a casing around rotor (or stator) blades and a hub is solved simultaneously in order to take the interaction of all geometries into account. The integral equation and boundary conditions for the water-jet are formulated and solved by distributing constant dipoles and sources on blades, hub and casing surfaces, and constant dipoles on the trailing wake sheets behind the rotor (or stator) blades. Systematic convergence studies were conducted in the cases of rotor only problem, stator only problem and rotor induced swirl velocities on the stator blade. For the rotor only calculation, the predicted power coefficient (P^*) had good agreement with experimental data. The model predicted a somewhat larger extent of cavitation coverage on the rotor than what was observed in the experiments. The interaction between the rotor and the stator is accounted for in an iterative manner by considering the circumferentially averaged induced velocities on the control points from one to

the other. The interaction between the rotor and stator converged quickly with iterations between the rotor and stator. The predicted power coefficient (P^*) on the rotor was improved with the stator effect being included. The effect of the stator on the rotor performance was found to be minor. The tip gap model has been included in the present method to take into account the tip clearance effect. The effects of the gap size as well as different discharge coefficients (C_Q) were studied. The pressure distribution of the rotor at a constant radius (r/R=0.99) which is very close to the tip was also compared with those calculated by the FLUENT simulation. The steady wake alignment has been implemented in the present method to include all of the component influences on the rotor trailing wake and to substitute the original pitch alignment.

- *Prediction of the pressure rise in the water-jet pump*: An Inviscid/Viscous hybrid scheme, using potential flow solver (PROPCAV-WJ) and RANS (FLUENT), has been used to evaluate the pressure head rise on the casing surface in the water-jet pump. The predicted results by the present method had fairly good agreements with those calculated by the RANS solver in both rotor-only and rotor/stator simulations. It was found that the coupling method requires much less computational time than the RANS solver.
- *Prediction of thrust/torque breakdown due to super cavitation on the rotor blade*: The present numerical scheme has been successfully improved and extended to predict super cavities on the rotor blade. The predicted performance due to cavitation breakdown has good correlations with the experimental measurements. It should also be noted that the steady cavitating simulation of the rotor only problem by the present method took much less computational time with only a single CPU than that by the RANS solver to simulate the cavitating flow inside the water-jet pump.

6.2 RECOMMENDATIONS FOR FUTURE WORK

The results predicted by PROPCAV-WJ had fairly good agreements with those simulated by FLUENT or those measured and observed in the experiments, which confirms the validity and robustness of the present method. Additional research may be included to improve the current numerical scheme as follows:

- *Handling blunt trailing edge geometries*: The actual rotor and stator geometries have blunt trailing edge. Although predicted pressures agree well with those predicted by RANS for the major portion at each section of the blade, the same shape of the blunt trailing edge geometry is still necessary for PROPCAV-WJ. The method of Pan and Kinnas (2011) and improved by Yu (UT-OE, MS 2012; Kinnas et al. 2012b) to include the 3-D geometry effect when coupling with XFOIL, which uses a viscous/inviscid interaction approach with an iterative scheme to find a non-lifting closing extension behind the finite trailing edge, can be applied in the present method to predict flow around blade sections with blunt trailing edges.
- *Extending the tip gap model in the cavitating calculation*: The tip clearance effect has been implemented in the present method for the fully-wetted calculation. The more appropriate C_Q can be determined either from the calculation of the 3-D RANS solver or from the experiments at John Hopkins University. By applying the tip gap model, the rotor loading close to the tip region should be more appropriate than that calculated by using the sealed gap geometry. Moreover, by extending the current tip gap model to the cavitating simulation, the prediction of the cavitating performance including the thrust breakdown can be improved.
- *Including the viscosity effects on the cavitation*: The viscosity effects can be included in the present method to improve the super cavitation model of the rotor and stator blades via the approach of Sun and Kinnas (2006). By updating the boundary

layer sources in the modified Green's formulation equation, the viscosity effect can be taken into account on the cavity of the blade. The iterative procedure continues until the viscous cavity shape converges.

- *Validating the current method in unsteady simulations*: The present method shows the capability of predicting the unsteady performance of a water-jet pump subject to a non-uniform inflow. Systematic correlations of the detailed measurements on the ONR-AxWJ2 water-jet with respect to the unsteady state are suggested for the validation of the present model. Analyses of unsteady fully-wetted and cavitating water-jets, such as in the case of non-axisymmetric inflows, can also be simulated by evaluating the 3-D (time-averaged or unsteady) effective inflow to the rotor or stator. By applying the hybrid coupling scheme (a potential flow solve coupling with a RANS solver), which solves for the global flow inside a water-jet pump including the influences of all the components, the effective inflows to the impeller or stator are able to be determined.
- *Considering unsteady rotor/stator interaction*: The method developed by He (UT-OE, PhD 2010) for the unsteady propeller/rudder interaction can be used to simulate the unsteady rotor/stator interaction in water-jet pumps.

Appendices

Appendix A

Iterative Pressure Kutta Condition (IPK)

This appendix summarized the iterative pressure Kutta condition (IPK) for the sake of completeness. Details of the description can be found in Kinnas and Hsin (1992).

The Green's formulation for the perturbation potentials on the propeller blades and wake surfaces is discretized as following:

$$[A][\phi] = [RHS] - [\Gamma][W] \tag{A.1}$$

where $[A]$ is the matrix of dipole influence coefficients, $[RHS]$ is the matrix of constant source distributions and $[W]$ is the matrix of dipole induced influence coefficients at control points on the blade surfaces by the wake sheets.

The Kutta condition requires that the velocity to be finite at the blade trailing edge. It can be satisfied by making the pressure difference at the upper and lower faces to be zero:

$$\Delta p_m = p_m^{upper} - p_m^{lower} = 0 \text{ for m=1,2,...,M} \tag{A.2}$$

where M is the total number of strips in the span-wise direction of the blade.

Due to the nonlinear dependence of Δp on ϕ, an iterative method is needed for solving the Equations (A.1) and (A.2) with respect to the unknowns $[\phi]$ and $[\Gamma]$. To determine the circulation Γ_m at m^{th} strip, the following Newton-Raphson scheme is applied:

$$[\Gamma]^{(k+1)} = [\Gamma]^{(k)} - \left[J^{(k)}\right]^{-1}[\Delta p]^{(k)} \tag{A.3}$$

Equation (A.1) at the k^{th} iteration can be written as:

$$[A][\phi]^{(k)} = [RHS] - [\Gamma]^{(k)}[W] \tag{A.4}$$

and the Jacobian matrix is defined as:

$$J_{i,j}^{(k)} = \frac{\partial \Delta p_i^{(k)}}{\partial \Gamma_j^{(k)}} \tag{A.5}$$

The solutions (ϕ and Γ) for the initial iteration (k=0) are determined by applying the Morino's Kutta condition (Morino and Kuo 1974) by the following system of equations:

$$\begin{aligned} [A][\phi]^{(0)} &= [RHS] - [\Gamma]^{(0)}[W] \\ \Gamma_m &= \phi_m^{upper} - \phi_m^{lower},\ \text{m=1,2,...,M} \end{aligned} \tag{A.6}$$

Since the Jacobian values of Equation (A.5) do not change greatly with the number of iterations, they can be kept the same during the iterative process. As a result, the new Jacobian matrix can be expressed as:

$$J_{i,j}^{(k)} = J_{i,j} = \frac{\partial \Delta p_i}{\partial \Gamma_j} = \frac{\Delta p_i^{\alpha} - \Delta p_i^{0}}{\Delta \Gamma_i^{\alpha} - \Delta \Gamma_i^{0}} \tag{A.7}$$

where the superscript (0) corresponds to Equation (A.6) and the superscript (α) corresponds to the solution at the $(1+\alpha)^{th}$ iteration, and

$$\Gamma_j^{\alpha} = (1+\beta)\Gamma_j^{0} \tag{A.8}$$

where β is a small number. (β=0.01 is recommended.)

Using the new Jacobian matrix, the Equation (A.3) becomes:

$$[\Gamma]^{(k+1)} = [\Gamma]^{(k)} - [J]^{-1}[\Delta p]^{(k)} \tag{A.9}$$

The solutions can be determined iteratively by solving Equations (A.4) and (A.9). However, the method will be very computationally expensive for the unsteady problems because Equation (A.4) needs to be recalculated at each time step and iteration. Therefore, the base problem technique is applied. The [RHS] matrix remains the same at each time step. The following equation can be derived by subtracting Equation (A.4) from (A.1):

$$[A]\left[[\phi]^{(k)}-[\phi]\right]=-[W]\left[[\Gamma]^{(k)}-[\Gamma]\right] \tag{A.10}$$

or

$$[A][\delta\phi]=-[W][\delta\Gamma] \tag{A.11}$$

where

$$[\delta\phi]=[\phi]^{(k)}-[\phi] \text{ and } [\delta\Gamma]=[\Gamma]^{(k)}-[\Gamma] \tag{A.12}$$

Introduce the notation of "base potentials", $[\Phi]^m$, which corresponds to the solutions of the base problem:

$$[A][\Phi]^m=-[W][B]^m, \text{ m=1,2,...,M} \tag{A.13}$$

where

$$[B]^m=\left[B_1=0,\ B_2=0,.....,\ B_m=0,\ B_{m+1}=0,.....,\ B_M=0\right]^T \tag{A.14}$$

The base potentials correspond to the potentials of the blade when there is no inflow and the potential jumps are equal to zero in all but the first wake panel in each strip. The dipole distribution for the first wake panel in each strip is "1" at the blade trailing edge and decreases linearly to "0" at the right panel edge. It should be noted that the base potentials depend only on the discretization and are independent of the inflow and time step. As a result, the solution of Equation (A.11) can be expressed as a linear superposition of base potentials:

$$[\delta\phi]=\sum_{m=1}^{M}\delta\Gamma_m[\Phi]^m \tag{A.15}$$

By the definition of [δϕ] and [δΓ], the solution to the system of equations can be written as:

$$[\phi]^{(k)}=[\phi]+\sum_{m=1}^{M}\left(\Gamma_m^{(k)}-\Gamma_m\right)[\Phi]^m \tag{A.16}$$

Once the base potentials are determined, the potentials which satisfy the Kutta condition can be calculated by solving Equations (A.16) and (A.9) by using the solutions from Equation (A.6).

Application to the Cavitating Problem

The system of the equations for the cavitating problem (partial or super cavitation) is different from that of fully-wetted problem. The unknowns for the cavitating problem are potentials on the blade and normal velocities on the cavity. Therefore, the IPK cannot be utilized directly to the system of the equations. For the cavitating problem, The IPK is applied as a *post process*. Once the problem has been solved, the potentials on the wetted surface are known and the potentials on the cavity surface can be determined via the dynamic boundary condition. Following the calculation of the potentials, the base problem is solved first to obtain the base potentials. The potentials on the cavity and blade surfaces which satisfy the Kutta condition can be achieved by solving Equations (A.9) and (A.16) iteratively.

Appendix B

FLUENT Run Specifics

This appendix describes detailed numerical settings of the 2-D axisymmetric and 3-D rotor only and rotor/stator FLUENT calculations.

2-D Axisymmetric Simulation

The FLUENT 2-D axisymmetric run has a domain from x/R=-3.0 to 6.034 and contains 11,232 cells. The turbulence model used in this simulation is k-ω SST model. The range of y^+ on the hub wall is from 50 to 200 and that on the casing is from 60 to 180. H-refinement is applied near the walls of hub and casing. The solution methods in the simulation are SIMPLEC scheme for pressure-velocity coupling. Green-Gauss cell based gradient, standard pressure and QUICK schemes are used for the special discretization. The run takes 2 minutes with 1 CPU (2.43 GHZ quad-core 64-bit Intel Xeon processor) to complete 1,000 iterations. The 2-D computational domain, meshes and boundaries are shown in Figure B.1.

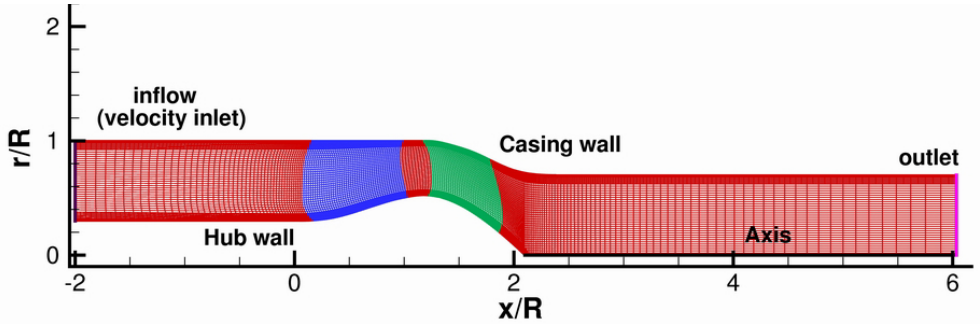

Figure B.1: 2-D axisymmetric computational domain, meshes and boundaries of the ONR AxWJ2 water-jet.

3-D Rotor Only Simulation

The FLUENT 3-D rotor only run (created by Mr. Ye Tian in OE Group at UT-Austin) with periodic boundaries has a domain from x/R=-4.0 to 5.867 and contains 3,072,564 cells. The turbulence model used in this simulation is k-ω SST model. The range of y^+ on the hub wall is from 50 to 450 and that on the casing is from 40 to 180. The solution methods in the simulation are SIMPLEC scheme for pressure-velocity coupling. Least squares cell based gradient, standard pressure and QUICK schemes are used for the special discretization. The run takes 28 hours with 32 CPUs (2.43 GHZ quad-core 64-bit Intel Xeon processor) to complete 20,000 iterations. The 3-D computational domain, meshes and boundaries for rotor-only simulation are shown in Figure B.2. The range of y^+ on the rotor tip in the gap region is from 10 to 35 and that on the casing surface in the gap zone is from 5 to 15. The Grids in the tip gap region are shown in Figure B.3.

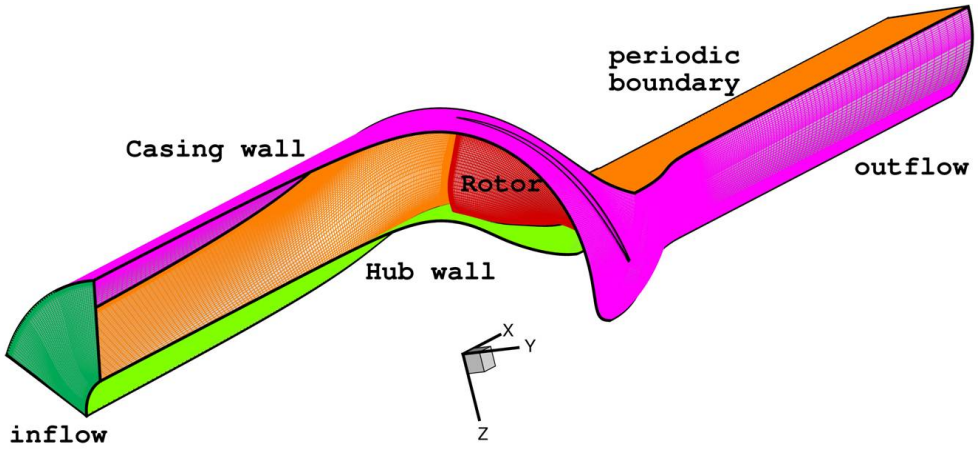

Figure B.2: 3-D computational domain, meshes and boundaries for rotor-only simulation of the ONR AxWJ2 water-jet.

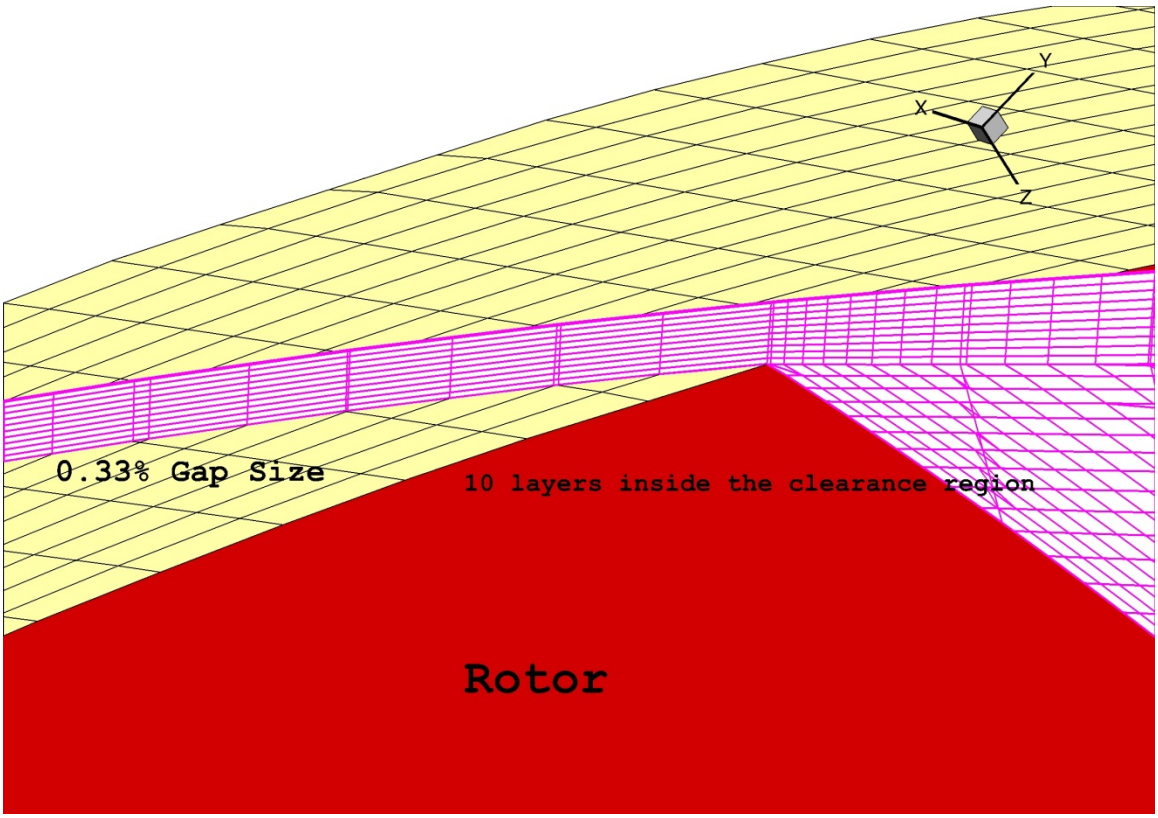

Figure B.3: Grids (10 layers) in the tip gap region for rotor-only simulation of the ONR AxWJ2 water-jet.

3-D Rotor/Stator Simulation

The FLUENT 3-D rotor/stator run (case file provided by Mr. Seth Schroeder at NSWCCD and rescaled by the author) with periodic boundaries has a domain from x/R=-4.0 to 5.867 and contains 4,538,440 cells. A mixing plane is utilized for the interaction between the rotor and stator. The turbulence model used in this simulation is Realizable k-ε model with standard wall functions. The range of y^+ on the hub wall is from 80 to 400 and that on the casing is from 100 to 250. The solution methods in the simulation are SIMPLEC scheme for pressure-velocity coupling. Green-Gauss node based gradient, PRESTO and second order upwind schemes are used for the special discretization. The run takes 33 hours with 32 CPUs (2.43 GHZ quad-core 64-bit Intel Xeon processor) to complete 20,000 iterations. The 3-D computational domain, meshes and boundaries for rotor/stator simulation are shown in Figure B.3. The comparison of the three simulations can be found in Table B.1.

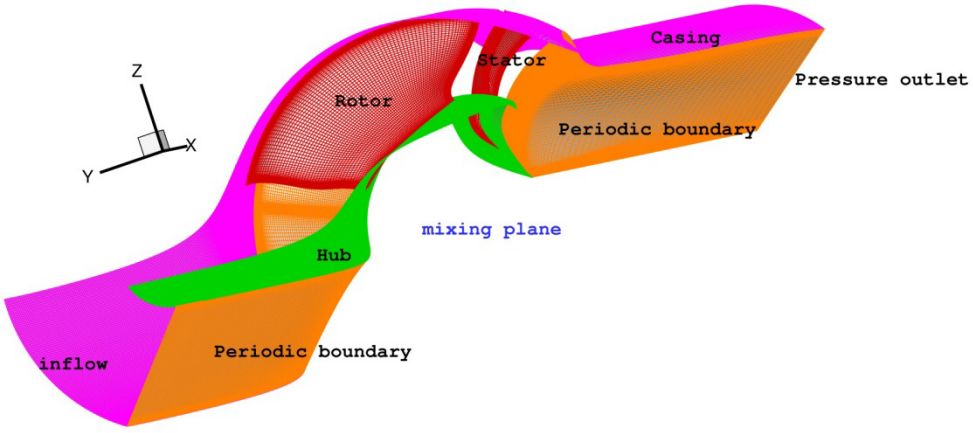

Figure B.4: 3-D computational domain, meshes and boundaries for rotor-only simulation of the ONR AxWJ2 water-jet.

	No. of Cells	Computational Time	Turbulence Model	CPU
PROPCAV/FLUENT (2-D Axisymmetric)	11,232	PROPCAV: 2 minutes (fully-wetted) RANS: 2 minutes	k-ω SST	1
FLUENT (3-D) Rotor only	3,072,564	28 hours	k-ω SST	32
FLUENT (3-D) Rotor/Stator	4,538,440	33 hours	Realizable k-ε	32

Table B.1: Comparison of Inviscid/Viscous hybrid scheme and FLUENT simulations.

Appendix C

Correction of Kutta Condition in the System of the Equations

This appendix describes the corrections to the implementation of Kutta condition in the system. The Final system of equations, including the influence of the split panels can be found in (Fine 1992) for more detailed descriptions. The modified parts are shown as follows:

On the cavitating blade

$$\sum_{m=1}^{M}\left\{\begin{array}{l}\sum_{n=1}^{N_{LE}} A_{inm}\phi_{nm} + \sum_{n=N_{LE}+N_{CAV_m}+1}^{N} A_{inm}\phi_{nm} + \\ \left[R_{1m}\phi_{1m} + R_{2m}\phi_{2m} + R_{3m}\phi_{3m}\right]\xi_{im} + \phi_{Rm}A_{imn_{spm}}F_{Rm} - \\ \sum_{n=N_{LE}+1}^{N_{LE}+N_{CAV_m}} B_{inm}\dfrac{\partial\phi}{\partial n}_{nm} - \dfrac{\partial\phi}{\partial n}_{Lm} B_{imn_{spm}}F_{Lm} - \\ \sum_{l=1}^{N_{Cm}} C_{ilm}Q_{lm} - Q_{Lm}C_{imn_{spm}}F_{Lm} + W_{i1m}\left[\phi_{Nm} - \phi_{1m}\right]\end{array}\right\} \tag{C.1}$$
$$= RHS_{split\ \text{panel on the blade}} + RHS_{S_{CBi}}$$

In the Equation (C.1), the original $(1 - SOP_m)\,\phi_{Nm}$ term has been modified to ϕ_{Nm}.

In the cavitating wake

$$\sum_{m=1}^{M}\left\{\begin{array}{l}\sum_{n=1}^{N_{LE}} D_{inm}\phi_{nm} + \sum_{n=N_{LE}+N_{CAV_m}+1}^{N} D_{inm}\phi_{nm} + \\ \left[R_{1m}\phi_{1m} + R_{2m}\phi_{2m} + R_{3m}\phi_{3m}\right]\xi_{im} + \phi_{Rm}D_{imn_{spm}}F_{Rm} - \\ \sum_{n=N_{LE}+1}^{N_{LE}+N_{CAV_m}} E_{inm}\dfrac{\partial\phi}{\partial n}_{nm} - \dfrac{\partial\phi}{\partial n}_{Lm} E_{imn_{spm}}F_{Lm} - \\ \sum_{l=1}^{N_{Cm}} F_{ilm}Q_{lm} - Q_{Lm}F_{imn_{spm}}F_{Lm} + W_{i1m}\left[\phi_{Nm} - \phi_{1m}\right]\end{array}\right\} \tag{C.2}$$
$$= RHS_{split\ \text{panel in the wake}} + RHS_{S_{CWi}}$$

In the Equation (C.2), the original $(1 - SOP_m)\ \phi_{Nm}$ term has been modified to ϕ_{Nm}.

The velocities at the trailing edge on the face side of the rotor blade when super-cavitation occurs before and after the modification are shown in Figures C.1 and C.2, respectively. The pressures at a certain section before and after correction are presented in Figure C.3 and Figure C.4. After the modification, the predicted velocities and pressures by the present method give more reasonable results.

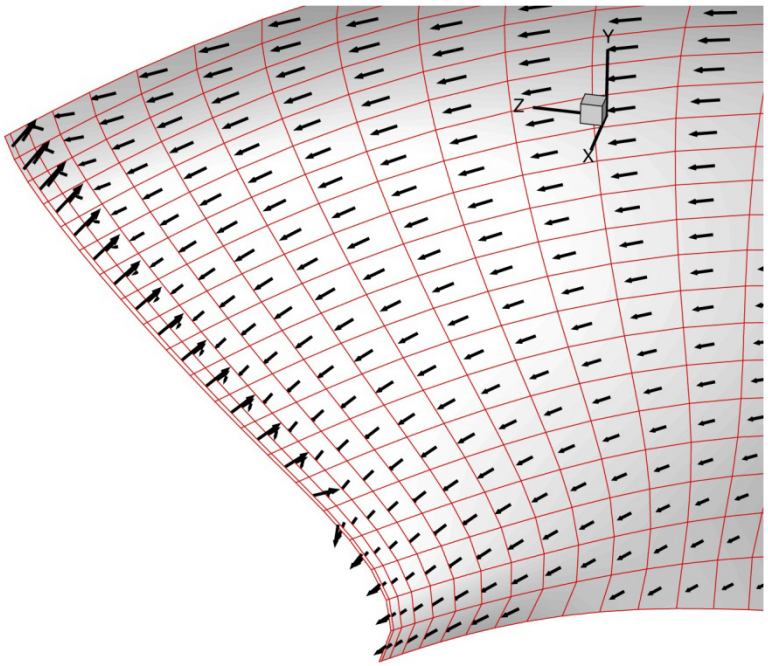

Figure C.1: Velocities at the trailing edge on the face side of the ONR AxWJ2 water-jet rotor blade before the correction of the Kutta condition. There are reversed flows at the blade trailing edge.

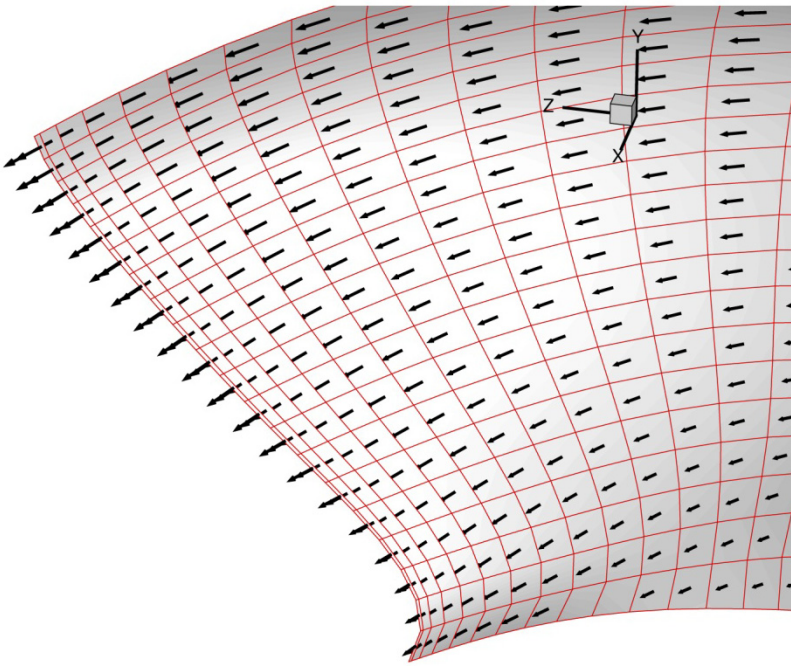

Figure C.2: Velocities at the trailing edge on the face side of the ONR AxWJ2 water-jet rotor blade after the correction of the Kutta condition. There are no reversed flows at the blade trailing edge.

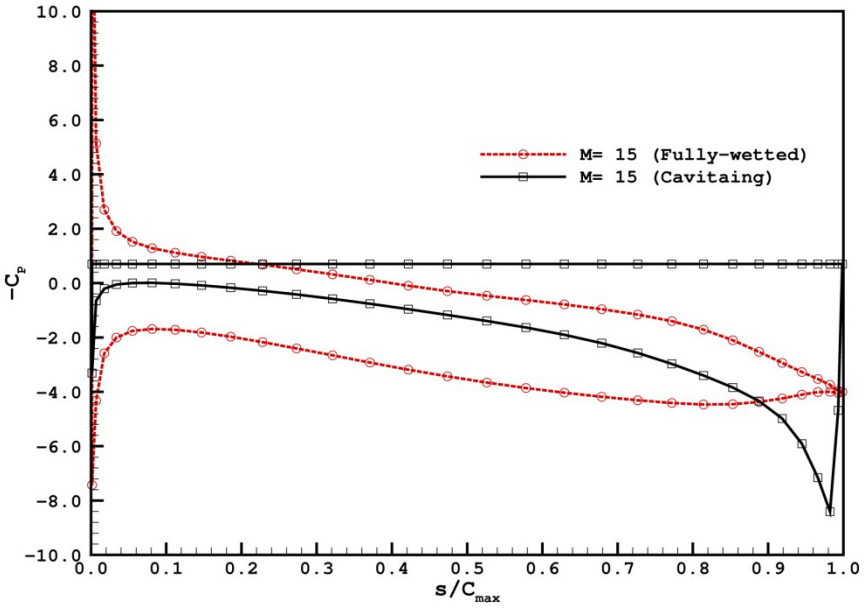

Figure C.3: Pressure distribution at a certain section on rotor blade of the ONR AxWJ2 water-jet before the correction of the Kutta condition.

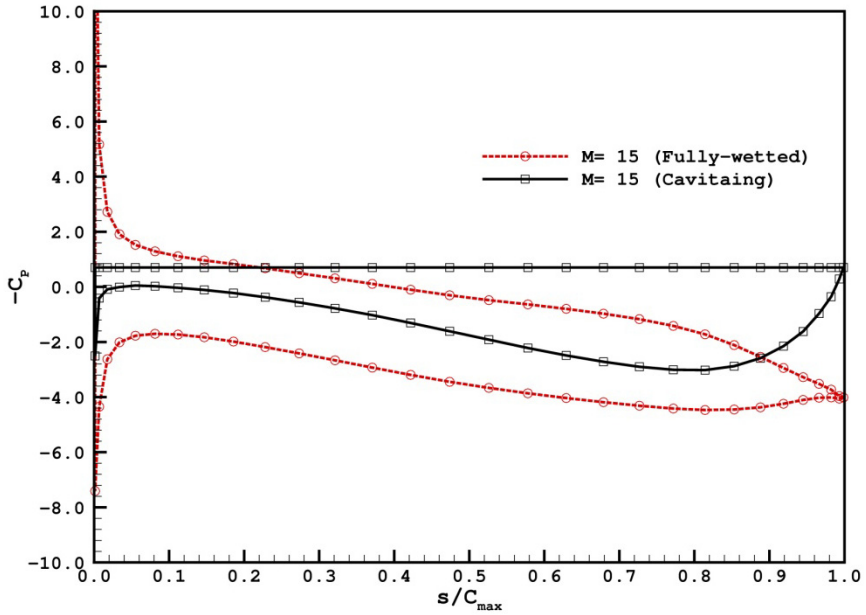

Figure C.4: Pressure distribution at a certain section on rotor blade of the ONR AxWJ2 water-jet after the correction of the Kutta condition.

Glossary

Latin Symbols

C_f	skin-friction coefficient, $C_f = \tau_{wall}/0.5\rho_e U_e^2$
C_P	pressure coefficient, $C_P = P - P_0/0.5\rho n^2 D^2$ for propellers
C_Q	discharge coefficient, $C_Q = Q_J\sqrt{\rho/2\Delta p}/h_{gap}$
C	chord length of blade sections
D	propeller diameter, $D=2R$
F_r	Froude number, $F_r=n^2D/g$
F_x	propeller axial forces
f_{max}/C	maximum camber to chord ratio
g	acceleration of gravity
G	Green's function
h	cavity thickness over the blade surface
h_{gap}	gap size
h_w	cavity thickness over the wake surface
H^*	head coefficient
J_S	advance ratio based on V_S, $J_S=V_S/nD$
K_Q	torque coefficient, $K_Q = Q/\rho n^2 D^5$
K_T	thrust coefficient, $K_T = T/\rho n^2 D^4$
l	cavity length
n	propeller rotational frequency (*rps*)
N^*	cavitation coefficient, $N^* = P_{t3} - P_v/\rho n^2 D^2$
P	pressure
P_0	pressure far upstream at propeller shaft
P_v	vapor pressure of water

P_{t3}	measured pressure at station 3 in ONR-AxWJ2 pump
P_{t6}	measured pressure at station 6 in ONR-AxWJ2 pump
P^*	power coefficient
$\vec{q}$	total velocity
$\overrightarrow{q_t}$	total cavity velocity
$\overrightarrow{q_{in}}$	local inflow velocity (in the propeller fixed system)
$\overrightarrow{q_w}$	wake inflow velocity (in the ship fixed system)
Q	propeller torque
Q_J	volumetric flow rate
Q^*	flow coefficient
R	propeller radius
Re	Reynolds number, $Re=U_{in}R/\nu$.
$\vec{s}, \vec{v}, \vec{n}$	non-orthogonal unit vectors in the grid local coordinates
S_C	cavitating surface, $S_C = S_{CB} + S_{CW}$
S_{HC}	wetted part of hub and casing surface
S_R	wetted part of the rotor blade
S_{RC}	cavitating part on the rotor blade
S_{RW}	rotor wake surface
S_{RWC}	cavitating part in the rotor wake
Ss	wetted part of the stator blade
S_{SC}	cavitating part on the stator blade
S_{SW}	stator wake surface
S_{SWC}	cavitating part in the stator wake
t	time
t_{max}/C	maximum thickness to chord ratio

T	propeller thrust
$u_{tan,SR}$	rotor induced swirl velocity on the stator blade
U_{in}	flow velocity at the inlet boundary
V_S	ship speed
(X, Y, Z)	propeller fixed coordinate
(X_s, Y_s, Z_s)	ship fixed coordinate

Greek Symbols

α	angle of attack
$\Delta\phi_{TE}$	potential jump at the trailing edge of the blade
$\Delta\phi_{W}$	potential jump across the trailing wake sheet of the blade
Δt	time step size
$\Delta\theta$	blade angle increment, $\Delta\theta=\omega\Delta t$
$\Delta\Omega_f$	volume swept by the cell boundary between two time steps
η	pump efficiency, $\eta=Q^*H^*/P^*$
Γ	non-dimensionalized circulation, $\Gamma=\Delta\phi_{TE}/2\pi R\sqrt{V_S^2+(0.7\pi nD)^2}$ for rotating propeller
Γ_s	non-dimensionalized circulation, $\Gamma_s=\Delta\phi_{TE}/2\pi RV_S$ for rudder or stator
ω	propeller angular velocity
ϕ	perturbation potential
Φ	total potential
ν	kinematic viscosity
ρ	fluid density
σ_n	cavitation number based on n, $\sigma_n = P_0 - P_v/0.5\rho n^2 D^2$

σ_v	cavitation number based on V_S, $\sigma_v = P_0 - P_v / 0.5\rho V_S^2$

Other Symbols

$+$	upper wake surface, cavity or separation region
$-$	lower wake surface, cavity or separation region

Acronyms

2-D	Two dimensional
3-D	Three dimensional
BEM	Boundary Element Method
CFD	Computational Fluid Dynamics
CPU	Central Processing Unit
ITTC	International Towing Tank Conference
LCC	Large Cavitation Channel
ONR	Office of Naval Research
NSWCCD	Naval Surface Warfare Center at Carderock Division
RANS	Reynolds Averaged Navier-Stokes (equations)
SIMPLEC	SIMPLE-Consistent algorithm (Semi-Implicit Method for Pressure-Linked Equations)
VII	Viscous/Inviscid Interaction

Computer Programs

ANSYS/FLUENT	commercial CFD software
ANSYS/GAMBIT	grid generator provided by ANSYS Company
XFOIL	two-dimensional integral boundary layer analysis code

References

Brewton, S., Gowing, S., and Gorski, J. (2006). "Performance Predictions of a Waterjet Rotor and Rotor/Stator Combination Using RANS Calculations." Proc. 26th Symposium on Naval Hydrodynamics, Rome, Italy.

Brockett, T. (1966). "Minimum Pressure Envelopes for Modified NACA66 Sections with NACA a=0.8 Camber and Buships Type I and Type II Sections." Technical Report 1780, DTNSRDC Report.

Chesnakas, C. J., Donnelly, M. J., Pfitsch, D. W., Becnel, A. J., and Schroeder, S. D. (2009). "Performance Evaluation of the ONR Axial Waterjet 2 (AxWJ-2)." NSWCCD-50-TR-2009/089, Naval Surface Warfare Center, West Bethesda, Maryland.

Chun, H. H., Park, W. G., and Jun, J. G. (2002). "Experimental and CFD Analysis for Rotor-Stator Interaction of a Water-jet Pump." Proc. 24th Symposium on Naval Hydrodynamics, Fukuoka, Japan.

Drela, M. (1989). "XFOIL: An analysis and design system for low Reynolds number airfoils." In Lecture Notes in Engineering (Vol. 54, Low Reynolds Number Aerodynamics), New York. Springer-Verlag.

Fine, N. E. (1992). "Nonlinear Analysis of Cavitating Propellers in Nonuniform Flow." PhD thesis, Department of Ocean Engineering, Massachusetts Institute of Technology.

Fine, N. E., and Kinnas, S. A. (1993). "A Boundary-Element Method for the Analysis of the Flow around 3-D Cavitating Hydrofoils." Journal of Ship Research, 37(3), 213-224.

Gaggero, S. and Brizzolara, S. (2008) "A Potential Panel Method for the Prediction of Mid-chord Face and Back Cavitation." 6th International Conference on High Performance Marine Vehicles, 1, 33-46.

Gaggero, S., Luca, S., Brizzolara, S., Michele, V., Marco, F., and Francesco, C. (2009). "Comparison of experimental measurements and numerical calculations for a propeller in axial cylinder." Proc. of 1st International Symposium on Marine Propulsors, Trondheim, Norway, 525-536.

Gu, H. (2006). "Numerical Modeling of Flow around Ducted Propellers (UT-OE Report 06-1)." PhD Thesis, Ocean Engineering Group, Department of Civil, Architectural, and Environmental Engineering, The University of Texas at Austin, Austin, TX.

Gupta, A. (2004). "Numerical Prediction of Flows around Podded Propulsors (UT-OE Report 04-6)." MS Thesis, Ocean Engineering Group, Department of Civil, Architectural, and Environmental Engineering, The University of Texas at Austin, Austin, TX.

He, L. (2010). "Numerical Simulation of Unsteady Rotor/Stator Interaction and Application to Propeller/Rudder Combination (UT-OE Report 10-5)." PhD Thesis, Ocean Engineering Group, Department of Civil, Architectural, and Environmental Engineering, The University of Texas at Austin, Austin, TX.

Hsin, C.-Y. (1990). "Development and Analysis of Panel Method for Propellers in Unsteady Flow." PhD Thesis, Department of Ocean Engineering, Massachusetts Institute of Technology.

Hughes, M. J. (1993). "Analysis of Multi-component Ducted Propulsors in Unsteady Flow." PhD Thesis, Department of Ocean Engineering, Massachusetts Institute of Technology.

Hughes, M. J. (1997). "Implementation of a Special Procedure for Modeling the Tip Clearance Flow in a Panel Method for Ducted Propulsors." Proc. Society of Naval Architects and Marine Engineers Propeller/Shafting '97 Symposium, Virginia Beach, VA.

ITTC (2008). "Final Report and Recommendations to the 25th ITTC, Specialist Committee on Cavitation." Proc. of 25th International Towing Tank Conference, Fukuoka, Japan, volume II, 473-533.

Kerwin, J. E., Kinnas, S. A., Lee, J. T., and Shih, W. Z. (1987). "A Surface Panel Method for the Hydrodynamic Analysis of Ducted Propellers." Trans. of SNAME '95, 93-122.

Kerwin, J. E., Taylor, T. E., Black, S. D., and McHugh, G. P. (1997). "A coupled lifting-surface analysis technique for marine propulsors in steady flow. " Proc. Society of Naval Architects & Marine Engineers Propellers/Shafting '97 Symposium, Virginia Beach, VA, United States.

Kerwin, J. E. (2006). "Hydrodynamic Issues in Water-jet Design and Analysis." Proc. 26th Symposium on Naval Hydrodynamics, Rome, Italy.

Kerwin, J. E., Michael, T. J., and Neely, S. K. (2006). "Improved Algorithms for the Design/Analysis of Multi-Component Complex Propulsors." Proc. Society of Naval Architects and Marine Engineers Propeller/Shafting '06 Symposium, Williamsburg, VA.

Kinnas, S. A. and Hsin, C.-Y. (1992). "A Boundary Element Method for the Analysis of the Unsteady Flow around Extreme Propeller Geometries."AIAA Journal, 30(3), 688-696.

Kinnas, S. A. and Fine, N. E. (1993). "A Numerical Nonlinear-Analysis of the Flow around 2-Dimensional and 3-Dimensional Partially Cavitating Hydrofoils." J. Fluid Mech., 254, 151-181.

Kinnas, S. A., Lee, H. S., Gu, H., and Gupta, A. (2004). "Prediction of Performance of Ducted and Podded Propellers." Proc. 25th Symposium on Naval Hydrodynamics, St. John's, Newfoundland and Labrador, Canada.

Kinnas, S. A., Lee, H. S., Mishra, B., He, L., Rhee, S.-H., and Balasubramanyam, S. (2006). "Hydrodynamic Analysis of Podded Propellers." Proc Propeller/Shafting '06 Symposium, Virginia Beach, VA.

Kinnas, S. A., Lee, H. S., Michael, T. J., and Sun, H. (2007a). "Prediction of Cavitating Water-jet Propulsor Performance Using a Boundary Element Method." Proc. 9th Int. Conf. on Numerical Ship Hydrodynamics, Ann Arbor, Michigan.

Kinnas, S. A., Lee, H. S., Sun, H., and He, L. (2007b). "Performance Prediction of Single or Multi-Component Propulsors Using Coupled Viscous/Inviscid Methods." Proc. 10th Int. Symposium on the Practical Design of Ships and other Floating Structures, PRADS2007, Houston, TX, United States.

Kinnas, S. A., Chang, S.-H., Yu, Y.-H., and He, L. (2009). "A Numerical Method for Predicting the Performance of Podded and Ducted Propellers." Proc. Society of Naval Architects and Marine Engineers Propeller/Shafting '09 Symposium, Williamsburg, VA.

Kinnas, S. A., Chang, S.-H., and Yu, Y.-H. (2010). "Prediction of Wetted and Cavitating Performance of Water-jets." Proc. 28th Symposium on Naval Hydrodynamics, Pasadena, CA.

Kinnas, S. A., Chang, S.-H., Tian, Y., and Jeon, C.H. (2012a). "Steady and Unsteady Cavitating Performance Prediction of Ducted Propulsors." The 22nd International Offshore (Ocean) and Polar Engineering Conference and Exhibition, Rhodes (Rodos), Greece.

Kinnas S. A., Yu, X. and Tian, Y. (2012b). "Prediction of Propeller Performance under High Loading Conditions with Viscous/Inviscid Interaction and a New Wake Alignment Model." 29th Symposium on Naval Hydrodynamics Gothenburg, Sweden.

Lee, H. S. (2002). "Modeling of Unsteady Wake Alignment and Developed Tip Vortex Cavitation (UT-OE Report 02-4)." PhD Thesis, Ocean Engineering Group, Department of Civil, Architectural, and Environmental Engineering, The University of Texas at Austin, Austin, TX.

Lee, H. S. and Kinnas, S. A. (2004). "Application of BEM in the Prediction of Unsteady Blade Sheet and Developed Tip Vortex Cavitation on Marine Propellers." Journal of Ship Research, 48(1), 15–30.

Lee, H. S. and Kinnas, S. A. (2005). "A BEM for the Modeling of Unsteady Propeller Sheet Cavitation inside of a Cavitation Tunnel." Computational Mechanics, 37(1), 41-51.

Lee, H. S. and Kinnas, S. A. (2006). "Prediction of Cavitating Performance of Ducted Propeller." Proc. 6th Int. Symposium on Cavitation, CAV2006, Wageningen, The Netherlands.

Lindau, J. W., Moody, W. L., Kinzel, M. P., Dreyer, J. J., Kunz, R. F., and Paterson, E. G. (2009). "Computation of Cavitating Flow through Marine Propulsors." Proc. First Int. Symposium on Marine Propulsors, Trondheim, Norway, 211-221.

Lindau, J. W., Pena, C., Baker, W. J., Dreyer, J. J., Moody, W. L., Kunz, R. F., and Paterson, E. G. (2011). "Modeling of Cavitating Flow through Waterjet Propulsors." Proc. of 2nd International Symposium on Marine Propulsors, Hamburg, Germany, 142-151.

Mishra, B. (2005). "Prediction of Performance of Podded Propulsors via Coupling of a Vortex-Lattice Method with an Euler or a RANS Solver (UT-OE Report 05-1)." MS Thesis, Ocean Engineering Group, Department of Civil, Architectural, and Environmental Engineering, The University of Texas at Austin, Austin, TX.

Moon, I.-S., Kim, K.-S., and Lee, C.-S. (2002). "Blade Tip Gap Flow Model for Performance Analysis of Waterjet Propulsors." Proc. International Association for Boundary Element Methods (IABEM) '02 Symposium, Austin, TX, United States.

Morino, L. and Kuo, C.C. (1974). "Subsonic Potential Aerodynamics for Complex Configuration: a general theory." AIAA Journal, 12, 191-197.

Pan Y. and Kinnas, S. A. (2011). "A Viscous/Inviscid Interactive Approach for the Prediction of Performance of Hydrofoils and Propellers with Nonzero Trailing Edge Thickness." Journal of Ship Research, 55(1), 45–63.

Schroeder, S., Kim, S.-E., and Jasak, H. (2009). "Toward Predicting Performance of an Axial Flow Waterjet Including the Effects of Cavitation and Thrust Breakdown." Proc. of 1st International Symposium on Marine Propulsors, Trondheim, Norway, pp. 387-394.

Sun, H. and Kinnas, S. A. (2006). "Simulation of Sheet Cavitation on Propulsor Blades Using a viscous/inviscid interactive method." Proc. 6th Int. Symposium on Cavitation, CAV2006, Wageningen, The Netherlands.

Sun, H. (2008). "Performance Prediction of Cavitating Propulsors Using a Viscous/Inviscid Interaction Method (UT-OE Report 08-2)." PhD Thesis, Ocean Engineering Group, Department of Civil, Architectural, and Environmental Engineering, The University of Texas at Austin, Austin, TX.

Sun, H. and Kinnas, S. A. (2008). "Performance prediction of cavitating water-jet propulsors using a viscous/inviscid interactive method." Proc. 2008 SNAME Annual Meeting and Ship Production Symposium, Houston, TX.

Taylor, T. E., Kerwin, J. E., and Scherer, J. O. (1998). "Water-jet Pump Design and Analysis Using a Coupled Lifting-Surface and RANS Procedure." Proc. Int. Conf. on Water-jet Propulsion, The Royal Institution of Naval Architects, London, UK.

Warren, C., Taylor, T. E., and Kerwin, J. E. (2000). "A Coupled Viscous/Potential-Flow Method for the Prediction of Propulsor-Induced Maneuvering Forces. " Proc. Society of Naval Architects and Marine Engineers Propeller/Shafting '00 Symposium.

Wu, H., Soranna, F., Michael, T., Katz, J., and Jessup, S. (2008). "Cavitation Visualizes the Flow Structure in the Tip Region of a Waterjet Pump Rotor Blade." Proc. 27th Symposium on Naval Hydrodynamics, Seoul, Korea.

Wu, H. and Miorini, R. L. (2009). "ONR AxWJ-1 Waterjet performance Test." Report, Johns Hopkins University, Baltimore, Maryland.

Wu, H., Tan, D., Miorini, R. L. and Katz, J. (2011). " Three-dimensional Flow Structures and Associated Turbulence in the Tip Region of a Waterjet Pump Rotor Blade." Journal of Exp Fluids, 51, 1721-1737.

Young, Y. L. and Kinnas, S. A. (2001). "A BEM for the Prediction of Unsteady Mid-chord Face and/or Back Propeller Cavitation." Journal of Fluids Engineering, 123, 311–319.

Young, Y. L. (2002). "Numerical Modeling of Super-cavitating and Surface-piercing Propellers. (UT-OE Report 02-3)." PhD Thesis, Ocean Engineering Group, Department of Civil, Architectural, and Environmental Engineering, The University of Texas at Austin, Austin, TX.

Young, Y. L. and Kinnas, S. A. (2003). "Analysis of Super-cavitating and Surface-piercing Propeller Flows via BEM." Journal of Computational Mechanics, 32(4-6), 269–280.

Young, Y. L. and Kinnas, S. A. (2004). "Performance Prediction of Surface-piercing Propellers." Journal of Ship Research, 48, 288–304.

Yu, X. (2012). " Three Dimensional Viscous/Inviscid Interactive Method and Its Application to Propeller Blades (UT-OE Report 12-2)." Master Thesis, Ocean Engineering Group, Department of Civil, Architectural, and Environmental Engineering, The University of Texas at Austin, Austin, TX.

Vita

Shu-Hao Chang was born to Yong-Lang Chang and Sho-Qiong Wu on October 26th, 1979 in Taichung City, Taiwan, R.O.C. He graduated from Taipei Municipal Jianguo High School in 1997. He entered the Department of Civil Engineering at National Taiwan University where he achieved his Bachelor's degree in July, 2001 and completed his Master's degree in Hydraulic Engineering in July, 2003. In August 2006, he enrolled in the University of Texas at Austin for his doctoral study in the Ocean Engineering Group of the Department of Civil, Architectural, and Environmental Engineering.

Permanent address: 5F, NO. 3, Lane 10, Section 4, Cheng-de Road,
Shih-lin District 111-66, Taipei City, Taiwan,
Republic of China

This dissertation was typed with MS Word by the author.